FIB-SEM assisted exploration of honeycomb and kagome magnets

Franziska Breitner

Angaben zur Veröffentlichung / Publication details:

Breitner, Franziska. 2025. "FIB-SEM assisted exploration of honeycomb and kagome magnets." Augsburg: Universität Augsburg.

FIB-SEM assisted exploration of honeycomb and kagome magnets

Dissertation

zur Erlangung des akademischen Grades

Dr. rer. nat.

eingereicht an der
Mathematisch-Naturwissenschaftlich-Technischen
Fakultät
der Universität Augsburg

vorgelegt von

Franziska Arianna Breitner

Augsburg, Januar 2025

Universität
Augsburg
University

Erstprüfer: Prof. Dr. Philipp Gegenwart
Zweitprüfer: Prof. Dr. Manfred Albrecht

Tag der mündlichen Prüfung: 25.03.2025

Contents

List of Figures

List of Tables

1 Introduction

Both honeycomb Kitaev magnets and kagome magnetic metals have been in the focus of extensive research in the last couple of years.

The Kitaev model describes a spin-1/2 system in which no ordering occurs due to high frustration predicting a quantum spin liquid (QSL) as a ground state [1]. However, if additional interactions besides the Kitaev interaction, such as Γ or next- and third-nearest neighbour interactions, are present, no Kitaev quantum spin liquid behaviour is observed for the honeycomb Kitaev magnet. While some materials have been found to date which under certain conditions behave as a pure Kitaev material, the search for such a quantum spin liquid is still ongoing. For example, measurements of the thermal Hall conductance performed on α-RuCl$_3$ single crystals showed a half-integer quantized plateau [2] which would be a clear signature for a Kitaev QSL. Furthermore, the high frequency spectrum of the magnetic excitations of α-RuCl$_3$ above a critical field B_C probed by inelastic neutron scattering was reported to be a broad continuum [3] which is also seen as an indicator for proximity to a Kitaev QSL.

Kagome magnetic metals, on the other hand, show non trivial topological states, like flat bands or Dirac states [4–6], stemming from the two dimensional frustrated lattice, which are a playground for a plethora of fascinating phenomena. For example, antiferromagnetic ordering on a kagome lattice could give rise to classical or quantum spin liquids [7–9].

For both classes of materials, the magnetic and electronic properties were found to be very sensitive to the inclusion of foreign phases or doping [10–14] and the presence of either can lead to a significant change in the observed bulk properties. Therefore, upon investigating these materials, it is necessary to use an approach which avoids the occurrence of both unwanted doping and the presence of foreign phases.

Investigations of the microstructure as well as the space resolved chemical composition of the samples or the execution of experiments, such as pump-probe spectroscopy, for which micrometer thin samples are required would not be possible on bulk samples. Furthermore, bulk measurements are often restricted by the size and shape of grown crystals. Here, the focused ion beam (FIB) technology which allows for the precise control of shape as well as structuring on a micrometer scale presents a solution to many, if not all, of the challenges mentioned above.

The idea of using electron microscopy in order to image and analyse small structures goes back as far as the early 1930s, when the first electron microscope was invented by Ernst Ruska [15] and already mass produced less than 10 years later.

The next logical step then was to look at the interactions of heavy ions with matter which are even stronger than those of electrons and thus might be a useful device for the manipulation of matter on the nanoscale. For this purpose, at first solid sources were used, but proved to not be suitable for application on a larger scale. Thus, the search for an alternative lead to the invention of the first liquid metal ion source in 1975 [16] which was first used in scanning microscopy in 1979 [17]. Due to its low melting point, gallium was found to be a suitable candidate and is still widely used today. Other popular liquid metal ion sources include Al, In, Au or Sr [18]. In recent years, other sources such as liquid metal alloys [19], ionic liquid ion sources [20, 21] or plasma focused ion beams [22, 23], which offer several advantages compared to liquid metals such as comparatively higher resolution or higher sputtering rates, [24] were developed.

The basic working principle of a FIB can be described by the formation of a Taylor cone which is a self-forming cone-like tip on which the surface tension and electric field are balanced. Ions are generated at high voltages and can be directed towards the sample in a controlled way, allowing for the precise cutting of microscopic structures [25].

Today, this technique is widely used for the devising of very small structures on samples allowing for a wide range of measurements. In industry, FIB technology is mainly used for quality control and failure analysis in the semiconductor industry [26–28], whereas in research facilities it finds broad application in the preparation of ultrathin lamellae for transmission electron microscopy [29]. Further applications of the FIB technology include microstructuring of crystals for electrical or magnetic measurements, such as the fabrication of structures for Hall measurements on small crystals or thin films [30–32], simultaneous measurement along several crystallographic axes [33] and Josephson contacts [34, 35], or defect engineering [36, 37].

In the scope of this project, a combined FIB-SEM setup along with an EDX detector will be used to explore several members of the honeycomb Kitaev magnets, namely α-RuCl$_3$, Na$_2$IrO$_3$ and β-Li$_2$IrO$_3$, as well as the kagome magnetic metals CrRhAs and CrNiAs. Here, the FIB-SEM technology allows for a detailed investigation of these materials in a way not possible in measurements performed on bulk samples, including controlled contacting of micrometre scale structures, studying the influence of degradation on the space resolved structural and electrical properties as well as making Hall contacts for micrometre scale structures or samples too small to manually contact accordingly and the preparation of a large thin lamella for pump probe x-ray diffraction measurements.

This thesis begins with an introduction into the theoretical background, namely magnetism and electrical transport, in chapter 2, followed by a description of the experimental methods in chapter 3 including x-ray diffraction, energy dispersive x-ray spectroscopy and Laue back scattering as well as FIB-SEM microstructuring and the basics of magnetization and electrical transport measurement.

In chapter 4 the results of a combined study of the structural and electrical behaviour of Na_2IrO_3 uncovering the existence of sodium deficient structural domain walls and their metallic conductivity are presented.

Chapter 5 deals with the influence of thermal decomposition of α-$RuCl_3$ and the accompanying formation of RuO_2 on the samples low temperature properties, namely the heat capacity down to 0.4 K, magnetic susceptibility and electrical transport.

FIB structuring was employed to prepare a thin device of β-Li_2IrO_3 the process of which along with first XRD measurements confirming the samples suitability for further experiments, such as pump probe x-ray diffraction, is described in chapter 6.

The final chapters 7 and 8 deal with the kagome magnetic metals CrRhAs and CrNiAs. For both single crystals were grown and magnetic and electrical measurements performed. For CrNiAs, the influence of substituting Ni with Co or Cu and As with P on the ferromagnetic transition was investigated and compared to that of hydrostatic pressure.

Finally, in chapter 9 a summary is given along with an outlook on how to possibly proceed in the future.

2 Theoretical Background

For systems with weakly interacting electrons, theories such as the band model, which focus on the wave character of electrons, pose a good starting point for trying to understand their physical properties. The Fermi Liquid Theory for example, while still considering interactions by renormalizing the effective mass, is based on the assumption of so-called quasi-particles which are defined as particles in non-interacting systems. Both the total energy and band structure of such a system can be approximated with reasonably good accuracy by density function theory (DFT) ab initio calculations. For other systems, however, this approach is no longer suitable and theoretical expectations no longer match experimental findings. To name but one example, the known insulator NiO should be metallic according to band theory despite its large energy gap [38]. Materials for which the total state can no longer be described as the product of several single states and which thus show deviations from the behaviour expected for weakly interacting electrons are called correlated systems. The term describes a system in which the electrons can no longer be viewed as independent of each other and their interactions must be taken into consideration for the investigation of the underlying physics. Correlation often occurs in systems with partially filled d or f shells and is enhanced by narrow bands. For real systems with large numbers of electrons in the order of 10^{23}, suitable approximations are needed in order to describe the physics of such materials [39, 40].

The following chapter aims to give an overview over the relevant physics, starting with the introduction of magnetic materials in general and their underlying mechanism as well as the Kitaev model and its realization in real materials. The chapter ends with a general look at electrical transport properties and the theory of heat capacity.

2.1 Magnetism

Magnetism describes physical phenomena which result from the spatial orientation of magnetic moments, usually those of electrons. These ordering states arise from interactions between the particles [40]. In the following section, the origin of magnetic phenomena as well as different interaction mechanisms and types of magnetism will be described.

2.1.1 Local Moments

Hund's Rules

The ground state of an atom or ion can be described by the quantum numbers L (total orbital angular momentum), S (total spin angular momentum) and J (total angular momentum). They can only assume certain values and are limited by several constrictions, which are described by Hund's Rules which are:

1. The lowest energy state is achieved for maximum S, thus S needs to assume the largest possible value.
2. L must be maximum under the condition that Hund's First Rule is still observed.
3. L and S are coupled yielding J with
   $J = |L - S|$ for a less than half filled shell
   $J = |L + S|$ for more than half filling.

Obeying Rule One and Two leads to a minimization of the Coulomb repulsion, while Rule Three optimizes the spin orbit energy. However, exceptions to Hund's Rules can be found, if, for example, the degeneracy of the ground state is lifted and some orbitals are energetically favourable compared to others [41, 42].

Coulomb Interaction

Equally charged particles repel each other, while oppositely charged particles attract each other. This effect is called Coulomb interaction or Coulomb repulsion and is dependent on the charge of the participating particles.

Two electrons with same charge will always try to maximize their distance in order to minimize this repulsion. Thus, a strong Coulomb interaction restricts electron motion by localizing them. This on-site repulsion of electrons can be described using the Hubbard model. The Hubbard Hamiltonian

$$\mathcal{H} = -t \sum_{\langle ij \rangle \sigma} (c^{\dagger}_{i\sigma} c_{j_\sigma} + h.c.) + U \sum_{i} n_{i\uparrow} n_{i\downarrow} \tag{2.1}$$

contains the strength of the Coulomb repulsion, often referred to as Hubbard U, as well as the hopping integral of neighbouring lattice sites t which is determined by the wavefunction overlap of a spin pair. While U can be either positive or negative, t usually assumes a positive value. i and j are used to designate neighbouring lattice sites. $c^{\dagger}_{i\sigma} c_{j_\sigma}$ is the spin-density operator for a spin σ located on the i-th site and $n_i = n_{i\uparrow} + n_{i\downarrow}$ the density operator [43, 44].

Looking at the ratio of U and t some predictions regarding the electronic state of a material can be made. For $U < t$, the material is likely to show metallic behaviour, while for $U > t$ the electrons become more localized favouring insulating behaviour [45]. A metal-to-insulator transition can occur, if the Coulomb interaction surpasses the energy of the electron motion.

Crystal Field Splitting

In order to accurately describe the magnetic properties of a real system, the interactions of each magnetic ion with its neighbours needs to be considered.

The crystal electric field (CEF) model considers neighbouring orbitals as point charges with the symmetry of the local environment determining both magnitude and nature of this field. For transition metal compounds, an octahedral environment can often be found where a transition metal ion is located in the center of an octahedron with an ion (which often happens to be oxygen) at each corner. Due to the negative charge of the electrons in the corner ions, the crystal field in this case stems from electrostatic repulsion.

For an octahedral coordination or other equivalent symmetries, the d-orbitals can be divided into two types: the e_g- and the t_{2g}-orbitals. The latter are triple degenerate and point between the x-, y- and z-axes, while the former show a two-fold degeneracy and point along those axes. Since the e_g-orbitals in an octahedral environment overlap more with the neighbouring p-orbitals than the t_{2g}-orbitals, as can be seen in Fig. 2.1, a splitting of the energy levels occurs where the energy of the e_g orbitals increases compared to the free ion while that of the t_{2g}-orbitals decreases.

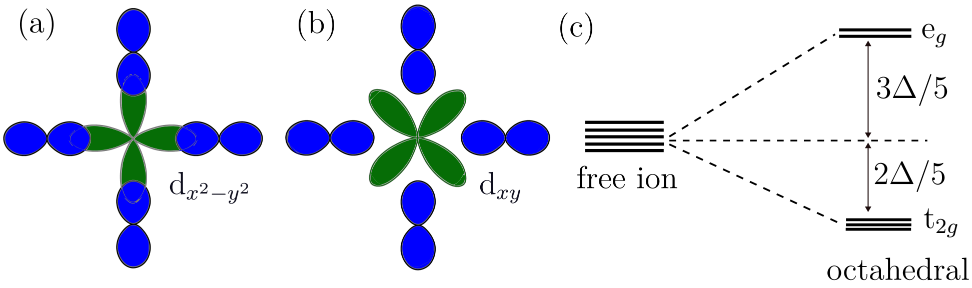

Figure 2.1: While the $d_{x^2-y^2}$ orbital directly overlaps with its neighbouring p-orbitals (a), the d_{xy}, d_{yz} and d_{zx} orbitals are further away (b). This leads to a splitting of the ground states into two energetically higher e_g and three energetically lower t_{2g} orbitals (c). Adapted from [42].

Depending on the size of the energy splitting Δ due to the CEF and intra-atomic Coulomb interaction, the orbitals will be occupied in a so called high-spin or low-spin configuration. For large Δ, an occupation scheme where the low energy states are doubly occupied before placing spins in the higher levels can be favoured resulting in a lower total spin. For small Δ an occupation scheme according to Hund's Rules is favoured and the total spin is maximized by filling each orbital with a spin before adding a second one to the lowest energy orbitals [42].

Spin Orbit Coupling

Spin-orbit coupling describes the interaction of a spin $\boldsymbol{S}$ and the orbital angular momentum $\boldsymbol{L}$ resulting in a total angular momentum $\boldsymbol{J} = \boldsymbol{S} + \boldsymbol{L}$. In a semi-classical picture, the nucleus with charge Ze revolves around a stationary electron creating a current I which in turn generates a magnetic field $\boldsymbol{B}_{\mathrm{orb}} = (\mu_0 I/2r)\boldsymbol{n}$ [46]. The magnetic energy of the spin moment $\mu_s = -g_s\mu_{\mathrm{B}}\boldsymbol{S}/\hbar$ and this field can then be written as

$$E_{\mathrm{so}} = -\boldsymbol{\mu}_s \cdot \boldsymbol{B}_{\mathrm{orb}} = \frac{Ze^2}{4\pi\epsilon_0 m_e^2 c^2 r^3}\boldsymbol{L}\cdot\boldsymbol{S}. \tag{2.2}$$

In a quantum mechanical picture, the effective magnetic field can be written as

$$\boldsymbol{B}^* = -\frac{\boldsymbol{v}\times\boldsymbol{E}}{2c^2} = \frac{1}{2m_e c^2}(\boldsymbol{p}\times\bigtriangledown\Phi_{\mathrm{el}}(r)) \tag{2.3}$$

Using the electron spin moment $\boldsymbol{\mu}_s = -g_s\mu_{\mathrm{B}}\boldsymbol{S}/\hbar$ as well as the central potential $\bigtriangledown\Phi_{\mathrm{el}} = (\boldsymbol{r}/r)\mathrm{d}\Phi_{\mathrm{el}}(r)/\mathrm{d}r$ and $\boldsymbol{r}\times\boldsymbol{p} = \boldsymbol{L}$ with Φ_{el} being the corresponding potential energy, the resulting Hamiltonian can then be written as

$$\mathcal{H}_{\mathrm{SO}} = \frac{e}{2m_e^2c^2}\frac{1}{r}\frac{\mathrm{d}\phi_{\mathrm{el}}(r)}{\mathrm{d}r}\boldsymbol{L}\cdot\boldsymbol{S} \tag{2.4}$$

For a hydrogen-like atom, one can further assume

$$\frac{1}{r}\frac{\mathrm{d}\phi(r)}{\mathrm{d}r} = \frac{Ze}{4\pi\epsilon_0 r^3} \tag{2.5}$$

and

$$\frac{1}{r^3} = \frac{Z^3}{a_0^3 n^3 l(l+\frac{1}{2})(l+1)} \tag{2.6}$$

with the quantum numbers l and n and the Bohr radius a_0 resulting in the Hamiltonian being rewritten as

$$\mathcal{H}_{\mathrm{SO}} = \gamma\boldsymbol{S}\cdot\boldsymbol{L} \propto \frac{Z^4}{n^3 l(l+\frac{1}{2})(l+1)}\boldsymbol{L}\cdot\boldsymbol{S} \tag{2.7}$$

The spin orbit coupling thus depends on the quantum numbers l and n, as well as the atomic number Z and the scalar product of $\boldsymbol{L}$ and $\boldsymbol{S}$. The coupling of the strength is described by the spin-orbit coupling constant λ.

Eq.(2.7) has to be multiplied with a correction factor of $\frac{1}{2}$ due to the relativistic character of spin-orbit coupling [47]. Furthermore, this model is but a rough approximation, since for systems with more electrons than hydrogen, the electric field of the electron is influenced by those additional charges, though compared to the nuclear contribution this effect is rather small [42].

Spin-orbit coupling causes magnetic anisotropy due to the shifted energy states which indicates the existence of a preferred orientation of the magnetization.

2.1.2 Competing Interactions and Frustration

Magnetic Ordering

The magnetic properties of a solid are mostly defined by its spins and the orbital motion of the electrons. While there is a non-zero nuclear contribution, for most materials it is small compared to that of the electrons. The magnetization $M = \frac{m}{V}$ is defined as the magnetic moment m per volume V. The ratio of magnetization to applied magnetic field is a material specific parameter which is called the magnetic susceptibility

$$[\chi] = \frac{M}{H} \tag{2.8}$$

A sample is paramagnetic for a positive and diamagnetic for a negative susceptibility. Ferromagnets which show a spontaneous magnetization and antiferromagnets are special cases and will be dealt with later on in this section.

The temperature dependence of the magnetic susceptibility for the different forms of magnetic order is shown in Fig. 2.2. While the temperature dependent susceptibility of a paramagnet smoothly increases with decreasing temperature, that of a ferro- or antiferromagnet shows a kink at an ordering temperature. For antiferromagnets, the susceptibility below the ordering temperature begins to decrease again.

Paramagnetism Paramagnetism can occur in samples with odd electron number or partially filled shells resulting in a local magnetic moment. In the absence of a magnetic field, the net moment is equal to zero due to the random distribution of magnetic moments, as shown in Fig. 2.3(a), while applying a magnetic field to a paramagnet leads to an orientation of the spins along the field direction. The temperature dependent magnetic susceptibility of a paramagnet is described by Curie's Law

$$\chi_m = \frac{C}{T} \tag{2.9}$$

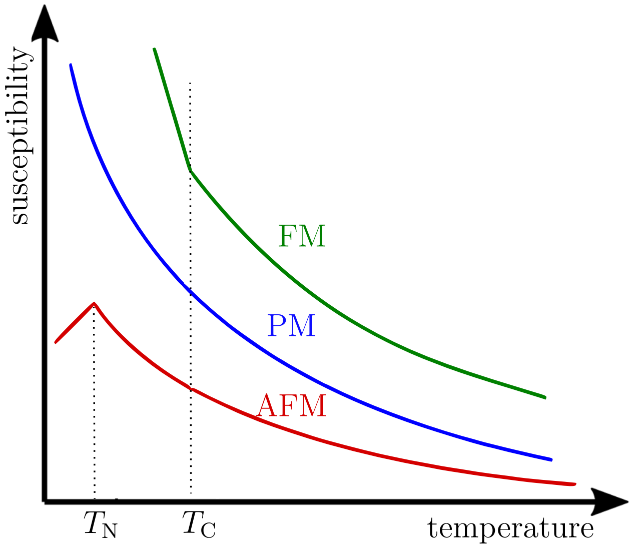

Figure 2.2: Temperature dependence of the magnetic susceptibility of a paramagnet, ferromagnet and antiferromagnet with the respective ordering temperatures marked by a kink in the plot.

with the material specific Curie constant $C = \mu_0 n \frac{p^2 \mu_\mathrm{B}^2}{3k_\mathrm{B}}$ where μ_0 is the vacuum permeability, $n = \frac{N}{V}$ the particle density, k_B the Boltzman constant, $p = g\sqrt{J(J+1)}$ the effective magnetic moment and μ_B the Bohr magneton. Since the individual moments are not coupled, paramagnets do not show any magnetic ordering down to lowest temperature. [46]

Diamagnetism In the absence of a magnetic field a diamagnet shows no permanent magnetic moment. Looking at the orbital motion of the electrons as a circular current, one finds that upon applying an external magnetic field, a current is induced. According to Lenz's rule the resulting magnetic field then counteracts the initial external field. The diamagnetic susceptibility shows a negative sign and is largely temperature independent. Though diagmagnetism occurs in all materials, it is a rather weak effect which is often hidden by larger contributions of other kinds of magnetism [46]. For a material in the superconducting state, the susceptibility shows a value of $\chi = -1$ meaning it behaves like an ideal diamagnet [48].

Ferromagnetism Unlike paramagnets, the magnetic moments of ferromagnets locally interact with each other resulting in the formation of areas with parallel spins called Weiss domains. Since these domains are not aligned with each other, the net magnetization can be zero.

Below a material specific temperature T_C, the so called Curie temperature, ferromagnetic materials show spontaneous magnetization even in the absence

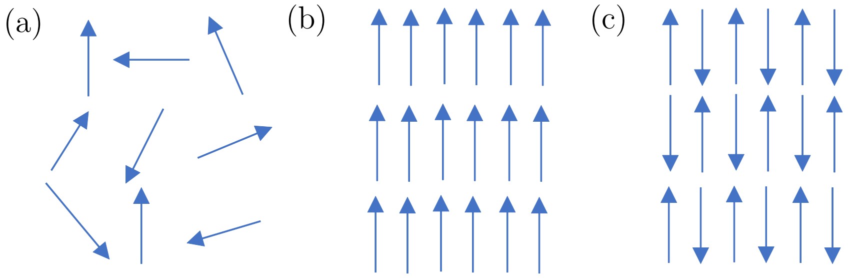

Figure 2.3: Schematic depiction of the basic forms of magnetic order. (a) Paramagnetism: Random orientation of non-interacting magnetic moments. (b) Ferromagnetism: Magnetic moments are aligned parallel. (c) Antiferromagnetism: Two sublattices with antiparallel orientation of the magnets and a net magnetic moment of zero.

of an applied magnetic field. This is due to quantum mechanical exchange interactions between permanent magnetic moments leading to a spatial ordering of the moments. The magnetic susceptibility of a ferromagnet above the ordering temperature can then be written as

$$\chi = \frac{C}{T - T_{\mathrm{C}}} \tag{2.10}$$

Applying a magnetic field to a ferromagnet results in a shrinking of those Weiss domains not aligned parallel to the external field. Once all moments are aligned, as depicted in Fig. 2.3(b), the resulting magnetization is referred to as saturation magnetization. Looking at the field dependent magnetization of a ferromagnet, one can observe a hysteresis. Setting the external field back to zero can result in a non zero magnetization of the ferromagnet, the remanent field. A magnet is called "hard" magnet if this remanent field is of sufficient magnitude. [41, 42]

Antiferromagnetism Like ferromagnets, antiferromagnets, too, show spontaneous magnetization in the absence of an external field. Unlike for ferromagnets, however, the neighbouring spins align antiparallel towards each other, as can be seen in Fig. 2.3(c), resulting in a net zero magnetic moment. This phenomenon often occurs in systems for which the crystal lattice can be treated as a combination of two sublattices with different spin orientations [42]. For antiferromagnets, the ordering temperature below which the materials behaviour changes from paramagnetic to antiferromagnetic is called Néel temperature T_{N} [41].

Frustrated Magnetism

The competition of different magnetic interactions within a material can lead to frustration, if the competing demands cannot be satisfied simultaneously and the minimum energy state can be achieved by multiple spin configurations leading to a degenerate ground state. In frustrated systems, magnetic order is suppressed [49,50]. The degree of frustration of a system can be quantified using the frustration parameter $f \equiv |\theta_{\mathrm{CW}}|/T_{\mathrm{N}}$ which is defined as the ratio of the systems Curie-Weiss and Néel temperature [51]. A system is strongly frustrated (and thus has a large frustration parameter) if the spin exchange interaction allows for a large amount of fluctuations between the different minimum energy states [52]. In general, one can differentiate between geometrical and exchange frustration, both of which will be explained in more detail in the following paragraphs.

Geometrical Frustration The typical example of geometrical frustration is a triangular lattice with a spin on each corner which points either up or down and antiferromagnetic interactions. In this case, it is not possible for each spin to be arranged antiparallel to its neighbours and thereby minimize their interaction energy. Thus, six energetically equivalent arrangements are found with either two up and one down spin or vice versa, which are depicted in Fig. 2.4.

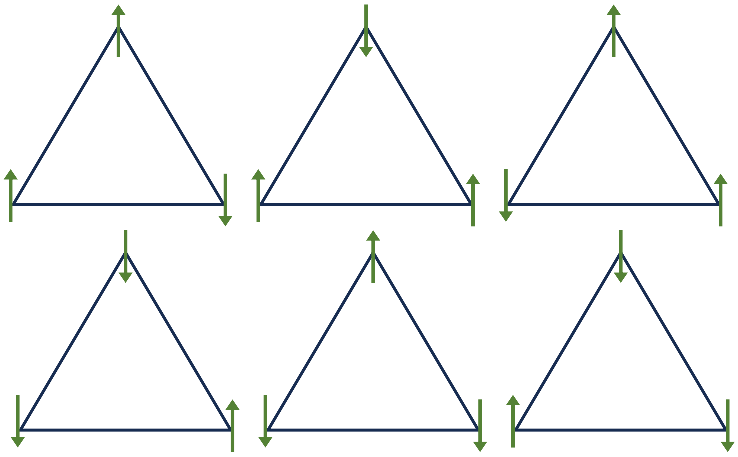

Figure 2.4: Geometrical frustration on a triangular lattice. Since it is not possible to arrange the three spins in such a way that they are antiparallel to each neighbour, one can find six different minimum energy states. Adapted from [50].

In real systems, the triangles can share either corners or edges. In 2D, corner sharing triangles form a so called kagome lattice, a 3D corner sharing lattice is usually referred to as pyrochlore lattice [51], both of which can be seen in Fig. 2.5.

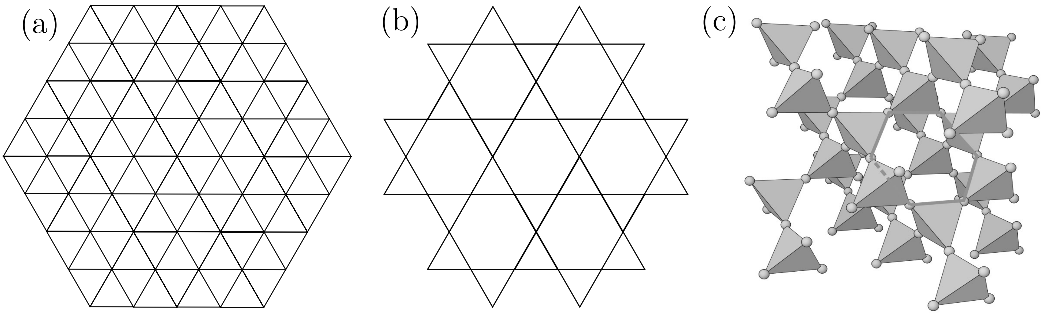

Figure 2.5: 2D and 3D realizations of a triangular lattice on which geometrical frustration can occur: (a) triangular lattice (b) Kagome lattice (c) pyrochlore lattice. Adapted from [51, 53].

Exchange Frustration Another type of frustration is the so-called exchange frustration which occurs when not all exchange interactions can be minimized at the same time. An example for this would be a quantum spin with ferromagnetic coupling to all its neighbouring spins which all show different orthogonal quantisation axes. The minimum energy would be achieved if the spin would be oriented parallel to all quantisation axes which is, however, not possible [54]. One of the most commonly known models dealing with exchange frustration is the Kitaev model, which will be dealt with further in the next parts of this thesis [55].

Spin Liquids Frustrated systems in which the spins are strongly correlated while at the same time showing strong fluctuations down to lowest temperature are called spin liquids. The spin fluctuations can be of classical or quantum nature. For large spins the thermal energy is the driving force enabling fluctuations, and classical fluctuations are dominant. With decreasing temperature, the thermal energy $k_{\mathrm{B}}T$ becomes smaller until classical fluctuations are no longer possible and the spins order or freeze.

In the quantum mechanical picture, a spins magnitude is quantized in half-integer units of $\hbar$. For small spins close to 1/2, motion is still possible even at zero temperature due to zero-point motion permitted by the quantum mechanical uncertainty principle. Unlike for classical fluctuations, phase coherence can occur for quantum fluctuations. For sufficient strength of these fluctuations, the spins are simultaneously oriented along several directions forming a superposition state preventing any conventional long range magnetic order. Such a material is called a quantum spin liquid, short QSL [7, 8]. The highly entangled nature of this ground state gives QSLs unique and intriguing physical properties, such as fractional excitations or topological states [56].

Kitaev Materials

Since several members of the honeycomb Kitaev magnets are investigated in this thesis, this section will give a brief introduction into the Kitaev materials.

Kitaev Model The Kitaev model is an analytically solvable model for a hexagonal 2D honeycomb lattice with a quantum spin liquid ground state. It was developed by Alexei Kitaev in 2006 [1]. Kitaevs model deals with Ising-type exchange interactions of spin-1/2 moments located on a honeycomb lattice wherein the anisotropic spin-spin exchange interactions depend on the orientation of the bonds and the exchange interaction is orthogonal to the bond direction. These different exchange interactions are referred to as x, y and z referring to the spin component which can be described by

$$\mathcal{H} = -J_x \sum_{\langle ij \rangle} \sigma_i^x \sigma_j^x - J_y \sum_{\langle ij \rangle} \sigma_i^y \sigma_j^y - J_z \sum_{\langle ij \rangle} \sigma_i^z \sigma_j^z \tag{2.11}$$

with $J_{x,y,z}$ the coupling constants and $\sigma^{x,y,z}$ the Pauli operators. Fig. 2.6 shows the different interactions on the honeycomb lattice. Here, the bond labels refer to the spin component taking part in the interaction.

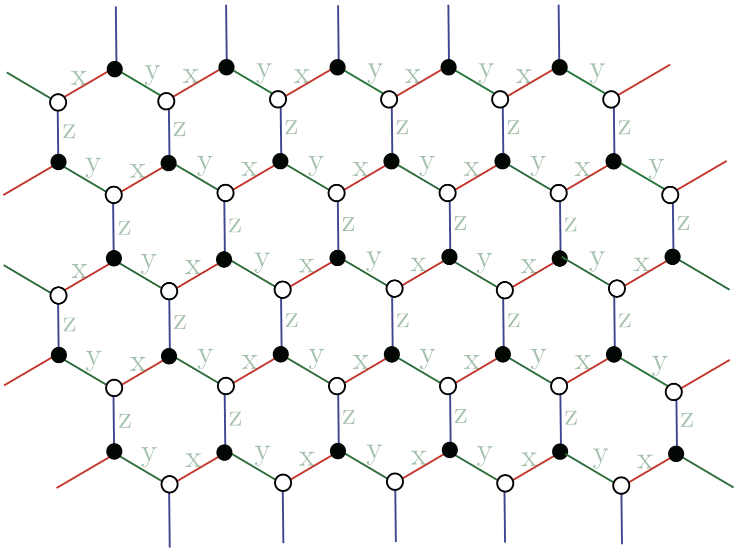

Figure 2.6: Orthogonal Ising interactions on the honeycomb lattice in the Kitaev model. Each spin interacts with three different neighbours and the interactions are labelled x, y and z corresponding to the partaking spin component. Adapted from [1].

An exact solution for the Kitaev model can be found by introducing four Majorana fermions $\{b_i^x, b_i^y, b_i^z, c_i\}$ with $S_i^\gamma = \frac{i}{2} b_i^\gamma c_i$ and $\gamma = \{x, y, z\}$ in order to represent the spin operators resulting in the following Hamiltonian [57]:

$$\mathcal{H} = \frac{1}{4} \sum_{\langle ij \rangle} b_i^\gamma b_j^\gamma c_i c_j \tag{2.12}$$

From this form, a quadratic Hamiltonian can be derived which can be exactly diagonalized. Fig. 2.7 shows the solution for the ground state represented as a phase diagram depending on the coupling constants. Here, the ground state is a quantum spin liquid with short range nearest-neighbour spin correlations which is either gapped (A) or gapless (B) [1]. Kitaev further observed, that anionic excitations can be found in the gapped phase which forms upon exposure to a finite magnetic field which could find possible applications in the field of topological quantum computing [58].

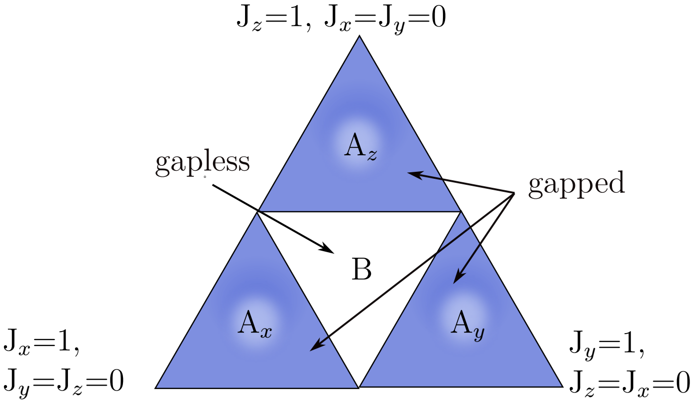

Figure 2.7: An exact solution for the Kitaev model can be found using Majorana fermions. The ground state is a gapped or gapless quantum spin liquid. Adapted from [1].

Jackeli-Khaliullin Mechanism In 2009, Jackeli and Khaliullin published their first paper looking for a realization of the Kitaev model in real systems. To this end, they considered transition metal oxides with strong spin-orbit coupling and oxygen atoms in an octahedral configuration [59]. A prime candidate for this was the class of $A_2\text{IrO}_3$ (A =Li, Na) compounds with a 5d^5 configuration of the Ir^{4+} ions on a honeycomb lattice [60].

For a free ion, the d-orbitals are degenerate, whereas in real systems degeneracy can be lifted by crystal field splitting and spin-orbit coupling (as discussed previously). For sufficiently large U, a system can become a Mott insulator [45].

In the absence of both crystal field and spin-orbit coupling, the Iridium 5d levels show a tenfold degeneracy. Taking the CEF splitting into consideration, the five electrons in the 5d level first occupy the energetically lower t_{2g} orbitals resulting in metallic behaviour due to the partially filled band. The degeneracy of the t_{2g} orbitals is further lifted, when SO coupling is taken into consideration, splitting them into a doubly degenerate band with effective total angular momentum $J = L - S = 1/2$ and a fourfold degenerate level with $J = L + S = 3/2$. Here, the energetically lower $J_{\text{eff}} = 3/2$ band is filled first, resulting in only a single electron in the then half-filled $J_{\text{eff}} = 1/2$ band [57, 61], which can be seen in Fig. 2.8. If U is of sufficient magnitude, the $J_{\text{eff}} = 1/2$ bands are split again into a lower Hubbard band (LHB) and an upper Hubbard band (UHB) and the system becomes a Mott insulator with strongly localized spin-1/2 moments showing high anisotropy [62].

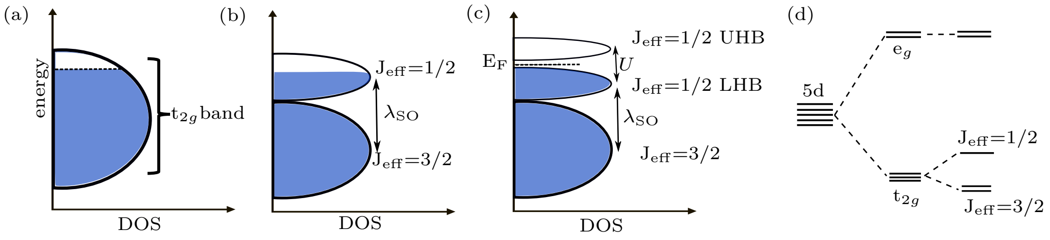

Figure 2.8: In the absence of both spin-orbit coupling and Coulomb repulsion, the schematic energy diagram is that of a wide t_{2g} band metal (a). Spin-orbit coupling leads to a splitting of the band into a lower $J_{\text{eff}} = 3/2$ and a half filled energetically higher $J_{\text{eff}} = 1/2$ band (b). Considering both SOC and U, a Mott ground state is formed with a filled $J_{\text{eff}} = 1/2$ LHB and an empty $J_{\text{eff}} = 1/2$ UHB separated by a gap (c). (d) shows the level splitting due to the influence of SOC and U. Adapted from [61].

Here, the exchange Hamiltonian of the spins depends on the bond geometry. Exchange ideally occurs through transition metal–ligand-transition metal (e.g. Ir-O-Ir) bonds with a 90° bond angle. There are two exchange path in the xy-plane which interfere destructively, meaning the isotropic term in the exchange Hamiltonian is equal to zero and effectively vanishes. Thus, for idealized edge-sharing octahedra only anisotropic interactions from orthogonal bonds contribute. This is exactly the sought-after Kitaev contribution [57].

Realization in Real Materials Finding a pure Kitaev system in real materials has proven difficult due to two main factors:

1. Local distortions due to CEF, mixing with higher energy states as well as direct coupling of d-orbitals must be considered in order to accurately describe the coupled bonds.
2. Exchange interactions between more than nearest neighbours may need

to be considered, since both 4d and 5d orbitals cover rather large spatial areas.

In general, the following Hamiltonian can be used to describe anisotropic magnetic interactions between two sites i and j

$$\mathcal{H}_{ij} = \boldsymbol{S}_i \cdot \boldsymbol{J}_{ij} \cdot \boldsymbol{S}_j \tag{2.13}$$

Here, $\boldsymbol{J}_{ij}$ is a 3×3 exchange tensor the parameters of which depend on the local symmetry. For C_{2h} symmetry, the interactions between the ij-bonds is written as

$$\begin{aligned} \mathcal{H}_{ij} = \boldsymbol{S}_i \cdot \boldsymbol{J}_{ij} \cdot \boldsymbol{S}_j + \boldsymbol{K}_{ij} S_i^\gamma S_j^\gamma + \Gamma_{ij}(S_i^\alpha S_j^\beta + S_i^\beta S_j^\alpha) + \\ \Gamma'_{ij}(S_i^\gamma S_j^\alpha + S_i^\gamma S_j^\beta + S_i^\alpha S_j^\gamma + S_i^\beta S_j^\gamma) \end{aligned} \tag{2.14}$$

with $\{\alpha, \beta, \gamma\} = \{x, y, z\}, \{y, z, x\}, \{z, x, y\}$ for the Z-, X- and Y-bonds. Additional terms may need to be added for systems with lower symmetry [57].

In 2010, Chaloupka et al. introduced the Heisenberg-Kitaev model, where they added a Heisenberg exchange parameter J_1 to the Kitaev model [60, 63].

Later works looked at the off-diagonal nearest-neighbour interactions Γ_1 and Γ'_1 [64–66] as well as Heisenberg J_2 and J_3 interactions [67, 68] and exchange with the next nearest neighbour described by the Kitaev K_2 term [69].

These studies found indications for several states with interesting magnetic ordering due to competing anisotropic interactions. For large nearest neighbour interactions Kitaev spin-liquid states can be found.

2.1.3 Magnetism in Metals

While the prior sections dealt with magnetism due to local moments, magnetism can also be caused by free charge carriers. This so called itinerant magnetism stems from delocalized electrons in the bands and can be found in metals.

Itinerant magnetism

The Stoner model describes the origin of itinerant magnetism as the shift of the densities of states for electrons with up compared to those with down spin due to exchange interactions. The model is based on the assumption, that unsaturated spins in the d band carry the magnetism. Furthermore, a molecular field term is used to describe the exchange effects and Fermi statistic must be adhered to. Starting from the paramagnetic DOS and splitting the spins into an up and a down band, the supplication of an external magnetic field results in a shift of the two bands in relation to each other. This shift leads to an increase of the kinetic energy of $\Delta E_{\mathrm{kin}} = \frac{g(E_{\mathrm{F}})\delta E}{2} \cdot \delta E$.

As a consequence, the electrons must be redistributed, as the Fermi level is the same for both bands which leads to a difference in the occupation numbers. The systems magnetization can then be written as $M = \mu_{\mathrm{B}}(N^{-} - N^{+}) = \mu_{\mathrm{B}} g(E_{\mathrm{F}})\delta E$ with N^{-} and N^{+} the concentration of spin-up and spin-down electrons. Integrating the magnetization yields the change in potential energy

$$\Delta E_{\mathrm{pot}} = -\int_{0}^{M} M' \mu_0 \lambda \mathrm{d}M' = -\frac{1}{2}\mu_0 \mu_{\mathrm{B}}^2 \lambda (g(E_{\mathrm{F}})\delta E)^2 = -\frac{1}{2} U (g(E_{\mathrm{F}})\delta E)^2 \tag{2.15}$$

where λ and thus U is a measure for the strength of the molecular field.

The total energy difference is then the sum of the difference in potential and kinetic energy respectively

$$\Delta E_{\mathrm{tot}} = \frac{1}{2} g(E_{\mathrm{F}})(\delta E)^2 (1 - U g(E_{\mathrm{F}})) \tag{2.16}$$

Spontaneous spin polarization and thus magnetism is likely to occur, if the Stoner criterion

$$U g(E_{\mathrm{F}}) \geq 1 \tag{2.17}$$

and thus $\Delta E_{\mathrm{tot}} < 0$, is fulfilled [70–72].

A classical example for itinerant antiferromagnetism is the 3*d* transition metal chromium and its alloys, as was first suggested by Néel in 1936 [73]. The systems 3*d* character is likely to be a significant influence on the observed magnetic properties [74]. Chromium shows an incommensurate spin density wave below the Néel temperature of $T_{\mathrm{N}} = 311\,\mathrm{K}$ with a characteristic wave vector $\boldsymbol{Q}$ stemming from nesting of the Fermi surface along the <100> direction.

A second transition can be found at $T_{\mathrm{SF}} = 121\,\mathrm{K}$ where a spin flip occurs and the spin density wave changes its polarization from transversal to longitudinal.

2.2 Electrical Transport Measurements

The following section aims to give a brief summary of the different transport phenomena relevant for this work.

Looking at the location of the Fermi level in relation to the different bands within the band structure, as can be seen in Fig. 2.9, the following general categorization can be found: For metals, the Fermi level is located within a band, whereas for insulators and semiconductors, the Fermi level lies within the band gap between valence and conduction band. The latter two differ by the size of the band gap. For semiconductors, the band gap is small enough that at room temperature it is possible for charge carriers from the valence band to reach the conduction band by thermal excitation resulting in some conductivity, whereas for insulators the band gap is significantly larger making the occurrence of this process unlikely [41]. The following section will mainly focus on the temperature dependent electrical transport as well as the Hall effect and variable range hopping.

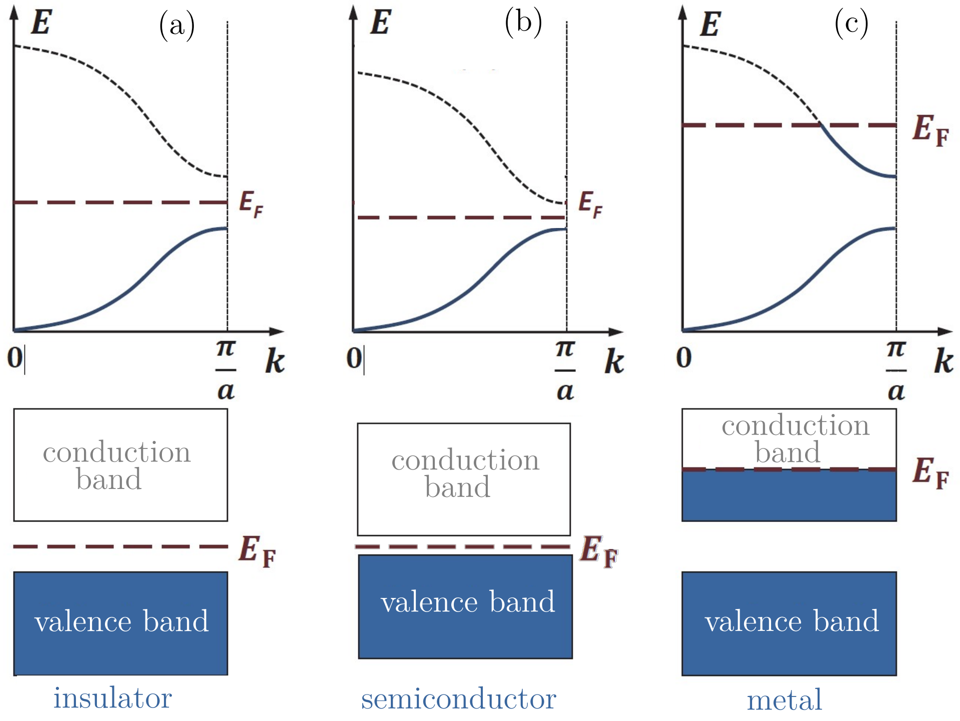

Figure 2.9: Band structure and location of the Fermi level for insulators, semiconductors and metals. Adapted from [41].

2.2.1 Insulators and Metals

For materials classified as metals, the conduction band is partially filled. Furthermore, the valence electrons of metals are delocalized. Electrical conductivity stems from valence electrons energetically close to the Fermi energy.

Metallic conductivity can be described using the so called Drude equation

$$\sigma = \frac{ne^2}{m^*} \tag{2.18}$$

with n being the charge carrier density close to the Fermi level, m^* the effective electron mass and τ the scattering time. Here, only τ shows a significant dependence on the temperature making defect and phonon scattering the main mechanism determining metallic conductivity. The total resistivity of a metal can then be written as

$$\rho(T) = \rho_{\text{res}} + \rho_{\text{ph}}(T) = \frac{ne^2}{m^*}\tau_{\text{d}} + \frac{ne^2}{m^*}\tau_{\text{ph}}(T) \tag{2.19}$$

by simply adding up the different contributions. This is also called Matthiesen rule. Here, ρ_{res} describes a temperature independent contribution caused by defect scattering which is proportional to the defect concentration. $\rho_{\text{Ph}}(T)$ is the sum of contributions due to phonon-electron interactions above and below the Debye temperature. For temperatures $T \ll \theta_{\text{D}}$ electron phonon interaction results in a $\rho_{\text{ph}} \propto T^5$ behaviour, also known as Bloch's law. For temperatures $T \gg \theta_{\text{D}}$, where all phonon states are thermally excited linear behaviour is expected, as can be seen in Fig. 2.10 [75].

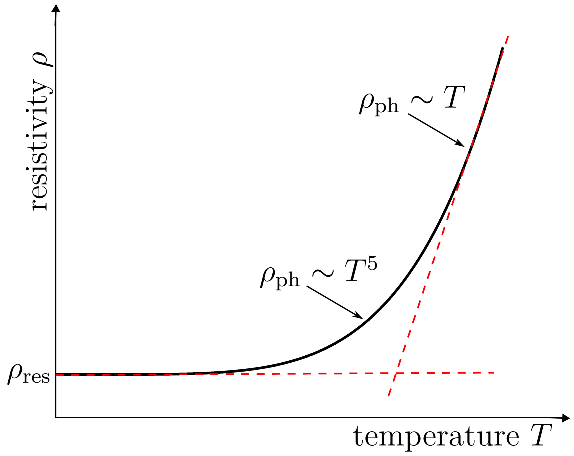

Figure 2.10: Temperature dependence of the electrical resistivity of a metal. Above the Debye temperature θ_{D}, the resistivity follows a linear behaviour due to Umklapp-electron-phonon scattering being the dominant transport mechanism. Below θ_{D}, normal electron-phonon scattering results in $\rho \propto T^5$ behaviour, while at lowest temperatures, where phonons freeze out, a constant residual resistivity ρ_{res} can be detected due to defect scattering.

Insulating behaviour occurs in materials, where the chemical potential is located in the gap of a fully filled valence band and an empty conduction band. Systems with an even electron number per unit cell and no band overlap are called band insulators [41]. Other types of insulators are Anderson insulators, topological insulators or Mott insulator. Insulators show a very high resistivity which increases with decreasing temperature. For sufficiently high temperatures, insulators can develop electrical transport. However, for many materials, this transition temperature is higher than the materials melting point. Vice versa, the conductivity of materials which show semiconducting behaviour at room temperature can transition to insulating behaviour at sufficiently low temperatures if the thermal energy is no longer sufficient to excite electrons into the CB [76].

2.2.2 Semiconductors

In semiconductors, the conduction (CB) and valence band (VB) are separated by an energy gap $E_\mathrm{g} > 0\,\mathrm{eV}$ which is smaller than that of insulators, allowing electrons to move from VB to CB by thermal excitation. While this can also happen in insulators, the probability for such a transition, and thus the conductivity, is increased for the smaller band gaps found in semiconductors compared to insulators. Similarly, for Mott insulators the relevant bands, called lower (LHB) and upper Hubbard band (UHB), are separated by an energy gap. However, while the conduction and valence band stem from different orbitals, the lower and upper Hubbard band are formed due to the splitting of one band. Nevertheless, both semiconductors and Mott insulators with comparably large band gaps such as Na_2IrO_3 show similar conduction mechanisms and a thermal excitation ansatz can be used.

Unlike for metals, where only τ shows a strong temperature dependence and the conductivity simply decreases with increasing temperature, in the case of semiconductors both charge carrier density and relaxation time are strongly temperature-dependent. At absolute zero, semiconductors are insulating, whereas at finite temperature electrons can be excited from the VB to the CB. The temperature dependence of the conductivity follows the exponential relation

$$\sigma \approx \sigma_0 \exp\left(\frac{-E_g}{k_\mathrm{B}T}\right) \tag{2.20}$$

where σ_0 contains the effective masses of holes and electrons showing a weak, but small compared to the exponential, temperature dependence.

While in intrinsic semiconductors free electrons and holes are found due to excitation from the VB to the CB, the conductivity can also be influenced extrinsically by doping. Here, impurities or atoms with a different number of conduction electrons are introduced or the sample stoichiometry is varied resulting in excess electrons in the conduction band (donors) or holes in the VB (acceptors) leading to an increased charge carrier density [41, 46].

Variable Range Hopping

The concept of variable range hopping (VRH) was introduced by Sir Nevill Mott in 1968. It describes the hopping of electrons between sides that are spatially distant but close in energy. The concept is depicted in Fig. 2.11.

Looking at the hopping probability between non-correlated localized states, the net electron flow between states i and j can be described by

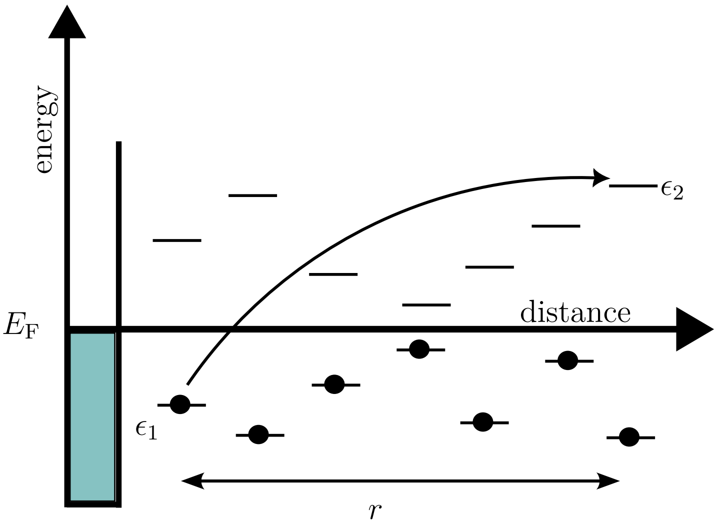

Figure 2.11: Spatial and energetic distribution of localized states around the Fermi energy. The states below E_F are filled, while those with higher energies are empty. The arrow signifies a jump from ϵ_1 to ϵ_2 by variable range hopping. Figure adapted from [77].

$$I_{ij} = f_i(1 - f_j)w_{ij} - f_j(1 - f_i)w_{ji} \tag{2.21}$$

where $f_i = [\exp(\frac{E_i - \mu_i}{k_\mathrm{B}T}) + 1]^{-1}$ is the probability, that state i is occupied. $w_{ij} = \gamma \cdot P_{ij}$ is the rate of electron transitions from state i (occupied) to state j (empty) which can be described by the product of the frequency of transition attempts γ and the probability P_{ij} of such a transition being successful. As VRH arises from tunnelling, the hopping probability is a derivative of the tunnelling probability $P_{\mathrm{t},ij} = \exp(-2\alpha|r_{ij}|)$ where r is the spatial distance between the states and α describes the states localization. Thus, the transition rate can be described as

$$w_{ij} = \gamma e^{-2\alpha|r_{ij}|}(e^{-\frac{E_i - E_j}{k_\mathrm{B}T} - 1})^{-1} \tag{2.22}$$

Inserting (2.22) in (2.21) while assuming $\Delta E \geqslant k_\mathrm{B}T$, $\mu \approx \mu_i \approx \mu_j$ and a small electric field yields

$$\sigma_{ij} = \frac{I_{ij}}{\Delta\mu} \sim \gamma \exp(2\alpha|r_{ij}| + \frac{|E_i - \mu| + |E_j - \mu| + |E_i - E_j|}{2k_\mathrm{B}T}) \tag{2.23}$$

This is the so called Miller-Abrahams conductance [78–80].

Mott further simplified the hopping process by assuming that only states within $\pm k_\mathrm{B}T$ of μ contribute significantly to the hopping current. This results in a hopping probability of

$$P_{ij} = \begin{cases} e^{-2\alpha r_{ij} - \frac{E_j - E_i}{k_\mathrm{B}T}}, & \text{if } E_j > E_i \\ e^{-2\alpha r_{ij}}, & \text{if } E_j \leq E_i \end{cases} \tag{2.24}$$

For systems with a random distribution of localized states, nearest neighbour hopping occurs in 4D space described by three spatial and one energy coordinates [81, 82]. Hopping is directed towards the site at closest range, which is the spatially closest site, if the first term in (2.24) is dominant (so called nearest neighbour hopping) and the energetically closest site, if the second term in the exponential function in (2.24) is dominant. In the second case, at sufficiently low temperatures, variable range hopping occurs.

The inter-site resistivity resulting from hopping can then be described as

$$R_{ij} = R_{ij}^0 \cdot e^{(\frac{2r_{ij}}{a} + \frac{E_i - E_j}{k_\mathrm{B}T})} \tag{2.25}$$

with a being the localization length [83,84]. Here, the first exponential term being dominant once again describes nearest neighbour hopping, while the second term dominating corresponds to variable range hopping occurring.

From this a macroscopic VRH resistivity can be derived as follows. At low temperatures, only states within an interval $[E_\mathrm{F} - \epsilon, E_\mathrm{F} + \epsilon]$ around the Fermi energy contribute to hopping. Thus, the density of state can be described as $D(E) \approx D(E_\mathrm{F})$. Within a certain volume $V \propto r^d$ (with d being the dimension), the number of states n is constant. The spatial distance can be written as $r \propto (2 \cdot D(E_\mathrm{F}) \cdot \epsilon)^{-\frac{1}{d}}$. Using the average activation energy $\langle \Delta E \rangle = \epsilon$ [85, 86], the average macroscopic resistance can then be obtained from r_{ij} as

$$R \propto \exp\left(\frac{1}{a \cdot (2 \cdot D(E_\mathrm{F}) \cdot \epsilon)^{\frac{1}{d}}} + \frac{\epsilon}{k_\mathrm{B}T}\right) \tag{2.26}$$

Here, the resistance reaches a minimum when both exponential terms are equal. This is the case for $\epsilon = (\frac{k_\mathrm{B}T}{a \cdot (2D(E_\mathrm{F}))^{\frac{1}{d}}})^{\frac{d}{d+1}} \propto T^{\frac{d}{d+1}}$. Using this information, (2.26) can be written as

$$R = R_0 \cdot \exp\left(\frac{T}{T_0}\right)^{\frac{1}{d+1}} \tag{2.27}$$

with $T_0 = 21.2 \cdot (k_\mathrm{B} D(E_\mathrm{F}) a^d)^{-1}$ for 3D variable range hopping [87].

Plotting the logarithmic resistance or resistivity $\ln(\rho)$ over $T^{-\frac{1}{4}}$ therefore results in a linear plot for the temperature range in which variable range hopping occurs and the hopping temperature T_0 can be extracted by linearly fitting the data.

2.2.3 Hall Effect

In order to understand the Hall effect, it is useful to look at the movement of electrons in a conductor. Applying an external electrical field $\boldsymbol{E}$ to a sample leads to an electrical current with current density $\boldsymbol{j}$ which can be described as the motion of electrons with negative charge $-e$ and velocity $\boldsymbol{v}$

$$\boldsymbol{j} = -ne\boldsymbol{v} \tag{2.28}$$

where n is the charge carrier density.

Applying an external magnetic field $\boldsymbol{B}$ perpendicular to the current, the charge carriers are deflected perpendicular to their original direction of motion as well as perpendicular to the applied field. This is due to the Lorentz force which can be written as

$$\boldsymbol{F}_{\mathrm{L}} = -e\boldsymbol{v} \times \boldsymbol{B} \tag{2.29}$$

In the following discussion, the electrical field E_x will be applied along the x-axis, while the magnetic field B_z will be directed along z yielding a current density j_x along x. The Lorentz force then acts along the y-axis. This results in electron motion along the same direction which in turn creates a second electrical field, the so called Hall field E_{H} also directed along y. This field can then be detected in measurements by applying contacts to the sides of the sample along the y-axis. Lorentz force and Hall field counteract and even compensate each other in the stationary case.

The Hall coefficient

$$R_{\mathrm{H}} = \frac{E_{\mathrm{H}}}{j_x B_z} \tag{2.30}$$

is often a constant, since in many cases numerator and denominator of the above fraction are directly proportional to each other. The ratio of Hall field and current density

$$\rho_{\mathrm{H}} = \frac{E_{\mathrm{H}}}{j_x} = R_{\mathrm{H}} B_z \tag{2.31}$$

is called the specific Hall resistivity [88, 89].

Anomalous Hall Effect

Shortly after the discovery of the normal Hall effect (HE), an additional anomalous Hall effect (AHE) was discovered in ferromagnetic materials. The combined specific Hall resistance can be expressed as a combination of both.

$$\rho_{xy} = \rho_{\mathrm{HE}} + \rho_{\mathrm{AHE}} = R_{\mathrm{H}} B_{\mathrm{ext}} + R_{\mathrm{AHE}}(T)\mu_0 M(T, B_{\mathrm{ext}}) \tag{2.32}$$

with R_{H} and R_{AHE} describing the normal and anomalous Hall effect the latter of which describes the relation between anomalous Hall resistance and magnetization M of a ferromagnet [41].

Anomalous Hall effect arises from three different origins, all of which are depicted in Fig. 2.12: the intrinsic Berry phase or the extrinsic skew scattering or side jump.

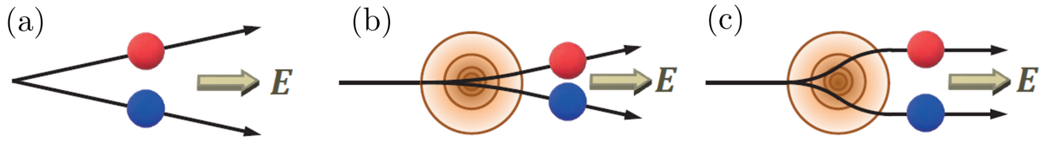

Figure 2.12: Mechanisms leading to anomalous Hall effect. (a) intrinsic (b) skew scattering (c) side jump [41].

The intrinsic mechanism is a consequence of a variable describing the equivalent of the effective magnetic flux density in reciprocal space generating an additional transversal velocity component and thus a dissipation-less Hall current density resulting in the observed AHE [90].

While this mechanism is independent of the materials defect concentration, this is different for the extrinsic origins.

Skew scattering basically is an asymmetric scattering of electrons by impurities and would be expected in nearly perfect crystals. It is directly proportional to the life time of a Bloch state. Spin orbit coupling leads to non-equal transition probabilities $W_{\boldsymbol{k}\to\boldsymbol{k}'}$ and $W_{\boldsymbol{k}'\to\boldsymbol{k}}$ which in turn causes asymmetrical scattering depending on the conduction electrons spin orientation [91].

The side jump mechanism, which is often defined by the difference of the total AHE and the contributions due to intrinsic and skew scattering mechanisms, can only be explained in a quantum mechanical picture. Here, the conduction electrons are shifted along y upon scattering at a defect. Due to symmetry breaking of the spin-orbit coupling, this shift is asymmetric and electrons with different spin orientations are not scattered equally, making this effect antisymmetric as well [92].

2.3 Heat Capacity

The heat capacity at constant volume is defined as the partial derivative of a materials inner energy with respect to the temperature

$$C_V = \left(\frac{\partial U}{\partial T}\right)_V \tag{2.33}$$

where U is the inner energy, T the temperature and V the volume. The heat capacity can also be described as the amount of heat necessary to increase the temperature of a system by a temperature fraction dT.

Experimentally, the heat capacity at constant pressure C_p is often used, as it is easier to access.

$$C_P = \left(\frac{\partial U}{\partial T}\right)_P \tag{2.34}$$

For better comparison, the heat capacity is usually given as $C_{P,\mathrm{mol}} = C_P \frac{M_\mathrm{mol}}{m}$ in units of Jmol^{-1}K^{-1}.

The heat capacity is composed of several contributions which can be electronic, phononic or magnetic.

$$C_P = \gamma T + \beta T^3 + \alpha T^n \tag{2.35}$$

Here, the electronic contribution shows a linear temperature dependence and is described by the Sommerfeld coefficient γ which is determined by the effective mass and density of electrons. As the temperature increases, the electronic contribution becomes less relevant and the phononic contribution, which shows a T^3 dependence, dominates. The coefficient β is material specific and contains the Debye temperature Θ_D. The exponent n of the magnetic contribution depends on the magnetic coupling of a material, for magnons it is $n = 3$.

The phonon contribution describes the lattice contribution from vibrational degrees of freedom and can be explained using the Debye model.

Atoms are treated as quantum mechanical oscillators which are coupled to each other. The frequency dispersion can then be approximated as

$$\omega(q) = vq \tag{2.36}$$

where v is the sound velocity and q the wave vector. The cut off is called the Debye frequency ω_D and depends on the number of atoms in a solid [46].

The heat capacity can then be described as

$$C_V = \left(\frac{\delta U}{\delta T}\right)_V = 9Nk_\mathrm{B}\left(\frac{T}{\Theta_\mathrm{D}}\right)^3 \int_0^{x_\mathrm{D}} \frac{x^4 \exp(x)}{(\exp(x)-1)^2} dx \tag{2.37}$$

with the Debye temperature $\Theta_\mathrm{D} = \hbar\omega_\mathrm{D}/k_\mathrm{B}$ as a material specific parameter giving information about the temperature region relevant for the investigated material. For $T \ll \Theta_\mathrm{D}$ the heat capacity can be approximated as $C_V \sim (\frac{T}{\Theta_\mathrm{D}})^3$. For lowest temperatures, this contribution becomes very small.

Nuclear contributions are described by $C_\mathrm{nuc} = \frac{\alpha}{T^2}$ where α measures the splitting of nuclear levels.

As for magnetic contributions, magnets with antiferromagnetic order are expected to show a $C_m \sim T^3$ behaviour (3D) with gapless excitations. Gapped excitations are described by $C_m \sim e^{-\Delta/T}$ with an excitation gap Δ in the energy spectrum [46, 93].

3 Experimental Methods

In the following chapter the different experimental methods used in this thesis will be explained. Sample characterization was done via x-ray and Laue diffraction as well as energy dispersive x-ray spectroscopy (EDX). A FIB-SEM dual beam system was used in order to prepare devices for electrical transport measurements as well as controlled thinning of crystals for X-ray diffraction experiments. The physical and magnetic properties of the samples were investigated using a Magnetic Properties Measurement System (MPMS) for magnetization measurements as well as a Physical Properties Measurement System (PPMS) for both heat capacity and electrical transport measurements.

3.1 X-ray Powder Diffraction

X-ray diffraction (XRD) is a well known and often utilized technique for characterizing crystallographic structures.

In the frame of this work, powder x-ray diffraction measurements were performed using a Rigaku Miniflex (Cu-K$_\alpha$, $\lambda = 1.5406\,\text{Å}$, $U = 40\,\text{keV}$, $I = 15\,\text{mA}$) [94]. Here, monochromatic light is used. The x-ray source and detector are located opposite each other with the sample placed in between. Both sample holder and detector rotate in order to vary the incident angel θ (Bragg-Brentano geometry).

A single crystal consists of layers made up of atoms in distinct positions, which can be subdivided into so called lattice planes which run parallel to each other with a distance d, as can be seen in Fig. 3.1. The incident x-rays experience interference due to the contact with the atomic planes upon leaving the crystal.

X-rays diffracted on different atomic planes show a path difference Δ. If $\Delta = n\lambda$ with n being an integer value is fulfilled, constructive interference occurs resulting in characteristic peaks at sample specific angles. The Bragg equation describes the relation between the incident angle θ of the x-rays, wavelength λ and plane distance d:

$$n\lambda = 2d\sin(\theta) \tag{3.1}$$

For constant wavelength, the diffraction angle depends solely on the plane distance giving information on the lattice of a crystal and allowing for the determination of lattice parameters as well as crystal symmetry. The intensity

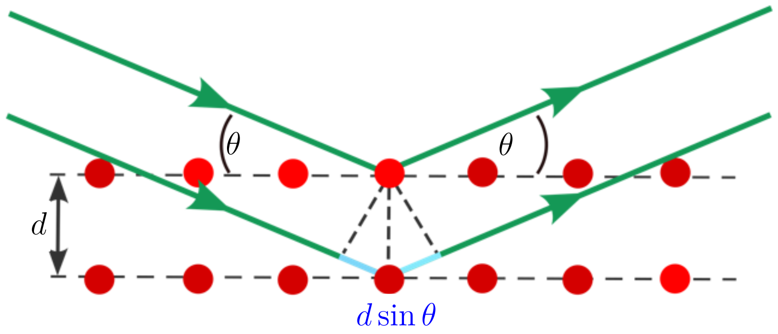

Figure 3.1: Schematic depiction of the Bragg reflection. Adapted from [95].

of detected peaks is determined by the type and placement of atoms within the sample. However, it can be influenced by several factors such as arrangement of the apertures, temperature or the sample volume which needs to be taken into consideration upon data evaluation. By analysing the diffraction angle, intensity and line shape, information about the lattice plane distance is gained from which the symmetry and dimensions of the materials unit cell can be gained.

For powder measurements the single crystals are ground into fine grains using a mortar and pestle. The powder is then placed centrically onto a sample holder using vacuum grease and distributed on the surface by lightly tapping on the side of the sample holder. Here, a statistical distribution of the powder with no preferred orientation is crucial. If this is the case, all lattice planes contribute to the specific peaks and can be used for analysis.

3.2 Laue Back-Reflection

The Laue method poses a good tool to learn more about a crystals symmetries as well as the location of the crystal axes. Unlike other x-ray diffraction methods, Laue can only be performed using single crystals. Non-monochromatic x-rays are used, meaning that Bragg's law is fulfilled by several lattice planes simultaneously. This makes the Laue method a comparably fast characterization technique. The crystal structure of a sample can then be determined by analysing the position of the obtained reflections [96]. Laue measurements can be done in transmission or back reflection geometry. For the latter, the schematic set-up is shown in Fig. 3.2. Here, it is necessary to have a detector through which x-rays can pass unhindered.

For the Laue images referenced in this thesis a Philips PW1830/40 x-ray generator with tungsten anode and Photonic Science detector was used.

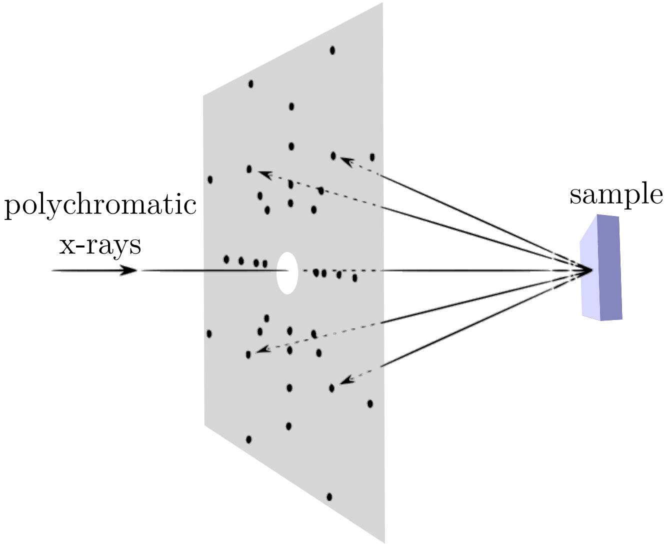

Figure 3.2: Set-up of a back-scattering Laue experiment. Adapted from [97].

3.3 FIB-SEM

A combined FIB-SEM set-up, sometimes also referred to as Dual Beam or CrossBeam, allows for the imaging and microstructuring of a plethora of materials. Cutting of precisely defined structures as well as removing small slices of a sample for further analysis are only two of many possible applications. A schematic sketch of the setup is shown in Fig. 3.3.

Focused Ion Beam

The following section is based on [98].

A focused ion beam basically uses high energy ions of a heavy element which can also be stored in the form of a liquid-metal ion source. Here, a very commonly used metal is gallium. Due to its low melting point, very little heating is required to access the metal in its liquid state. Secondly, gallium has a low volatility at the melting point which translates into a long source life (roughly 400 µAh/mg). As a result of its low volatility around the melting point, gallium can also be used in its pure form instead of working with some kind of alloy, which would have to be separated into its elemental components before being used for FIB processing. Furthermore, milling of heavier elements is possible due to the sufficiently high mass of gallium itself. All of these advantages make gallium the most commonly used ion for focused ion beam systems.

In order to create a focused ion beam, the gallium source is first heated to temperatures close to the boiling point. The liquid metal then flows onto a very

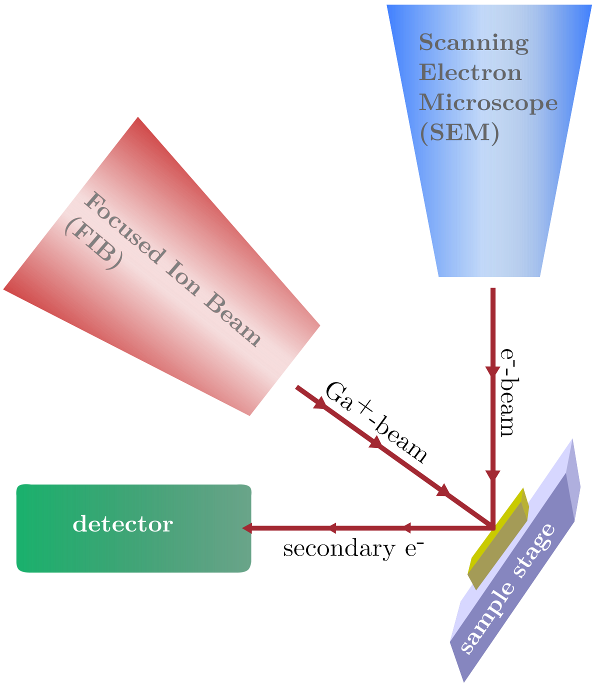

Figure 3.3: Schematic of the combined FIB-SEM setup. For milling, the sample is tilted at a 54° angle compared to the incident electron beam which corresponds to the surface being perpendicular to the incident Ga^+-ion beam. Secondary electrons are captured by a detector yielding a high resolution image of the sample surface.

sharp tungsten needle (2-5 µm tip width) where the extractor, a ring-shaped electrode positioned concentric to the needle tip, draws the Ga atoms further along the needle towards the tip. An electric field is created by the potential difference of the aperture and needle which in turn leads to the acceleration of energetic ions in close proximity to the tip towards the extractor. Due to the balance of surface tension and electrostatic force the liquid metal forms a so called Taylor cone, the tip of which has a diameter of no more then 5 nm. Gallium can then be pulled from the cone tip and ionized using the extractor voltage of the aperture. Finally, the Ga ion is accelerated down the ion column. This is called the extraction current. Typical emission currents are in the range of 1-3 µA which allows for a stable beam and lowers the probability of dimer or trimer droplet formation which would negatively impact the source lifetime [95].

The beam is regulated by a suppressor as well as an extractor. The suppressor voltage regulates the extraction current and also supports the extractor in maintaining a constant beam current by applying an electric field. A set of apertures and lenses is used to direct the beam onto the sample surface in a scanning pattern using electrostatic and magnetic fields to do so. If the ion-atom collisions are elastic, sample material is removed from or added to the surface. This process is called milling or sputtering, respectively. Inelastic scattering on the other hand results in the emergence of secondary electrons which can be captured by a detector and then used for imaging. The basic applications of a FIB are imaging, milling, deposition and implantation and will be discussed in further detail in the following paragraphs.

Imaging Analogous to the electron beam used for SEM imaging, the FIB can be used to generate an image of the sample surface. Energy from the ion beam is transferred to some surface electrons allowing them to leave the material. Most of these secondary electrons originate from a spherical area around and under the beam spot. Topological features yield an increase in escaping electrons, resulting in an image which reflects the height profile of the sample.

Milling Milling describes the precisely controlled removal of sample material via focused ion beam. The focused ion beam is therefore directed in a scanning pattern over the surface. The rate, geometry and depth of sample removal can be controlled by adjusting the used current and voltage as well as several other parameters. This allows for the creation of devices with defined geometries suitable for TEM analysis, resistivity measurements or diffraction studies. However, during this process some gallium atoms are embedded into the sample surface which later need to be removed again.

Deposition Material can be deposited on the sample surface by combining a FIB with a gas injection system (GIS). The material which is to be deposited is stored in an organic matrix which is then released as a gaseous cloud in close proximity to the surface. There the atoms collide with those of the focused ion beam, resulting in a transfer of kinetic energy. Upon surface impact the atoms are absorbed via Van der Waals forces. Both insulating (e.g. SiO_2) and conductive (e.g. Pt) materials can be deposited in this manner making it a rather useful procedure for nano-structuring. As for milling, the area of deposition as well as the thickness of the deposited layer can be precisely controlled by choosing the FIB parameters in the desired fashion. However, due to the use of an organic matrix, the deposited material does not consist of the pure element or molecule, but also contains high percentages of for instance carbon and thus the deposited material can be rather porous, as is the case for FIB Pt, and somewhat difficult to work with.

Implantation Unlike an electron beam which has no damaging effect onto the sample surface, the ions, having a higher mass, do penetrate the surface and embed themselves while removing surface atoms. While in case of milling this allows for precise structuring and removal of sample material, at the same time implantation of gallium can result in a change of electronic properties which is especially relevant in case of devices prepared for electrical transport measurements. Particularly at higher currents which correspond to faster milling but also increased penetration depth, ions can be implanted which then later on need to be removed again by „showering“ the surface with low voltage, low current ions.

While a FIB can be used on its own, using a combined FIB-SEM poses several advantages. Whereas FIB imaging inherently causes some degree of surface damage, surfaces investigated by electrons do not suffer similar problems at such a large scale. Furthermore, a combined set-up allows for the simultaneous milling and imaging allowing even better control over the structuring process.

Scanning Electron Microscope

The following section is based on [99, 100].

A scanning electron microscope offers a way of non-destructive imaging of very small objects in the micrometer range. For good samples and conditions, image resolution can reach as high as some ten nanometres. It consists of two main components: a vacuum chamber and an electron gun. The basic principle can be described as follows: A cathode is heated, thus emitting electrons which are then focused into a beam and accelerated using a suitable aperture. A set of magnetic lenses is used to further focus the electron beam. The sample surface is then scanned by using deflection coils to direct the beam in a line pattern. Interactions between sample and electron beam can then be measured by a set of detectors and processed into images. Image resolution is dependent on the used wavelength with smaller values resulting in higher image quality. The electron penetration depth depends on the chosen acceleration voltage as well as the sample composition yielding a variety of resulting phenomena such as back scattering, secondary or Auger electrons as well as characteristic x-ray radiation or bremsstrahlung. The spatial distribution of these phenomena shows a pear shaped cone oriented perpendicular to the sample surface. In case of elastic scattering, back scattered electrons (BSE) are emitted yielding information about the atomic distribution and material contrast of the sample. If inelastic scattering occurs, where the primary electron hits a surface atom and causes an electron to leave its orbital, secondary electrons are emitted revealing information about the sample topography such as edges or tilted surfaces as more secondary electrons are emitted at such structures due to the changed incidence angle resulting in a brighter image.

Sample Preparation using a FIB-SEM set-up

Besides the preparation of TEM lamellae, a FIB-SEM set-up is often used to prepare devices with controlled geometry and contact arrangement for electrical transport measurements. This process will be described in the following section. Since this method was mainly applied to Na_2IrO_3, this material will be used as an example here.

First, a suitable crystal is glued onto a sample holder using silver epoxy in order to ensure good conductivity and avoid charging effects later on in the preparation process. As a lamella is cut perpendicular to the sample surface, the crystal needs to be oriented along the desired cutting axis. Due to the platelet shape of Na_2IrO_3 all crystals were cut perpendicular to the ab-plane. As Na_2IrO_3 is a rather bad conductor, a path of silver epoxy was laid along the surface right up to the cutting area. The preparation of samples for resistivity measurements is adapted from TEM lamella preparation, however larger lamellas with dimensions of about $150 \times 50 \times 3\,\mu m$ are cut. After making sure the sample is located in the eucentric point at an ideal working distance, which in our case is 5 mm, the sample holder is tilted by 54° resulting in the sample surface being oriented perpendicular to the focused ion beam. Cutting areas are defined by overlaying the FIB image with a pattern design including current, voltage, shape, lateral dimensions and desired cutting depth. Fig. 3.4 gives an overview over the preparation process.

First, two mirror-symmetrical trapezoidal trenches with a 10 µm distance are cut resulting in a bar with a thickness of some µms (Fig. 3.4(a)). Due to time constraints this is done with a rather large aperture (30 kV, 30 nA or in some cases even 65 nA). Higher currents and voltages equal faster milling, but also less precise cutting and increased surface damage, as the penetration depth of Ga atoms is proportional to the used voltage. In the second step the bar is further thinned by using rectangular patterns on either side with smaller currents of 3 or 7 nA. Further cutting is done under an angle of about 2° relative to the FIB beam, as cutting is less efficient with increasing depth which would result in the cut bar widening towards the bottom and thus needs to be corrected in order to achieve a homogeneous thickness. Once the desired thickness is reached, the lamella is separated from the crystal by undercutting at a higher angle (4° relative to the FIB beam), shown in Fig. 3.4(b), leaving only a small connection to the bulk crystal. Next, the sample is removed from the bulk crystal either in-situ or ex-situ. In the first case, a micromanipulator is used inside the FIB chamber. There, a needle with a thickness of less than 5 µm is carefully moved towards the lamella until contact is made. A gas injection system (GIS) is then used to deposit platinum on the contact attaching the lamella to the needle. However, the

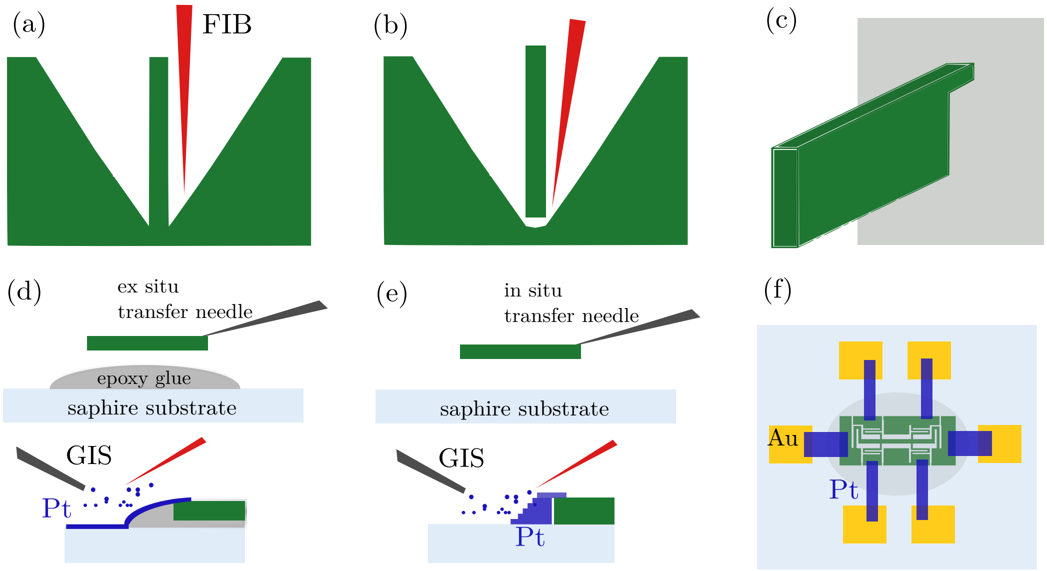

Figure 3.4: Preparation process of a FIB lamella (a-c) with transfer done either ex-situ (d) or in-situ (e). (f) shows an example of a structured lamella (green) glued onto a substrate (blue) using epoxy (grey) used for four wire resistivity measurements. Partially adapted from [101].

platinum used in this process is not pure metal but contains a high percentage of carbon and other contaminants making it rather brittle [102, 103]. Thus, careful handling is required, as severing the connection by accident once the lamella was cut free from the bulk can then easily result in the loss of the lamella. After cutting the bridge, the lamella is moved up by slowly retracting the needle and lowering the bulk crystal. The lamella then needs to be rotated by 90° in order to be placed on a substrate. This is not possible using only the needle, as the center of the tip is not equivalent to the rotation center of the micromanipulator. Thus, the lamella is attached to a TEM grid mounted on a rotating sample holder. The needle is cut free and retracted, so that the lamella can be rotated and then be reattached to the needle. Now the lamella surface is aligned parallel to the substrate surface and can be lowered down (see Fig. 3.4(d)). Here, both SEM and FIB imaging are used to estimate the distance of the lamella to the surface, as contact has to be achieved very slowly and carefully. An abrupt contact with the substrate surface often results in the lamella breaking off from the needle and getting displaced somewhere in the FIB chamber from where it cannot be retrieved. A good way to estimate the distance is to look at the shadow the lamella casts onto the substrate. Once contact is achieved, the lamella is attached to the substrate using the Pt-GIS, before the needle is cut free and retracted. Now the sample can be structured using Pt to grow contacts and FIB cutting to shape it in the desired stoichiometry. In some cases, the substrates already contained predeposited contact pads created by gold sputtering which are connected to the lamella via further platinum deposition ending in large enough gold areas, that manual contacting with Pt wires and silver epoxy is possible.

In order to minimize resistance and achieve good contact, the Pt contacts are grown in terrace-like steps and contact to the lamella is only made once the Pt construct reaches the same height, as can be seen in Fig. 3.4(e).

As shown in Fig. 3.4(d), lamellae can also be transferred ex-situ. In this case, an optical microscope is used along with a micromanipulator. The main differences here are the sample being exposed to air in the process and the lamella being held by electrostatic forces instead of platinum. Furthermore, the lamella is not placed directly onto the substrate, but rather on a small drop of quick-curing epoxy where, if done carefully, surface tension is sufficient to keep it afloat. The sample is then sputtered with gold which is later removed again via FIB processing in order to get the desired contact geometry. The epoxy-embedded lamella can technically also be contacted via Pt deposition. However, considering the insulating nature of both sample and epoxy this can proof rather difficult due to charging effects resulting in overexposure of the recorded image or increased sample drift meaning the platinum contacts are not deposited at the desired locations. This can be avoided, if a conductive path from the lamella to the sample holder is made.

Sample structuring as well as cutting down to the final desired thickness is done with small apertures below 300 nA to allow for very precise cutting and avoid further surface damage. Low voltage FIB milling is used to remove the embedded Ga ions from the surface, before EDX is used to check the surface for any remaining Ga contamination which could significantly influence the transport properties of the prepared device. An example for such a structure is depicted in Fig. 3.4(f).

Due to Na_2IrO_3 already growing as thin platelets a third contacting option using a FIB technique was employed for some samples. Here, the crystal was mounted directly on the substrate again using epoxy glue. To get a fresh and clean surface, the sample was then cleaved inside an argon filled glovebox. For Na_2IrO_3 this can be done using commercially available adhesive tape, since the material cleaves both nicely and easily due to its 2D structure. Transport to a gold sputter was possible without any air exposure using a transport box specifically designed for this purpose by M. Sc. Fabian Hirschberger which can be sealed by evacuating the glove box antechamber and the lid removed inside the sputter chamber using a magnet. The gold coated sample was then transferred into the FIB chamber where gold was removed again from the bar shaped measurement area. Trenches were cut all the way through the crystal towards the crystal edges in order to create defined contacts for a four point measurement which were then manually contacted using Pt wires and silver epoxy before being loaded onto the resistivity puck. A sample prepared in this fashion is depicted in Fig. 3.5. As no lamella needs to be cut, thinned and transferred first, and the risk of losing or damaging the sample in the process is much lower, this method is far quicker (1 day total preparation time on average) compared to lamella preparation (2-3 days) and was thus used for most samples after initially cutting lamellae for the first few experiments.

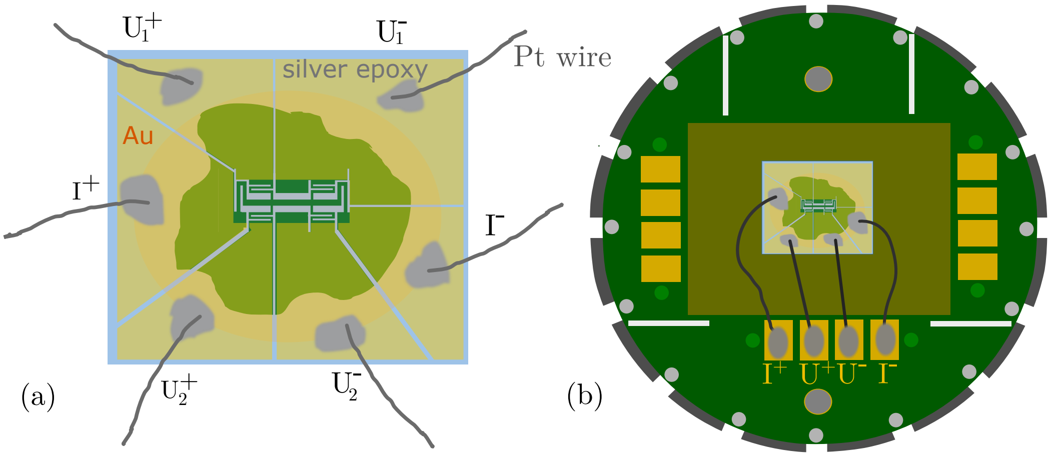

Figure 3.5: Left: Schematic of a structured crystal (green) on a sapphire substrate (light blue) covered with gold. Trenches were cut in such a way that the sample can be contacted for a four wire measurement of both longitudinal as well as Hall resistivity. Right: Schematic drawing of the sample mounted on a standard PPMS puck for transport measurements. Contact between puck and sample is made using Pt wires and silver epoxy.

3.4 Energy Dispersive X-ray Spectroscopy

Energy Dispersive X-ray Spectroscopy (EDX) measurements were performed using a scanning electron microscope (SEM), type Merlin Gemini 2 from Zeiss, combined with an EDX probe with an X-Max 80N SDD detector from Oxford Instruments.

Energy Dispersive X-ray Spectroscopy is a method which allows the user to determine the stoichiometric ratio of elements in single crystal or powder samples as well as map the distribution of each element over the sample surface. However, there are several limitations to this method. For one, even though elements with an atomic number $Z < 11$ can be detected by EDX, accurate quantitative analysis is difficult, making Na the lightest detectable element. This is due to the beryllium window conventionally used in EDX detectors which hinders the detection of the characteristic x-rays emitted by the lighter elements [104]. Though some instruments using windowless detection methods allow detection of elements with Z as low as 4, such equipment was not available in the frame of this work. Secondly, EDX is limited to the surface with penetration depths in the order of 1 µm or less depending on the atomic number of the relevant elements as well as the density of the investigated sample and the applied acceleration voltage. Fig. 3.6 depicts the pear shaped interaction volume of the incoming electrons with the sample where the majority of scattered electrons are located. The depth of the analysed region can be estimated using Castaings formula [105]

$$z_\mathrm{m} = 0.033(E_0^{1.7} - E_\mathrm{C}^{1.7})\frac{A}{\rho Z} \tag{3.2}$$

where E_0 is the accelerating voltage, E_C the minimum emission voltage, A is the atomic mass, Z the atomic number and ρ the density.

The EDX detector is calibrated in such a way in relation to the SEM gun, that the sample needs to be located in a set working distance in relation to the gun in order to be accurate. The working distance can be determined by focusing the SEM image on the sample surface and then moving the sample holder in z-direction until the desired working distance is reached. Furthermore, in order to obtain an accurate stoichiometry, the investigated surface needs to be exceptionally flat and ideally polished. Otherwise, large errors in some cases as high as 20 % of the expected value can be observed, as determined from measurements on unpolished versus polished crystalline samples. Lastly, it is not possible with our means to accurately investigate the presence of oxygen in the samples. On the one hand, standards for comparison would be required, on the other hand, both oxygen and carbon deposits can always be found on samples handled in air, which cannot be avoided since the sample needs to be transferred into the SEM chamber where at least brief air exposure is inevitable.

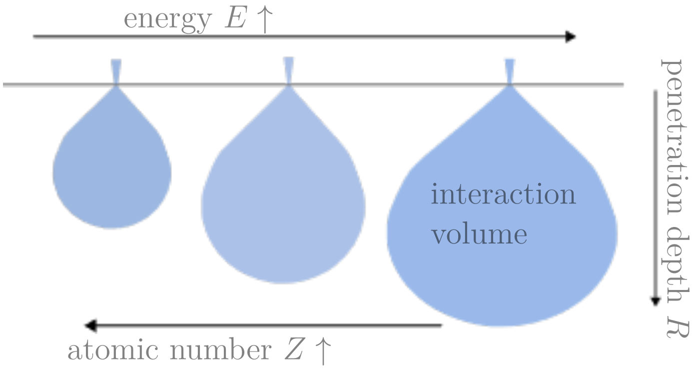

Figure 3.6: Schematic dependence of the penetration depth on energy and atomic number. The interaction volume of the incoming electrons is pear-shaped.

The basic principle of EDX is as follows [99]: Ionizing atoms leads to the emergence of electrons, which in turn leave behind unoccupied shells. Electrons from higher shells can then jump into such unoccupied spots. During this process, x-rays are emitted, the wavelengths of which are characteristic for each element. Furthermore, primary electrons are slowed down in the Coulomb field of the surrounding atoms which results in the emission of the so called bremsstrahlung. The resulting spectrum combines both the characteristic lines and continuous Bremsspectrum and thus allows for the analysis of the elemental composition of the sample. The ratio of elements can be determined from the ratio of intensities of the characteristic lines. An example for such a spectrum can be seen in Fig. 3.7(a). Recording a point spectrum for each pixel and combining it with the corresponding SEM image yields a map depicting the distribution of elements over the surface showing possible inhomogeneities or inclusions, an example of which is depicted in Fig. 3.7(b). Such a map can be displayed either in terms of absolute counts or in terms of normalized atomic or weight percentages for the relevant elements.

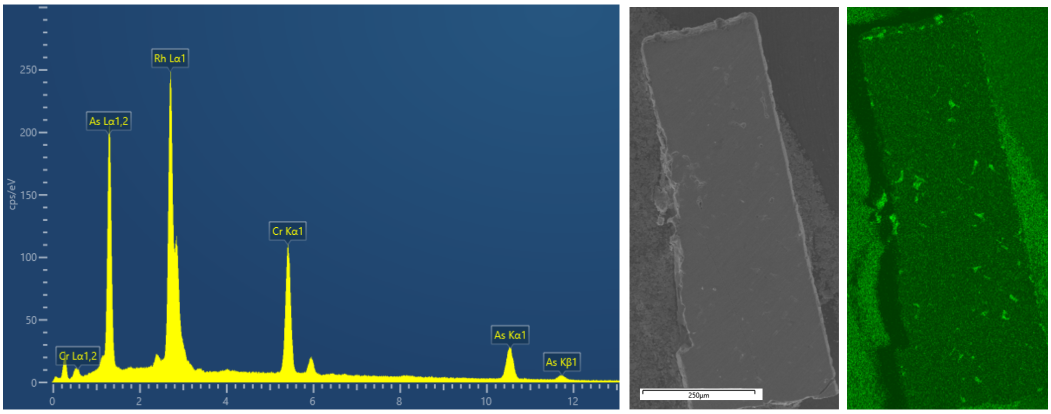

(a)

(b)

Figure 3.7: (a) Exemplary EDX spectrum of a CrRhAs single crystal. The unlabelled peaks can mostly be attributed to some Bi flux remaining on the sample surface. The peak at lowest voltage stems from a small carbon contamination which can not be avoided. (b) SEM image (left) and elemental distribution map (right) of a Yb_4CoGe_8 crystal showing some remaining In flux (bright spots) on the surface.

3.5 Magnetization

The following section is based on [106].

Measurements of the temperature- or field-dependent magnetization were performed using a Magnetic Properties Measurement System MPMS-3 by

Quantum Design. Measurements with applied fields of up to 7 T are possible for temperatures in the range of 1.8-300 K.

The basic setup of the MPMS consists of a set of coils, as shown in Fig. 3.8. An external magnetic field is applied. During the measurement, a change in the magnetic field of the induction coil is caused whenever the sample moves through a detector ring. This detector ring, also known as gradiometer, is made up of three single coils, the two outer of which are wound in opposite directions, thus cancelling out any signal stemming from the coils themselves and only leaving the sample signal. A good indicator of the signal quality is its symmetry.

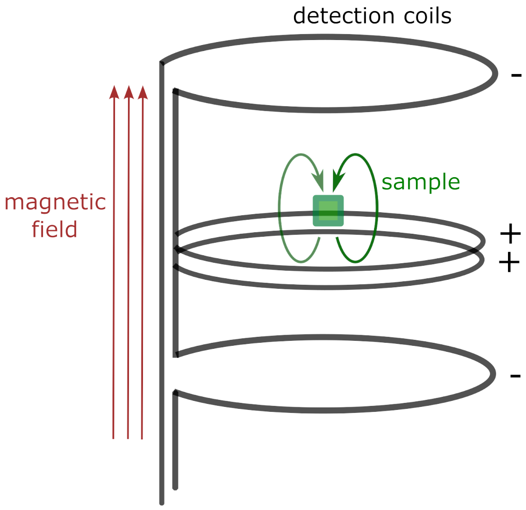

Figure 3.8: The standard set-up for a magnetization measurement contains a set of detection coils within which the sample is located. Movement of the sample causes a change in the detected magnetic field. Adapted from [107].

A SQUID (Superconducting Quantum Interference Device) magnetometer allows for the detection of even the smallest changes in the magnetic signal of the sample. It consists of a superconducting ring which is interrupted by one (rf) or two (DC) thin, non-superconducting layers with a thickness of about 1 nm allowing for the tunnelling through of Cooper pairs. A small current in the superconducting coil is induced, when the sample is moved inside the sample chamber, resulting in a voltage drop in the Josephson contacts which is then transformed into a detectable voltage signal. Using this technique signals with values as low as 10^{-6} emu can be detected which allows for the measurement of either very small samples or samples with weak magnetic signals. As the SQUID is extremely sensitive to magnetic fields, it is located at a considerable distance from the magnet in order to ensure good shielding from any disturbances.

3.6 Electrical Transport

Measurements of the electrical transport were performed using an ETO option for the PPMS by Quantum Design [108]. Each sample holder offers two separate channels which allow for the simultaneous measurement of two samples. Contacting can be done via two wire or four wire method and the measurement parameters chosen accordingly. Contacting the same sample on both channels however might lead to errors in resistance due to stray capacitance and should thus be avoided. Resistance is measured by applying a sinusoidal AC drive current and recording the AC response using a current amplifier. Measurements can be performed in a range of 1 nA-1000 mA with applied frequencies of 0.1-200 Hz. U-I-characteristics can be recorded either in a four wire geometry by applying a current excitation waveform and measuring the voltage response or vice versa for two wire contacting.

The relation between resistance R, voltage U and current I is described by Ohm's law

$$R = \frac{U}{I} \tag{3.3}$$

The resistivity is a material specific parameter and can be calculated as follows from resistance if the contact distance l as well as the cross sectional sample area A are known.

$$\rho = R\frac{A}{l} \tag{3.4}$$

Ideally, the sample should be bar shaped or at least approach a rectangular geometry The current contacts should be located on two opposite sample edges. Voltage contacts should be placed in a region between the current contacts where the electric field lines are straight. All four contacts should be aligned. Contacts must not touch, otherwise the contact resistance will be included in the measured signal or a short circuit can occur.

Hall measurement

In order to experimentally determine the Hall coefficient, ideally a set-up as depicted in Fig. 3.9 is used. The sample should be thin and rectangular in shape. Contacts are made on the sample edges in x direction in order to apply a current. Contacts on the sides of the sample (along y) then allow for a measurement of the Hall contribution. Additional contacts along x can be attached and used to measure the longitudinal resistivity in a four wire set-up.

Using $j_x = \frac{I}{b \cdot d}$ where d is the sample thickness and b the sample width as well as $E_\mathrm{H} = \frac{U_\mathrm{H}}{b}$ where U_H is the Hall voltage, one gets

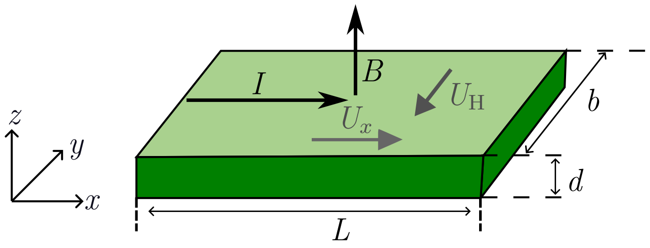

Figure 3.9: Set-up for a Hall effect measurement. Applying a current I along x and a magnetic field B along z leads to a Hall voltage U_{H} along y.

$$U_{\mathrm{H}} = R_{\mathrm{H}} \frac{I B_z}{d}. \tag{3.5}$$

The resistance can then be written as

$$R(B) = R_{\mathrm{H}} \frac{B_z}{d} \tag{3.6}$$

which only depends on rather easily measurable parameters.

Depending on the sign of the Hall resistance, the charge carriers are either electrons (negative sign) or holes (positive sign) [109].

Once the Hall coefficient is known, the charge carrier density n can be determined by

$$n = \frac{1}{qd} \cdot \frac{B}{R_{\mathrm{H}}} = \frac{1}{qd} m_{\mathrm{H}}^{-1} \tag{3.7}$$

where q is the electron charge and m_{H} the slope of $R(B)$.

Ideally the Hall contacts should be perfectly orthogonal to the direction of the applied current. Since this is not possible in a real experiment, the transversal resistance always contains a longitudinal contribution. In order to obtain the pure Hall resistance, the data needs to be antisymmetrized:

$$R_{\mathrm{H}}(B) = R_{\mathrm{asym}} = \frac{R(B_i) - R(-B_i)}{2} \tag{3.8}$$

The longitudinal contribution can be obtained by symmetrizing the data according to

$$R_{\mathrm{sym}}(B) = \frac{R(B_i) + R(-B_i)}{2} \tag{3.9}$$

The material specific resistivity can then be calculated using

$$\rho = R \frac{bd}{L} = R \frac{A}{L} \tag{3.10}$$

where A is the cross-sectional sample area and L the sample length or distance of the current contacts.

3.7 Heat Capacity

Measurements of the heat capacity were performed using a Physical Properties Measurement System (PPMS) by Quantum Design [110]. Here, the relaxation method under closed adiabatic conditions is applied. The sample is heated for a set period of time, then cooled, while the change in temperature is recorded. The temperature response is then fitted taking into account the thermal relaxation between sample and platform as well as platform and bath temperature. For addenda as well as most measurements, the simple model is used:

$$C_{\mathrm{tot}}\frac{\mathrm{d}T}{\mathrm{d}t} = -K_w(T - T_{\mathrm{b}}) + P(t) \tag{3.11}$$

Here C_{tot} is the total heat capacity of sample and platform, K_w the thermal conductance of the supporting wires, T_b the bath temperature and $P(t)$ the power applied by the heater which equals P_0 during heating and is equal to zero otherwise. The solution for this model is an exponential function with a characteristic time constant τ. The heat flowing between sample and platform as well as platform and puck can be simulated using a Two-Tau-Model. Here, the heat capacity is assumed to be nearly constant within the temperature range of a single measurement.

The sample is mounted onto the sample puck using Apiezon N grease to ensure good thermal contact. The puck consists of a platform to which both thermometer and heater are connected. The addenda of the grease and sample puck is measured separately, then subtracted from the sample measurement.

Measurements can be done in a temperature range of 1.9-400 K. Down to 4.2 K liquid helium is used, for even lower temperatures the vapour pressure is lowered by pumping. Measurements at temperatures as low as 0.35 K are possible using a He-3 option by Quantum Design, which uses pumped ^{3}He to achieve these low temperatures. Here, a different platform is used in order to minimize thermal contact to the surrounding. For example, only four wires are used compared to eight for some pucks used for regular heat capacity measurements. The sample is mounted in an insert which is then placed inside the PPMS chamber. As the sample is mounted upside down, the sample holder is covered by a cap to catch the sample if it should fall.

4 Domain wall electrical conductivity in Na_2IrO_3

The first materials suggested by Jackeli and Khaliullin as candidates for realizing the Kitaev model in real materials were Li_2RuO_3 and Li_2IrO_3 [59]. Experimental work on Na_2IrO_3 was first published in the following year by Singh et al. [111], closely followed by the suggestion of the material being another candidate for the realization of the Kitaev model by Chaloupka et al. [60]. The large atomic mass of the Ir^{4+} ions in iridates was found to give rise to strong spin-orbit coupling in the order of 0.4 eV [61, 112, 113] which is of similar magnitude as the Coulomb repulsion for $5d$ electrons. The sixfold degeneracy of the t_{2g}-states of the $5d^5$ electrons of Ir^{4+} in an octahedral crystal electric field is broken by spin orbit coupling. This results in a filled $j_{\mathrm{eff}} = 3/2$ and a half filled $j_{\mathrm{eff}} = 1/2$ band. For a reduced bandwidth of the $j_{\mathrm{eff}} = 1/2$ band a Mott gap can easily form already for small Coulomb repulsion resulting in a $j_{\mathrm{eff}} = 1/2$ spin orbit Mott insulator with bond-directional exchange interactions [60], as is the case for Na_2IrO_3. Even though Na_2IrO_3 orders antiferromagnetically at around T_{N}=15 K [111, 114, 115], Kitaev interactions are dominant at temperatures above the ordering [116–118].

Generally, systems with strong spin orbit coupling are promising candidates for finding new quantum states. An example for this would be topological insulators showing topologically protected conducting surfaces states [119]. In theory, charge carrier doping can be used to tune spin orbit Mott insulators such as Na_2IrO_3 into a metallic state. Looking at existing materials, an example for this would be the isostructural perovskite compounds Sr_2IrO_4 and La_2CuO_4. While the former is a spin orbit Mott insulator with $j_{\mathrm{eff}} = 1/2$, the latter is a $s = 1/2$ Mott insulator while also being a parent compound for high temperature superconductivity. Electron-doped $(Sr_{1-x}La_x)_2IrO_4$ was reported to show signatures of a pseudogap in STM (scanning tunnelling microscopy) as well as ARPES (angle-resolved photoemission spectroscopy) measurements [120, 121]. However, no fully metallic or superconducting electrical transport has been reported so far. Previous measurements of the electrical transport of bulk Na_2IrO_3 showed three dimensional variable range hopping stemming from carriers localized by disorder [111, 122, 123]. Several measurements further suggested the possibility of enhancing the surface conductivity, such as ARPES measurements reporting an in-gap feature indicating a metallic surface state [124]. However, this was disputed in a later publication, where the feature was ascribed to the dispersive states in the sodium terminated cleavage planes approaching the Fermi level [125]. Dziuba et al. reported a reduced resistivity for freshly cleaved crystal surfaces measured in UHV as well as three different types of tunnelling spectra attributed to different surface reconstructions as well as a V-shaped closing of the bandgap attributed to surface states [126]. Another study on the electrical resistivity of Na_2IrO_3 surfaces etched with argon plasma, however, showed a first-order density-wave-like transition at around $\sim$220 K, while Fermi liquid behaviour occurred below 20 K [127].

To sum it up, to this point several studies performed on Na_2IrO_3 exist pointing towards a high tunability of the materials electronic properties. Thus, in the following chapter the results of an in-depth study looking at the structural as well as electrical properties of Na_2IrO_3 single crystals will be presented. Structural analysis was performed using Laue as well as SEM and EDX measurements. Electrical transport behaviour was investigated on FIB structured samples and compared to previous measurements on bulk samples. Furthermore, this chapter looks at Na deficiency in structural domain walls observed on crystal surfaces and the influence of such a deficiency on the electrical transport.

4.1 Crystal Growth

Platelet-shaped crystals of Na_2IrO_3 with a diameter of up to several millimetres and a thickness of up to 100 µm can be grown via a combination of solid state synthesis and calcination. This established [111] and optimized [128] multi-step synthesis begins with mixing the starting materials Na_2CO_3 and Ir in a stoichiometric ratio of 1.05:1. Here, an excess of 5% Na_2CO_3 is added in order to compensate the material loss during heating due to the volatility of sodium. After grinding the starting material for several minutes, the powder is placed in an Al_2O_3 crucible, covered with an Al_2O_3 lid and heated to 800°C in a muffle furnace for one day. This is followed by cooling down, grinding the powder to improve intermixing and thus quality and baking at 900°C for 3 days. This cycle is then repeated a total number of four times. A lid is placed on top of the crucible in order to minimize mass loss during heating. In between steps, the powder quality is checked by XRD. In the last step, an additional 10% Ir is added to the powder, which has been found to increase crystal size [129], then the sample is heated to 1050°C and held at this temperature for 2 weeks. Upon retrieving the crucible from the furnace, crystals as shown in Fig. 4.1(a) have formed. Fig. 4.1(b) displays once again the full temperature profile.

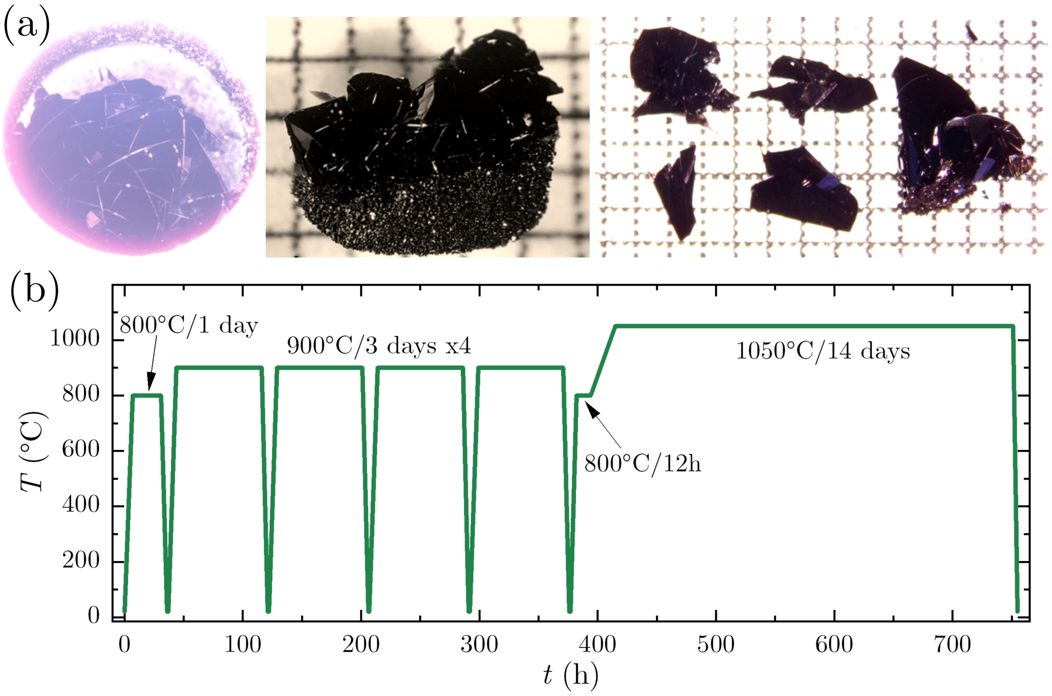

Figure 4.1: (a) Typical crystals of Na_2IrO_3 in and outside of the crucible. (b) Temperature profile used for the crystal growth of Na_2IrO_3.

Due to known surface degradation upon prolonged exposure to CO_2 and H_2O [130], the crystals are stored in a glovebox. Since the layers are only weakly bound, Na_2IrO_3 can be cleaved both nicely and easily using duct tape uncovering fresh, shiny surfaces.

4.2 Structural and Chemical Analysis

First, a brief summary on the crystal structure of Na_2IrO_3 shall be given here, as it will become relevant for the analysis of the Laue data presented later. The crystal structure of Na_2IrO_3 is monoclinic with a C2/m symmetry. There are three different Na and one Ir position, which along with the two O positions are listed in Tab. 4.1. Its lattice constants are $a = 5.427(1)$ Å, $b = 9.395(1)$ Å and $c = 5.614(1)$ Å. Sodium iridate consists of alternating layers of $NaIr_2O_6$ and pure Na, as can be seen in Fig. 4.2. The iridium atoms in the *ab*-plane are arranged in a honeycomb structure with a Na atom in the center of each honeycomb. Due to trigonal distortions of the IrO_6 octahedra, the Ir-O-Ir bond angle deviates slightly from the ideal value of 90° and is reported to be around 98-99.4° [114] resulting in slightly different Ir-Ir distances in the range of 3.130-3.138 Å.

atom	site	x	y	z	$U(\text{Å}^2)$
Na1	$2a$	0	0	0	0.001(6)
Na2	$2d$	0.5	0	0.5	0.009(7)
Na3	$4h$	0.5	0.340(2)	0.5	0.009(6)
Ir	$4g$	0.5	0.167(1)	0	0.001(1)
O1	$8j$	0.748(6)	0.178(2)	0.789(6)	0.001(6)
O2	$4i$	0.711(7)	0	0.204(7)	0.001(7)

Table 4.1: Structural parameters of Na_2IrO_3 determined via single-crystal x-ray diffraction at room temperature [114].

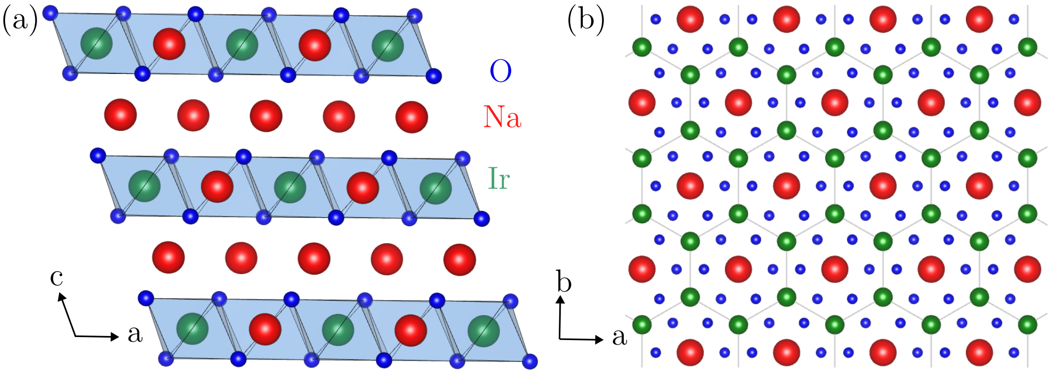

Figure 4.2: Crystal structure of Na_2IrO_3 perpendicular (a) to the alternating Na and $NaIr_2O_6$ layers as well as perpendicular to the *ab*-plane (b). The Ir atoms form a slightly distorted honeycomb structure and are each surrounded by oxygen octahedra with the empty places filled by Na atoms.

Laue back-scattering measurements

The Laue patterns shown in this section were recorded by B.Sc. Julian Kaiser [131]. All Laue measurements were performed in back-scattering geometry using a PW1830/40 X-ray generator by Philips with a tungsten anode and a detector by PHOTONIC SCIENCE. Voltages of 10, 15 or 20 kV and a current of 30 mA were applied for all measurements. A time of 10 min proved to be a sufficiently large exposure time for high-quality crystals with no significant improvements in pattern quality found for longer exposures. For good-quality single crystals, neither polishing nor cleaving lead to an improvement in the recorded patterns.

After subtracting the background, the recorded data was analysed using the software Single Crystal (Crystal Maker) as well as a program developed by B.Sc. J. Kaiser allowing the user to take both reflections due to additive overlap as well as reflections due to proximity to the characteristic wavelengths of tungsten into consideration.

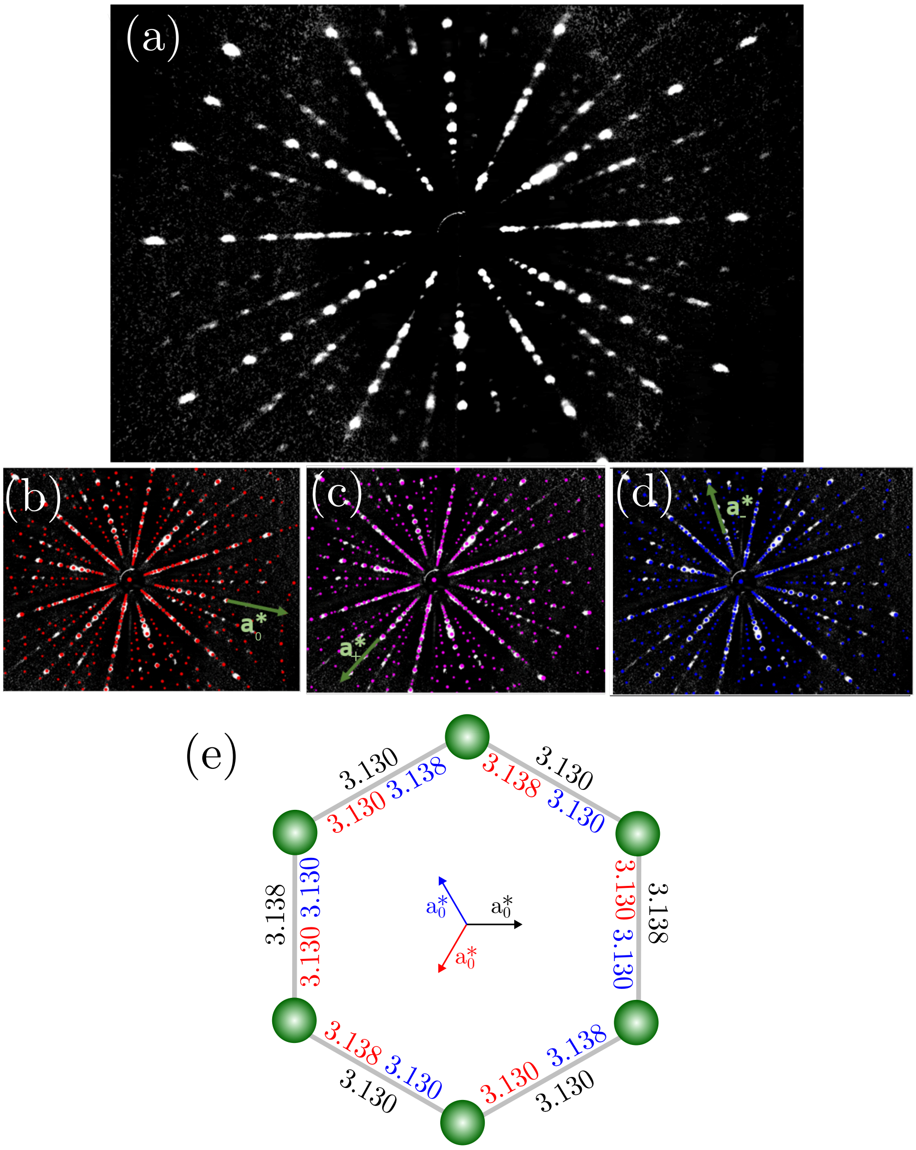

Figure 4.3: (a) Laue pattern of a high quality Na_2IrO_3 single crystal recorded at 20 kV. (b)-(d) show possible matches of simulated data, where the pattern is rotated around ±120° perpendicular to the c^*-axis. (e) The monoclinic distortion of the crystal structure leads to the divergence of the Ir-O-Ir bond angle from the ideal value of 90° and a slight distortion of the honeycombs. Rotation of ±120° thus does not lead to a perfect overlap of the structures which in turn results in a small shift of the Laue reflections.

A representative Laue pattern is displayed in Fig. 4.3(a) along with three possible sets of matching simulated data. Here, the data sets differ by a rotation of ±120° around the c*-axis, labelled a_0^* (0°), a_+^* (rotation of +120°) and a_-^* (rotation of -120°). At first glance, all three patterns appear to match the data reasonably well, as can be seen in Fig. 4.3(b)-(d). The iridium honeycomb for the three orientations along with the respective bond lengths is shown in Fig. 4.3(e). Due to the deviation of the Ir-O-Ir bond angle from the ideal value of 90°, the bonds do not show perfect overlap for the different orientations. Thus, a rotation of ±120° results in a shift in the reflections detected along (0 k l) due to the divergence of the honeycombs from the ideal structure stemming from the monoclinic distortion of the crystal structure, while those for (h 0 l) mostly overlap.

Taking a closer look at the reflections labelled 1-6 in Fig. 4.4(a), it becomes apparent that only 1-4 are covered correctly by the simulated data, while reflections 5 and 6 remain unexplained, as can be seen in Fig. 4.4(b). One possible explanation would be an underestimated detector sensitivity. Simulated data assuming higher sensitivity would give matching data points for all six reflections (see Fig. 4.4(c)), assigning reflection 5 and 6 the indices $\overline{6}\,\overline{2}\,\overline{13}$ and $\overline{6}\,2\,\overline{13}$. However, several additional reflections appear in the simulation which are not present in the recorded pattern. Furthermore, in a pattern recorded at 15 kV, shown in Fig. 4.4(d), both reflections 5 and 6 remain present, while they disappear in the simulation assuming higher detector sensitivity. Thus, an underestimated detector sensitivity is excluded as an explanation for the missing indication of some reflections. Fig. 4.4(e) shows the simulated pattern combining all three orientations a_0^*, a_+^* and a_-^* previously found to be reasonably good matches. A simultaneous occurrence of all three orientations indeed appears to provide a match for all investigated reflections, indexing reflections 5 and 6 as $2\,\overline{4}\,\overline{8}$ of a_+^* and $2\,4\,\overline{8}$ of a_-^* respectively.

A simultaneous presence of all three orientations would also present an explanation for the increased brightness of some reflections and the smearing found for others. For the former, this is the case if the reflections of two or more reflections overlap and their individual brightnesses add up. For the latter, due to the distorted honeycomb lattice, there is no perfect overlap for the individual reflections along the (0 k l) direction resulting in the observed broadening of the total reflections.

Taking another look at the reflections shown in Fig. 4.4(a), one can see, that for a voltage of 10 kV, reflections 2, 3, 5 and 6 disappear (Fig. 4.4(f)). Comparison to the characteristic lines of tungsten reveals the wavelength of these reflections to be close to the L_{β_1} and L_{β_2} lines which can be detected for voltages above 12.1 or 10.2 kV and thus not to be detectable at lower voltages. Reflections in the immediate vicinity of these lines are also likely to appear brighter, since the intensity of the characteristic lines far surpasses that of the bremsspectrum. Reflections further away from the characteristic lines may then just be hidden by the background noise.

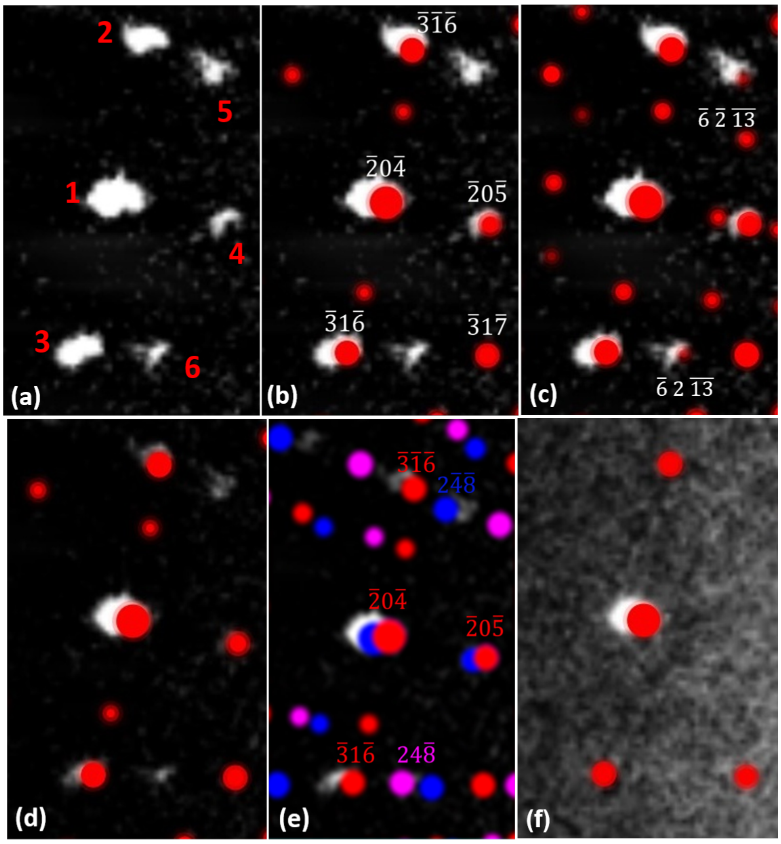

Figure 4.4: Taking a closer look at the reflections 1-6 (a), one finds that not all of them are matched by the simulated data (b). A higher detector sensitivity would provide a match for every reflection, but also yields several additional reflections not detected in the measurement (c). Recording a pattern at 15 kV (d) still shows reflections 5 and 6, while they disappear in the simulation even for higher detector sensitivity. A combination of all possible orientations a_0^*, a_+^* and a_-^* (e) gives the best fit, resulting in a match for each detected reflection. (f) For a voltage of 10 kV, reflections 2, 3, 5 and 6 disappear [132].

In order to be able to analyse the Laue patterns in view of the above mentioned points, a program was designed by J. Kaiser which allows the consideration of both additive overlap of individual reflections as well as characteristic lines. Only reflections with a wavelength deviation of less than 0.02 Å from the characteristic tungsten lines are included and the intensity of the reflections is assumed to be directly proportional to the covered area. Additionally, due to a small mismatch of the two detector halves, the analysis was done separately and then joined afterwards in order to obtain a full picture. The resulting Laue simulation is depicted in Fig. 4.5 showing a good match with the recorded pattern assigning an index to each reflection.

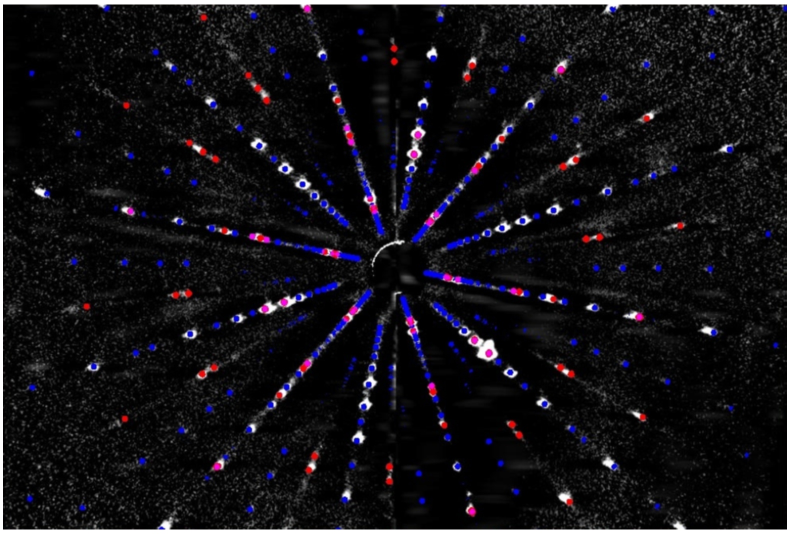

Figure 4.5: Laue pattern from Fig. 4.3(a) with a simulated pattern considering the simultaneous presence of all three orientations a_0^*, a_+^* and a_-^*. All reflections are matched by the simulated data [131, 132].

For small domains, a translation by $\pm\vec{b}/3$ would yield a similar result as a rotation of 120° posing an alternative explanation for the Laue pattern. Such a translation was found to be the case for Li_2IrO_3, which also belongs to the class of honeycomb iridate materials [114, 133]. However, in larger domains, both models no longer yield similar results. Thus, a simultaneous presence of three types of domains with rotation of 120° around c^* seems to be the best explanation for the Laue patterns recorded, not only indexing all peaks, but also explaining smearing of some as well as the increased brightness of other reflections.

Investigating Surface Structures using SEM and EDX

Investigations of the sample surface were performed using a SEM (Scanning Electron Microscope, type Merlin by Zeiss) along with a NTS-BS (Nano Technology Systems-Backscattered Electrons) detector which produces images with high sensitivity for material contrasts depicting areas with higher average atomic number with increased brightness. Bright lines with a thickness of up to 2 µm are found on the surfaces of cleaved and polished Na_2IrO_3 crystals as well as samples previously exposed to air. Most lines run parallel or intersect each other at an angle of 60 or 120°. Images recorded with other detectors such as AsB (angular selective backscattered electron) or HE-SE2 (high efficiency secondary electron) also revealed such lines, however, they are best visible in a backscattered electron image, some examples of which are shown in Fig. 4.6. Upon closer inspection, these lines are also visible when looking at the sample under an optical microscope at high magnification. After thorough investigation of the sample surfaces, topological features like steps, cracks or surface contaminations can be excluded as the origin of these bright lines.

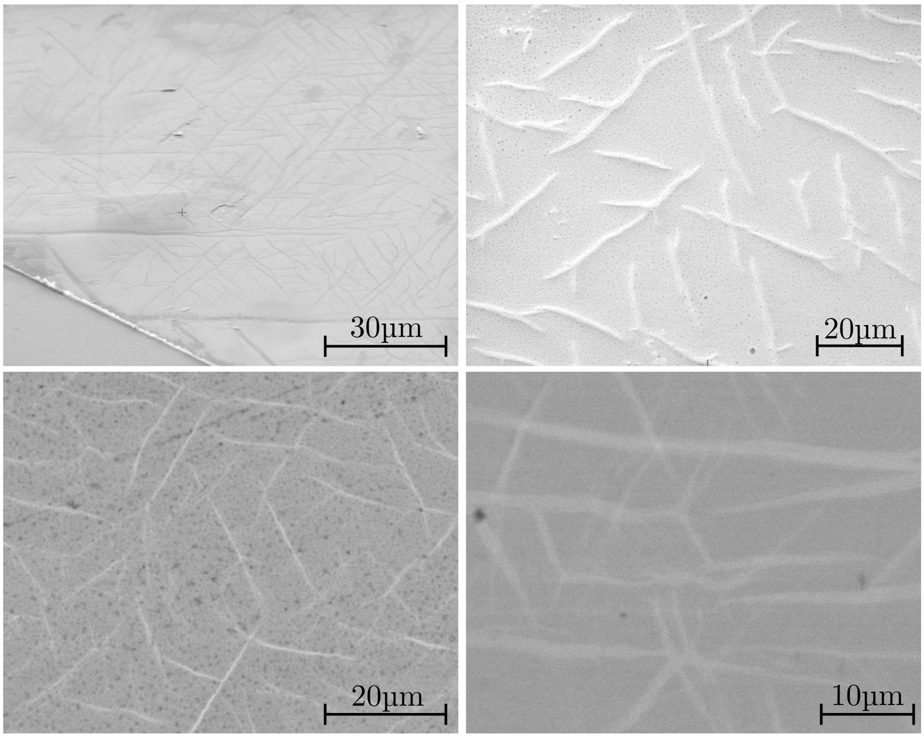

Figure 4.6: Taking a closer look at the surface of Na_2IrO_3 using a SEM along with a material contrast sensitive detector reveals bright lines with thicknesses of up to a few micrometers. Comparison with Laue data indicates that these lines are oriented along the three distinct b-axes.

For all samples on which both Laue and SEM measurements were performed, the direction of the lines was found to roughly correspond to at least one or more of the b axes of the three orientations a_0^*, a_+^* and a_-^*. This correspondence leads to the conclusion that the bright lines are domain walls separating domains which are rotated by ±120° relative to each other separating domains with different orientations.

A previous study on $(Na_{1-x}Li_x)_2IrO_3$ in the regime of $x > 0.25$ where phase separation occurs showed the appearance of similar lines [10]. However, in this case they can be assigned to a separation of pure Li_2IrO_3 regions from the doped areas, clearly differentiating these lines from those found in this thesis.

Elemental distribution maps of the Na content along the domain walls recorded via EDX reveal a decrease in the amount of Na on the lines compared to the surrounding areas, as depicted in Fig. 4.7. A linescan perpendicular to a domain wall clearly shows a drop in the sodium signal, while the counts for iridium remain more or less the same over the investigated region. The bright appearance of these domain walls in the SEM images recorded with the NTS-BS detector can thus be explained by the diminished Na content resulting in a higher average atomic number.

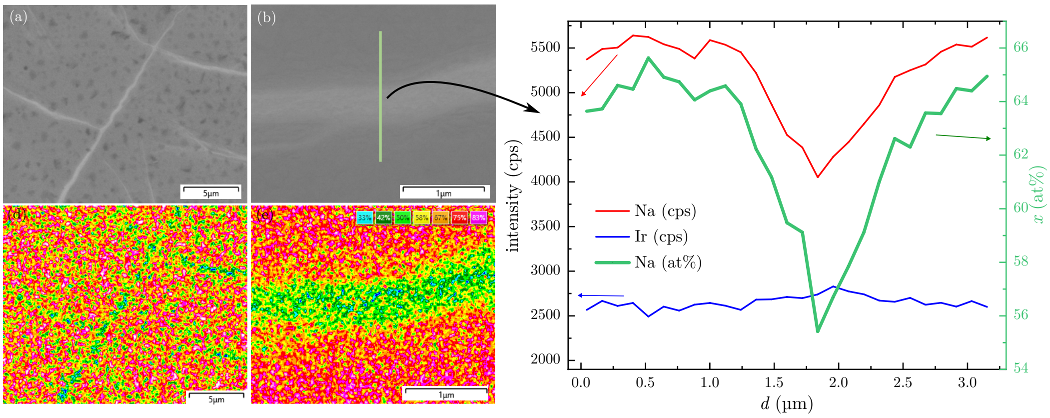

Figure 4.7: Elemental map recorded via EDX shows a Na deficiency of several atomic percent within the line compared to the surrounding surface where the green points indicate a lower Na content compared to the orange or pink surrounding area. The right graph depicts a line scan performed along the green line in (b), clearly showing the drop in Na content.

Looking at the Na:Ir ratio of several samples on and next to the domain walls listed in Tab. 4.2, the lines show a ratio in the range of 1.1-1.5 which equals a Na deficiency of up to $\sim 1/3$ for samples # 6 and # 7. It should be noted, that the Na:Ir ratio outside the lines is smaller than the theoretically expected value of 2. This could be attributed to re-adsorption of the heavy iridium atoms. The detected ratio thus is likely not an accurate representation of the atomic ratio, but can still be used to measure and compare the samples stoichiometries. A diminished Na content on the sample surface was already found in previous STM measurements by other groups showing up to 2/3 of Na atoms missing on the surface due to the weak bonding of the Na layer to the bulk [134]. While STM only looks at the surface, the penetration depth of EDX is in the range of several hundred nanometres meaning several crystal planes are included in the analysis [105].

Since the penetration depth is dependent on the applied voltage, all measurements were recorded at 20 kV allowing for comparability of the obtained values. Measurements at lower voltages showed a tendency towards slightly higher Na deficiency, hinting at an increase in Na content with increasing distance from the sample surface.

Unfortunately, it was not possible to definitely determine the depth of the domain walls. Attempts to investigate them via transmission electron microscopy (TEM) measurements did not yield usable results due to the high air sensitivity of Na_2IrO_3 surfaces and the corresponding degradation of the ultrathin lamella prepared for this purpose.

sample	$(Na/Ir)_{line}$	$(Na/Ir)_{surrounding}$
#1	1.5(2)	1.8(1)
#2	1.5(2)	1.8(1)
#3	1.3(1)	1.8(1)
#4	1.3(1)	1.7(1)
#5	1.2(2)	1.6(2)
#6	1.1(2)	1.6(2)
#7	1.1(1)	1.7(2)

Table 4.2: Atomic ratio of Na and Ir for different crystals determined via EDX on (line) and around (surrounding) the lines sorted from highest to lowest value.

4.3 Electrical Resistance

Samples for resistivity measurements were prepared via FIB-SEM microstructuring by either cutting lamellae or directly cutting the crystal, which was glued onto a sapphire substrate, into the desired geometry. A detailed explanation of this process can be found in 3.3.

Comparison with Measurements on Bulk Samples in Literature

Since no previous measurements on FIB structured Na_2IrO_3 devices exist at the time of this work, the first step taken to ensure data reliability was a comparison of the temperature dependent electrical transport with previous measurements performed on bulk samples. Na_2IrO_3 is known to show an increasing resistivity towards low temperatures making low temperature measurements difficult, as in some cases the maximum resistance of the measurement setup is reached and no further data can be recorded.

Measurements were performed on lamellae as well as samples for which a structure suitable for four wire measurements was cut directly into the bulk crystal.

While some FIB structured Na_2IrO_3 samples were found to show a current or frequency dependence, the origin of which will be discussed at a later point, the high temperature electrical transport is consistent with the known variable range hopping (VRH) behaviour found for bulk Na_2IrO_3. This VRH behaviour arises from the strong on site Coulomb interaction of the Ir 5d orbitals as well as the structural disorder due to interatomic site mixing as well as stacking faults [111, 114]. The occurrence of variable range hopping for this system is further backed up by the existence of narrow Ir 5d-t_{2g} bands as well as a small insulating gap [135].

Plotting the logarithmic resistivity $\ln(\rho)$ versus $T^{-1/4}$ yields a linear plot from which the hopping temperature T_0 can be determined. Fig. 4.8 shows the temperature dependent resistivity down to 2 K as well as U-I-characteristics in the temperature range of 2-300 K for a sample for which neither a strong current nor frequency dependence was observed. Here, $\rho(T)$ continuously increases towards low temperatures and the hopping temperature can be determined as $T_0^{1/4} = 22\,\mathrm{K}^{1/4}$. The U-I-characteristics show non-linear behaviour up to 80 K. Rewriting $I(U)$ as $\ln(I)$ vs. $E^{-1/4}$ and performing a linear fit yields a characteristic localization field of $E_0^{1/4} = 50\,(\mathrm{V/m})^{1/4}$ for 20 K.

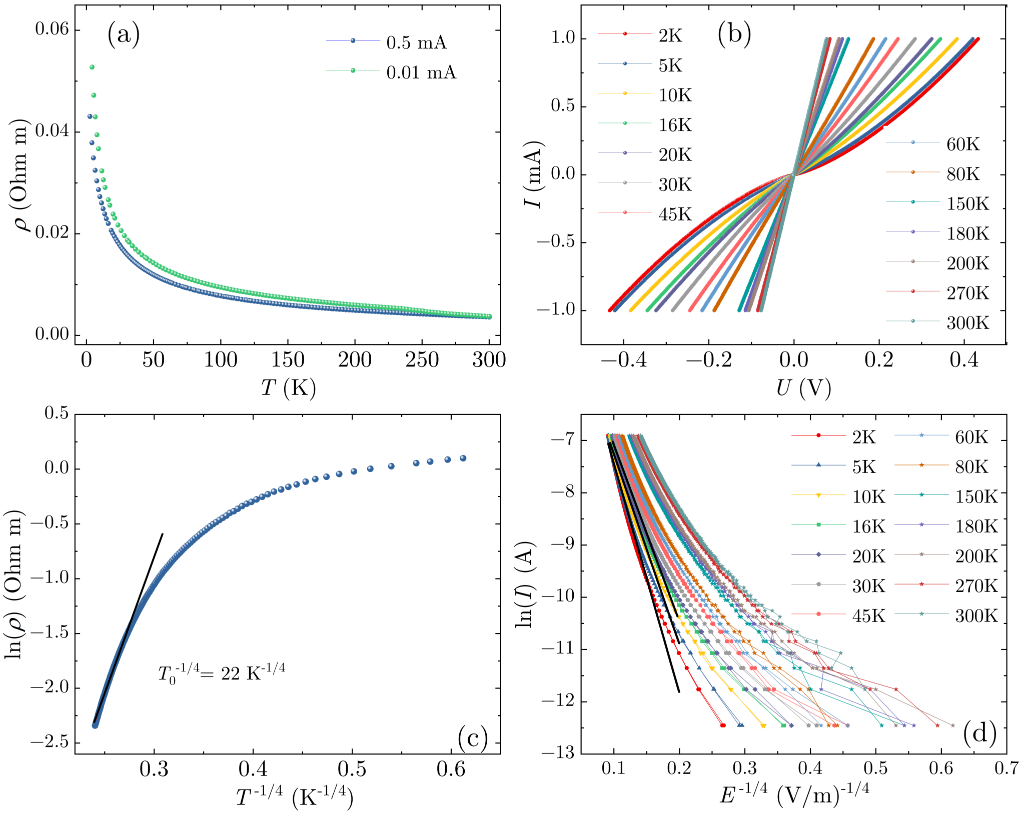

Figure 4.8: Temperature dependent resistivity (a) and U-I characteristic (b) for a FIB structured sample showing little to no current or frequency dependence. Plotting the data logarithmically as $\ln(\rho)$ vs $T^{-1/4}$ (c) or ln(I) vs $E^{-1/4}$ (d) reveals a regime with linear behaviour from which T_0 and E_0 can be obtained via linear fit (black).

Inserting both $E_0^{1/4}$ and $T_0^{1/4}$ into [136]

$$T_0 = \frac{21.2}{k_\mathrm{B} a_0^3 g_0} \tag{4.1}$$

$$E_0 = \frac{1}{e a_0^4 g_0} \tag{4.2}$$

and solving this system of equations for the localization length

$$a_0 = \frac{k_\mathrm{B} T_0}{21.2 e E_0} \tag{4.3}$$

and density of states

$$g_0 = \frac{T_0 k_\mathrm{B} a_0^3}{21.2} \tag{4.4}$$

results in the values listed in Tab. 4.3. These values are in between those obtained by Jenderka et al. for thin films [122] and Rodriguez et al. for a thin crystal device [123]. It should be noted, that Jenderka et al. determined T_0 from their own measurements, but estimated g_0 from previously published heat capacity data [137–141], while Rodriguez at al. measured both $\rho(T)$ and $I(U)$ in order to obtain the listed values.

sample	$T_0^{1/4}(\mathrm{K}^{1/4})$	a_0 (nm)	g_0 ($\mathrm{eV}^{-1}\mathrm{m}^{-3}$)
Jenderka et. al [122]	20-45	0.1-0.6	10^{28}
Na_2IrO_3 this work	22	2	10^{27}
Rodriguez et al. [123]	31	3	10^{25}

Table 4.3: Comparison of the hopping temperature T_0, localization length a_0 and density of states g_0 determined by $\rho(T)$ and $I(U)$ measurements for a FIB structured sample with literature data.

In conclusion, it can be said, that FIB structured samples show electrical behaviour comparable to measurements performed on bulk samples or thin films. However, some samples showed either a frequency or current dependence of the electrical resistivity. Thus, in order to ensure good quality data, for all further measurements only samples which did not show such dependences were used for analysis.

It should also be mentioned at this point that the absolute values of the electrical resistivity showed a tendency to increase for measurements performed at later times on the same sample. This offers a possible explanation for the difference in absolute values for different samples, since initially measurements were performed at different times depending on the availability of the necessary equipment. However, once this issue was discovered, measurements on all further samples discussed in the next section were performed immediately after FIB structuring and contacting was finished.

FIB structured Domain Walls

In order to further study the domain walls detected by SEM-EDX, electrical transport measurements were performed. For this purpose, several domain walls were contacted for four wire measurements by FIB microsectioning. Here, only one domain wall per crystal was contacted in order to avoid any interference between measurements on the same sample.

The Na deficiency of each sample was determined by EDX prior to microstructuring. Fig. 4.9(a)-(c) shows an example of such a sample. The domain wall (blue) is contacted by GIS-deposited platinum (red) which is connected to the gold coated (yellow) area. Trenches are cut to separate the gold surface into four separate contact pads and ensure the absence of any other conductive paths besides that along the domain wall. In order to avoid sample degradation as much as possible, the crystals were cleaved inside an argon filled glovebox, then transferred to the sputtering chamber in a sealed box and immediately transferred into the FIB-SEM chamber. During contacting, air contact could not be avoided completely due to the silver epoxy not fully drying inside a glovebox, but was limited as much as possible. As an increase in resistivity of samples with increasing time since contacting was observed for several devices, as soon as the contacts were cured, the sample was placed into the PPMS chamber in order to ensure comparable conditions for all measured samples. In this way, a total of four samples were measured successfully with the Na:Ir ratio ranging from 1.82 to 1.08 on the domain walls, the $R(T)$ plots of which are shown in Fig. 4.9(d).

Since the height of the domain walls remains unknown, the total sample thickness along with the line width and the distance of the voltage contacts was used in order to calculate the geometry factor. Thus, the absolute values are only an upper limit with the real resistivity of the domain walls possibly being even smaller. Compared to previous bulk measurements, the absolute values are already rather small even for the highest Na content and decrease even further with increasing Na deficiency. For the two samples with the lowest detected Na:Ir ratio of 1.12 and 1.08 respectively, metallic behaviour, meaning $\mathrm{d}\rho/\mathrm{d}T > 0$, is observed down to 2 K.

Fitting the low temperature resistivity for both samples with a sum of the residual resistance, electron-electron and electron-phonon contributions $\rho = \rho_0 + aT^2 + bT^5$ [142], as shown in Fig.4.9(e), parameters comparable to those of moderately heavy $4f$ and $5f$ Kondo systems as well as bilayer Sr_2RuO_4 along the a- and c-axis [143] are obtained. The exact values of the parameters for both metallic samples are listed in the caption of Fig. 4.9(b). As mentioned, this statement is made under the assumption of the domain wall thickness equalling the sample thickness, which is usually in the range of 20-40 µm.

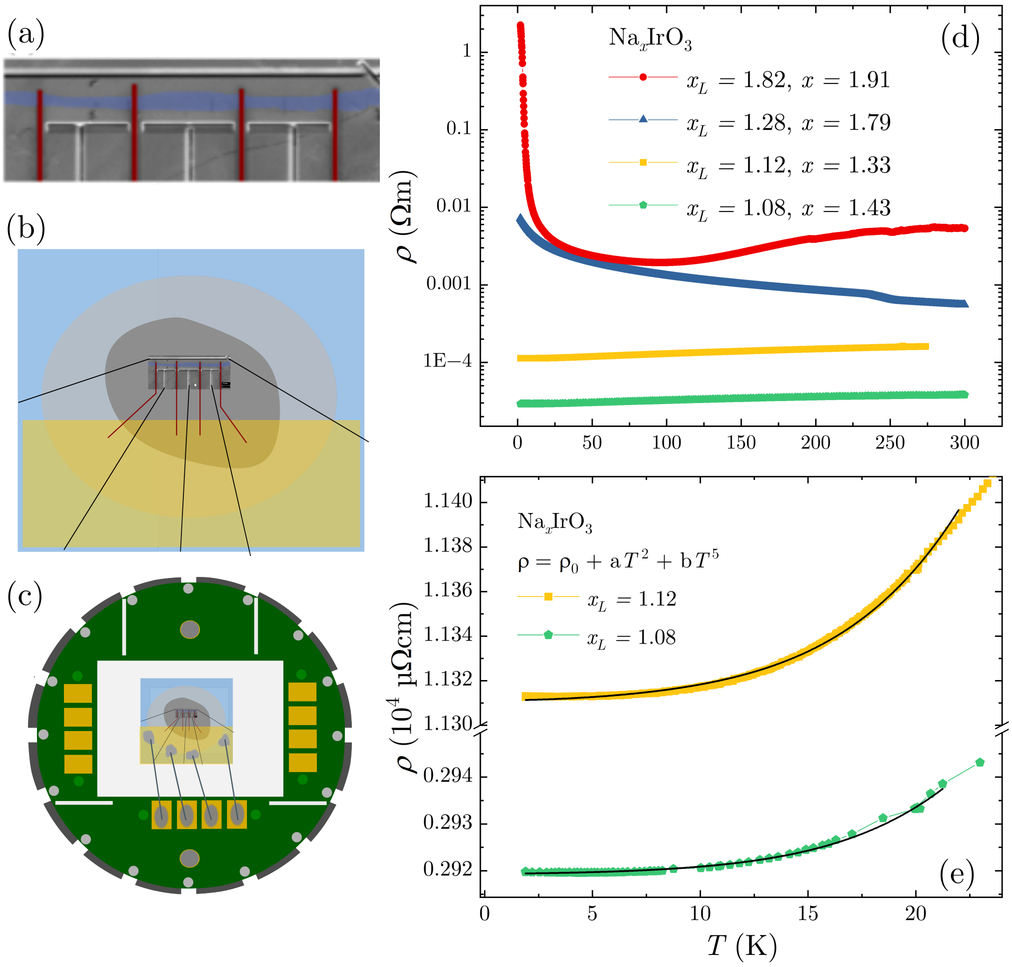

Figure 4.9: (a) Contacting of the domain wall (blue) with GIS deposited platinum (red). (b) Contacted crystal on sapphire substrate with gold contact pads. (c) Contacted sample on PPMS puck. (d) Temperature dependent resistivity on several domain walls with varying Na content. x_L denotes the Na/Ir ratio on the line, x that in the surrounding area as determined by EDX. With increasing Na deficiency, the absolute values become smaller. For the two samples with highest Na deficiency, metallic behaviour was found down to 2 K. (e) Fitting the low temperature data with $\rho = \rho_0 + aT^2 + bT^5$ yields values $\rho_0 = 1.13 \cdot 10^4\,\mu\Omega\text{cm}$, $a = 6.18 \cdot 10^{-2}\,\mu\Omega\text{cm K}^{-2}$ and $b = 1.11 \cdot 10^{-5}\,\mu\Omega\text{cmK}^{-5}$ for the yellow and $\rho_0 = 2.92 \cdot 10^3\,\mu\Omega\text{cm}$, $a = 0.96 \cdot 10^{-2}\,\mu\Omega\text{cmK}^{-2}$ and $b = 0.24 \cdot 10^{-5}\,\mu\Omega\text{cm K}^{-5}$ for the green plot.

The sample with the second lowest Na:Ir ratio was remeasured two more times, after two and five days of air exposure respectively, in order to check if the metallic conductivity is preserved over time. After two days, an increase in absolute values was observed, while the sample remained metallic in the whole investigated temperature range. After five days, however, not only did the absolute values increase even further, but now an increase of the resistivity towards low temperatures is observed. This appears to be due to degradation which is known to occur for Na_2IrO_3 crystal surfaces upon prolonged exposure to H_2O and CO_2 [130] and which can thus be excluded as a possible explanation for the initial metallic behaviour.

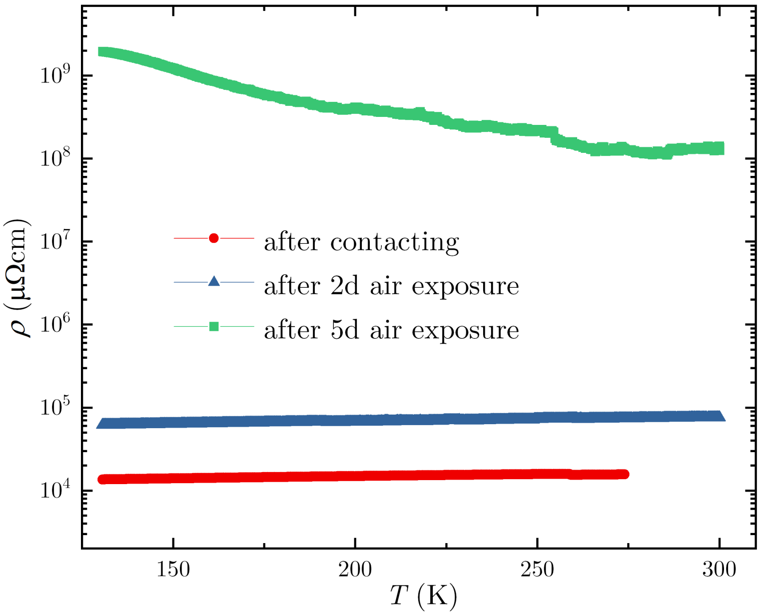

Figure 4.10: Temperature dependence of the resistivity of a metallic domain wall over time. After two days of air exposure, metallic behaviour can still be observed, though an increase in absolute values occurs. After five days, the resistivity shows even higher absolute values and increases towards low temperatures.

Thus, the metallic conductivity observed on Na deficient domain walls with a sufficiently high percentage of Na atoms missing indicates that the metal-to-insulator transition for Na_2IrO_3 has locally been passed due to hole doping as a result of the missing Na atoms, resulting in the observed electrical transport behaviour. A similar crossing of the metal-to-insulator transition was recently predicted in a theoretical study for ultrathin Na_2IrO_3 flakes with natural charge carrier doping of the 2D layers [144].

The observations of these structural domain walls running all over the crystal surface along with the variation of resistivity behaviour and absolute values depending on the Na deficiency may also offer an explanation for the differences observed in temperature dependent electrical transport as well as the non-linearity observed for low temperature U-I-characteristics measured on larger surface areas, which could both be attributed to the occurrence of a diverse array of conducting paths the orientation of which compared to the prepared four wire geometry may very well influence the resulting electrical transport.

Magnetoresistance

Both measurements of the longitudinal resistivity as well as Hall measurements were performed on domain walls showing metallic behaviour. Due to the limited stability of metallic behaviour, a new sample was prepared for this measurement. Metallic behaviour comparable to that previously observed was found in a quick $R(T)$ measurement. The longitudinal resistivity depicted in Fig. 4.11(a) shows a steep increase of the magnetoresistance at low fields indicating the presence of weak antilocalization and thus strong spin orbit coupling.

For higher fields, a H^2-behaviour can be observed. A similar behaviour was found in the out of plane magnetoresistance of heteroepitaxial Na_2IrO_3 thin films where it was attributed to a classical Lorentz contribution stemming from deflections of carriers in perpendicular fields [89, 122].

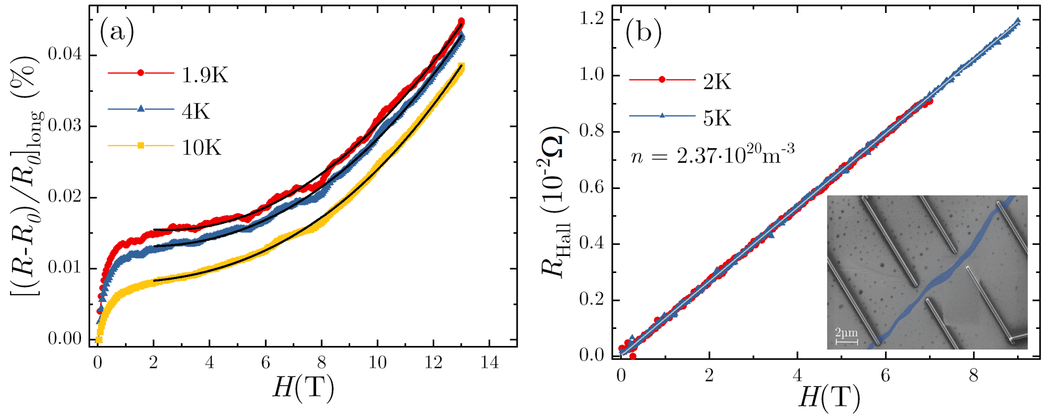

Figure 4.11: (a) Field-dependent magnetoresistance measured along a domain wall showing metallic conductivity. At low fields, a steep increase indicates the presence of weak antilocalization, while the high field regime can be fitted by a T^2-behaviour. (b) Hall resistance for a metallic domain wall showing linear behaviour. The inset shows the domain wall in blue along with the contacts made from GIS deposited platinum.

Another metallic domain wall was contacted as depicted in the inset of Fig. 4.11(b) for a Hall measurement. For this purpose, platinum contacts were made at two points on opposite sides of the domain wall allowing for both Hall measurements and a measurement of the temperature dependent longitudinal resistivity in order to once again ensure the occurrence of metallic conductivity. Due to the limited width of the domain walls, platinum was deposited at a very low rate with small FIB voltage and current in order to minimize platinum overspray and thus the deposition of platinum on the domain wall. EDX measurements confirmed the absence of platinum outside the contacts. The resulting measurement showed a linear Hall resistance. The charge carrier density was determined to be in the order of $10^{14}\,\mathrm{cm}^{-3}$ which is small compared to known metallic compounds for which the charge carrier density is usually of the order of 10^{22}-$10^{23}\,\mathrm{cm}^{-3}$ [145], but surprisingly large for a system which behaves like a Mott insulator in bulk.

No indications for the occurrence of an anomalous Hall effect or the formation of a hysteresis upon switching the field were found. Thus, while hole doping was reported to quickly lead to ferromagnetic ordering in Kitaev spin liquids [146, 147] and Roy and Kahir [144] even predicted ferromagnetic ordering for ultrathin Na_2IrO_3 flakes showing metallic behaviour due to natural doping, no indications for such ferromagnetic ordering could be found for the Na deficient domain walls investigated here.

4.4 Summary and Discussion

In summary, platelet shaped Na_2IrO_3 single crystals were grown from a combination of established solid state synthesis and calcination and analysed using a combination of Laue back-scattering and energy dispersive x-ray spectroscopy. Here the simultaneous occurrence of three different orientations a_0^* (0°), a_+^* (rotation of +120°) and a_-^* (rotation of -120°) differing by a rotation of ±120° around the c^* axis was found.

Combined SEM and EDX measurements uncovered the presence of bright, Na-deficient lines on the surfaces of pristine, freshly cleaved or polished single crystals which could be assigned to at least one of the three different orientations and were thus suggested to be structural domain walls.

In order to investigate the effect of Na deficiency on the electrical transport properties, such lines were contacted via FIB microstructuring after ensuring the reliability of this method by comparing measurements on larger FIB structured areas to previous bulk measurements. For these samples, variable range hopping behaviour occurs for higher temperatures. Resulting values of the hopping temperature T_0 are comparable to previous measurements on crystals or thin films. Non linear U-I-characteristics at low temperatures were found for several samples. Combining both measurements yielded information on the localization length as well as density of states both of which were in good agreement with data previously published.

Domain walls with different degrees of Na deficiency showed a correspondence between an increase in Na deficiency and a decrease in absolute values of the resistivity. The samples with highest Na deficiency (Na:Ir ratio of 1.1) even showed metallic behaviour down to the lowest temperature of 2 K. The coefficient observed for a T^2-fit indicates a moderately correlated state. Thus, hole doping appears to lead to a reduction of U/t and a local crossing of the metal-to-insulator transition due to hole doping. It should however be mentioned that, due to the unknown height of the domain walls, the resistivity values are just an upper limit and real values might be even smaller.

Repeat measurements at later times showed that the metallic state was not preserved over time with absolute values continuously increasing, until finally no more metallic behaviour was observed. This was assigned to be due to sample degradation, which then in turn could be excluded as an explanation for the initially observed metallic behaviour.

A similar metallic behaviour can be found in conductive domain walls occurring in otherwise insulating materials like ferroelectrics [148–150]. In these cases, conductivity is tuned by the application of an electric field resulting in non-linear U-I-characteristics similar to those observed for Na_2IrO_3 [123,126]. However, ARPES measurements showed that in the case of Na_2IrO_3 the charge carrier density – and therefore the Fermi level - is influenced by the deposition of additional Na atoms [123–125]. The conducting behaviour observed for structural domain walls of Na_2IrO_3 can thus be attributed to the Na deficiency.

The longitudinal magnetoresistance measured along such a metallic domain wall shows a strong increase at small fields indicating weak antilocalization and thus strong spin orbit coupling, while for higher fields a classical H^2-behaviour was observed. Furthermore, Hall measurements showed a linear resistance with no indication for an anomalous contribution and thus no ferromagnetic ordering.

5 Thermal Decomposition of α-RuCl$_3$ and its influence on the low temperature properties

Like Na$_2$IrO$_3$, α-RuCl$_3$ is a layered $j_{\mathrm{eff}} = 1/2$ spin-orbit Mott insulator [151–154] with significant spin orbit coupling in the order of 0.10-0.15 eV [155]. Even though α-RuCl$_3$ becomes a zigzag antiferromagnet below T_{N}=7-8 K [156–158], this order can be suppressed by applying a magnetic field in the order of 7 T. At room temperature, the crystal structure of α-RuCl$_3$ is monoclinic [158, 159], as can be seen in Fig. 5.1. At around 150 K a structural transition occurs [160, 161] with the correct low temperature structure still a topic of debate. For magnetic fields applied in-plane, measurements of the angle-dependent heat capacity show a close to six-fold symmetry stemming from the Ru^{3+} ions forming an almost perfect honeycomb structure [162].

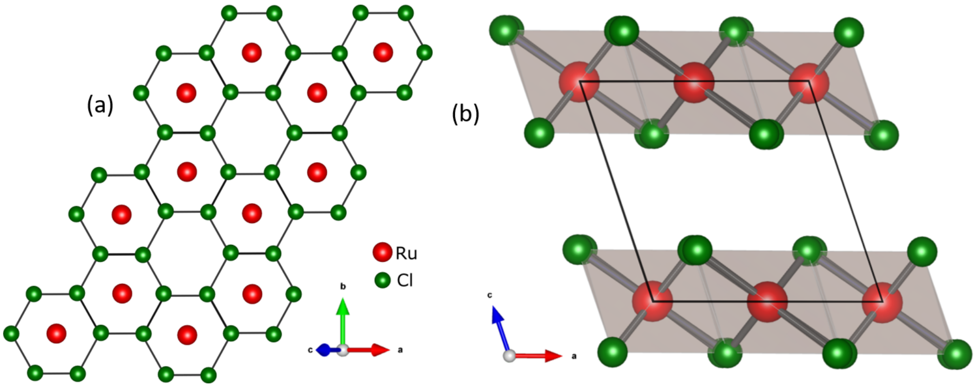

Figure 5.1: Monoclinic crystal structure of α-RuCl$_3$ depicted perpendicular to the *ab*-plane showing the honeycomb structure (a) and along the *b*-axis (b) (adapted from [159]).

While high interest in the physical properties of α-RuCl$_3$ has already been shown for years due to the its proximity to a Kitaev spin liquid [152, 153], this was further boosted by the detection of a half-integer quantized plateau in the thermal Hall conductance reported by Kasahara et al. in 2018 [2]. However, studies based on this initial report showed a strong sample dependence raising the question of the legitimacy of the claim of a generic regime of half quantization [163–169].

Some crystals were observed to show an additional feature in the specific heat capacity at around 14 K which is generally attributed to stacking disorder in the structural domains [158, 159, 161]. Thus, an absence of this 14 K signature along with a sharp heat capacity peak at 7-8 K is often used to classify single crystals as being of high-quality [158]. Since the honeycomb layers are only weakly coupled by van der Waals forces, strain effects or careless handling can easily lead to the introduction of stacking faults in α-RuCl$_3$ single crystals.

A 1968 study by Newkirk and McKee [170] looked at the chemical stability of RuCl$_3$ powder under ambient conditions at increasing temperatures and found significant decomposition of the material setting in at around 150°C.

At the time of the execution of this thesis, no detailed study on the chemical stability of α-RuCl$_3$ single crystals upon heating under different conditions and the possible influence on its (low temperature) properties has been conducted. Thus, the following chapter shows the results of systematically performed heat treatments of pristine α-RuCl$_3$ crystals on the sample stoichiometry determined by EDX and XRD as well as the low temperature heat capacity, magnetic susceptibility and resistivity. Furthermore, this chapter looks into the question of whether degradation or decomposition on a small scale already occurs during the crystal growth process.

5.1 Crystal Growth and Sample Preparation

Crystal growth of all RuCl$_3$ crystals investigated in this thesis was performed by Dr. Vladimir Tsurkan (EPV, Universität Augsburg). As starting material, anhydrous RuCl$_3$ powder (Carl Roth, 99.9% metals basis) was used. The powder was pressed into pellets, then transferred into a quartz ampoule inside an Argon filled glove box (O_2 and H_2O content <0.5 ppm). The closed ampoule was then connected to a turbo molecular pump and evacuated as low as 10^{-4} mbar. Upon heating the pressure increased indicating contamination in the starting material. Thus, the material was heated to 120° and held at this temperature while consistently pumped for at least 24 h. Once the starting materials were sufficiently clean, crystal growth was performed via vacuum sublimation [171] the concept of which is depicted in Fig. 5.2.

To this extent, the ampoule was once more evacuated down to 10^{-4} mbar, then sealed and horizontally placed into a muffle furnace and thus creating a heat gradient from the starting material to the furnace door. This method leads to reduced convection which is linked to the occurrence of stacking faults in the crystal which should be avoided. The typical temperature gradient is in the range of 5-10°C. A maximum temperature of 1000°C was held for

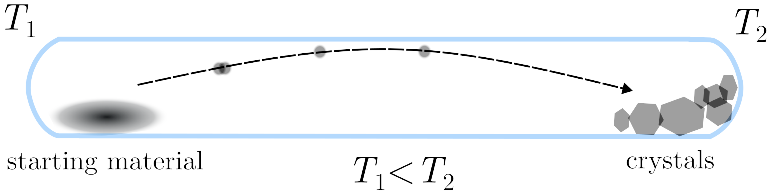

Figure 5.2: Vacuum sublimation is a crystal growth method where the starting material, in this case commercially available anhydrous $RuCl_3$ powder, acts as its own transport agent. Transport from the hot side (T_1) to the colder side (T_2) results in crystallization.

10 h, before slowly cooling down to 600°C over the course of 400 h (≙1 °C/h). Faceted crystals of several millimetres size with shiny surfaces can be obtained this way, as can be seen in Fig. 5.3(c). The crystal depicted in Fig. 5.3(a) shows some sample imperfections arising from cleaving, while the crystal in (b) is shown after heat treatment which leads to a much rougher surface.

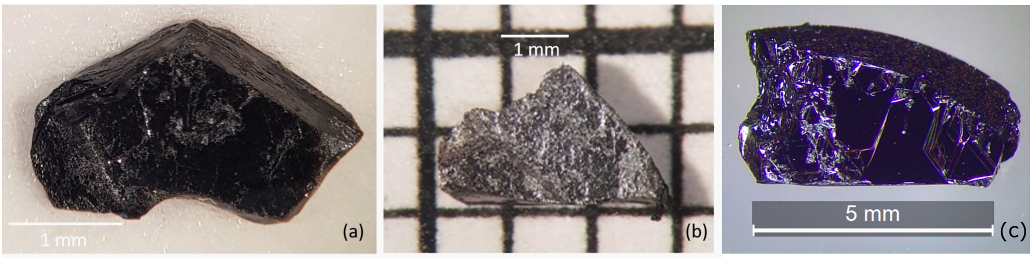

Figure 5.3: Crystals used for heat capacity study. Sample 1 (a) is depicted before heat treatments, sample 2 (b) after heat treatment in Argon flow at 500°C showing a much rougher surface. Imperfect cleaving can lead to imperfections on the surface, as is the case here. For comparison, (c) (image credit: Vladimir Tsurkan) shows a freshly retrieved as grown crystal with shiny surfaces.

Crystal quality can be checked by looking at the samples heat capacity. While crystals of good quality usually show only a single sharp transition at around 7 K, a (second) signature at 14 K is a sign of lower quality and often linked to the occurrence of stacking faults [168]. As can be seen in Fig. 5.4, all samples shown in the following chapter showed consistent molar heat capacity data with only a single transition at 7 K. Between measurements and/or heat treatments, samples were cleaned with n-butyl acetate to avoid carrying any grease, silver epoxy or glue residue into the next measurement. Heat capacity measurements of untreated samples before and after EDX analysis were performed in order to check for changes induced by the measurement. The low temperature heat capacity remains unchanged, as shown exemplary for sample 1 in Fig. 5.4. All untreated samples show consistent heat capacity down to 0.35 K.

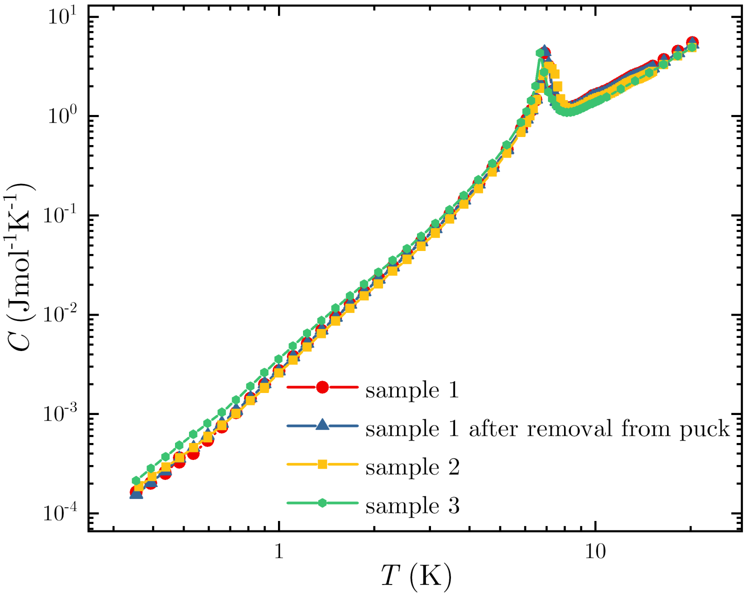

Figure 5.4: The specific heat capacities of the untreated samples 1,2 and 3 show consistent behaviour down to the lowest measured temperatures. For sample 1, the heat capacity after removal from an EDX puck was measured in order to determine if this influences the sample behaviour. No change in heat capacity before and after the measurement was found.

Heat treatments of the samples were performed in two different ways. Sample 1 and 3 were each sealed in a quartz ampoule flooded with 150 mbar Argon after cleaning the ampoule with acetone, drying it at 70°C and evacuating down to 10^{-2} mbar and flushing with Argon several times. The sealed ampoules were then heated in increasing steps of maximum temperature which was held for 12 h, until a decrease in mass was detected (scale accuracy 0.01 mg). No experiments with longer holding times were performed, as the exponential influence of the maximum temperature surpasses the linear one of increased holding times. For sample 1, the first detectable change in mass was found after heating at 400°C. For sample 3 the mass of which was roughly three times that of sample 1, a change was observed already after 350°C. Heat treatments of samples 2 and 4-6 were performed inside a differential thermal analysis (DTA) chamber, where Argon flow could be realized. Here, the crystals were individually placed into small Al$_2$O$_3$ crucibles typically used for DTA. The sample chamber was evacuated down to 3 mbar, then flushed with Argon for a few minutes before heating to 500°C for 1 h. After heat treatment, clear mass loss can be detected. The samples also showed a pronounced change in appearance with the surfaces now being significantly less shiny and more porous. Thus, the crystals had to be treated with great care in order to avoid flakes breaking of. The mass of all crystals before and after heat treatments was determined by weighing them several times and averaging those values, a summary of which can be found in Tab. 5.1. Since sample 6 was used only for an electrical transport study, the mass was not recorded.

	m_{sample} (mg)	Δm(%)
sample 1	6.34(2)	-
400°C	5.96(3)	6%
450°C	5.84(4)	8%
sample 2	5.44(2)	-
500°C	4.58(3)	7%
sample 3	20.05(7)	-
350°C	18.89(5)	6%
sample 4	12.79(5)	-
500°C	11.76(5)	8%
sample 5	14.73(3)	-
500°C	11.35(4)	23%

Table 5.1: Masses of the pristine and heat treated samples 1-5 along with the difference in sample mass before and after heating determined by balance.

5.2 Chemical Analysis

The sample stoichiometry for all depicted samples at each step was determined by EDX. All elements other than Ru and Cl where deconvoluted for the following data sets. Thus, Ru and Cl content always add up to 100 at%. It should be noted, that, while oxygen (as well as carbon) is always detected during EDX due to previous air exposure of the sample, reliable quantization of the oxygen content of the sample was not possible in this experiment. Untreated samples show a Ru:Cl ratio of 25(3):75(3) and an even distribution of both elements over the investigated surfaces, as shown in Fig. 5.5, whereas heat treated samples show significant changes in both aspects. It should be noted here, that due to limitations in the size of area that can be investigated during each measurement as well as time constraints, an examination covering the complete sample surface in detail was not feasible.

As can be seen in Fig. 5.6(a)-(c), a formation of clusters consisting mainly of Ru (up to 75 at%) was found on the surface of sample 1 after heat treatment at 400°C, the diameter of which was in the range of up to 70 µm. The average atomic ratio of Ru:Cl over the investigated surface was 30:70 and 32:68 after heat treatments at 400 and 450°C respectively.

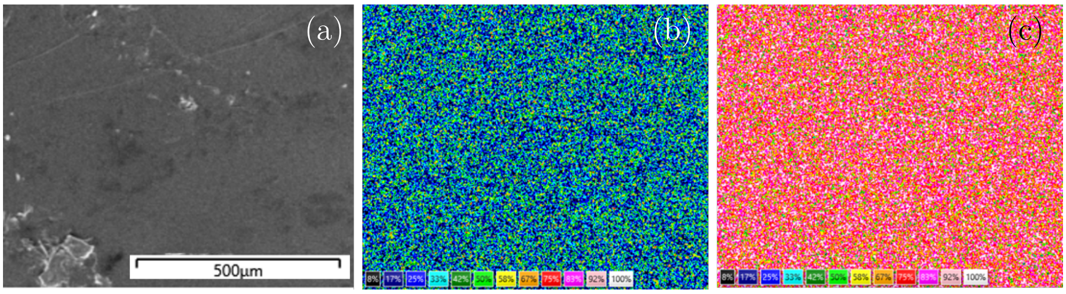

Figure 5.5: SEM image (a) and elemental distribution maps of the surface ((b) and (c)) of the untreated sample 1. The distribution of Ru (b) and Cl (c) appears rather homogeneous with the overall stoichiometry being 25(3):75(3) which is as expected. The color code in (b) and (c) describes the percentage of Ru or Cl atoms with both values adding up to 100% ranging from 0 (black) to 100 (white).

Heat treatments at increased temperatures thus seem to lead to an additional change in sample stoichiometry. While the SEM image of sample 2 (not depicted) did not show any visible formations such as the clusters found for sample 1, the overall stoichiometry was found to be 62:38 which equals a drastic reduction of the Cl content of the sample surface (analogous for sample 4 depicted in Fig. 5.6(d)).

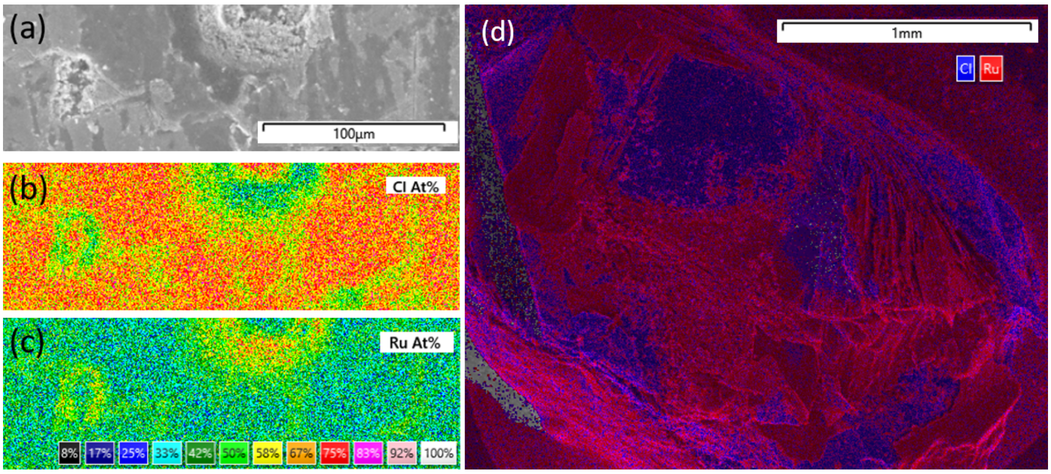

Figure 5.6: SEM image (a) and elemental distribution maps of samples 1 ((b) and (c)) and 4 (d) after heat treatment at 400 or 500°C respectively. While sample 1 shows a formation of clusters with increased Ru concentration along with a decreased amount of Cl and a diameter of up to 70 µm, sample 3 shows an overall increased Ru concentration with large areas of the surface showing almost no Cl. The color code in (b)-(d) describes the percentage of Ru or Cl atoms with both values adding up to 100% ranging from 0 (black) to 100 (white).

It should be noted that EDX is limited to the sample surface with the penetration depth of the electron beam being no more than 1 µm [105]. Thus, another crystals with a thickness of 0.5 mm was prepared analogous to sample 2 and cleaved into several layers, the last of which exposed the surface of the crystal roughly halfway in. EDX was performed on the freshly uncovered surfaces. The resulting maps can be seen in Fig. 5.7. As for sample 2, large areas with increased Ru content and Cl deficiency were found. The effect seems to weaken towards the crystal center. A few layers into the crystal the Ru:Cl ratio has changed to 44:56, which still equals a significant Ru excess, whereas in the center it is close to the pristine crystals stoichiometry again with only a small deviation and a Ru content of 27 at%. Nevertheless, it is clear from these measurements that the degradation of α-RuCl$_3$ due to heat treatment is not limited to the surface, but penetrates a significant distance into the crystal.

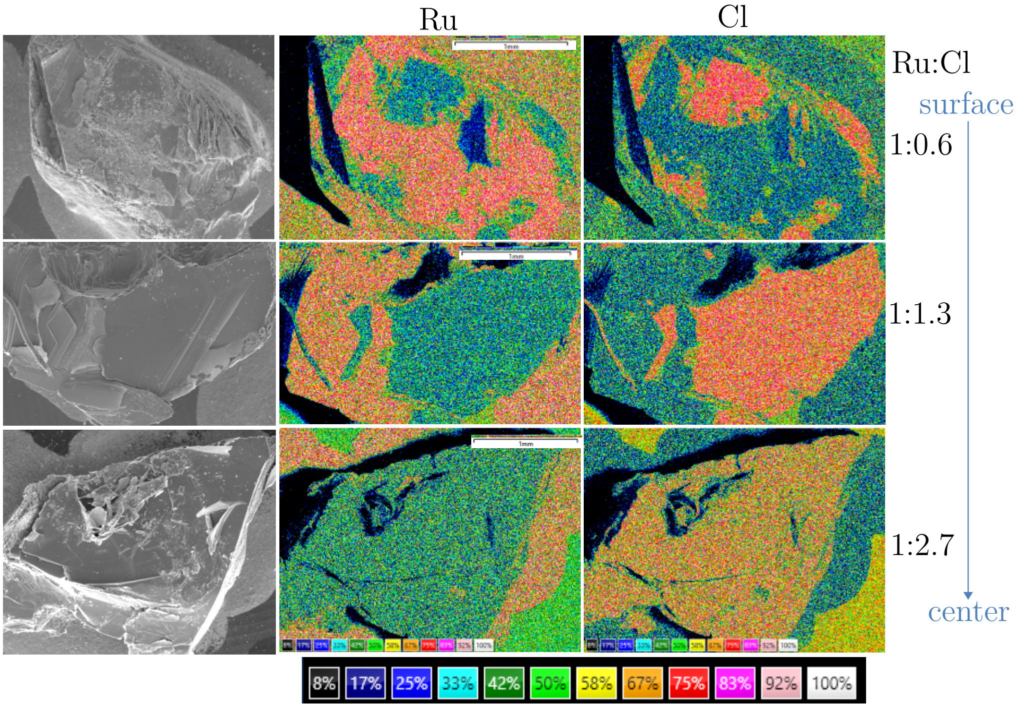

Figure 5.7: Elemental distribution for several layers of the annealed crystal (sample 4). Towards the center of the crystal, the Cl concentration increases with the ratio of Ru:Cl ranging from 1:0.6 on the surface to 1:2.7 halfway into the crystal which is still somewhat diminished compared to the pristine crystals stoichiometry. The effect of thermal annealing is thus clearly not limited to the sample surface. The color code of the maps describes the percentage of Ru or Cl atoms with both values adding up to 100% ranging from 0 (black) to 100 (white).

Looking at the increased ruthenium concentration determined by EDX, the question arises whether this is pure or metallic Ruthenium or some other compound containing elements which were deconvoluted or not detected during EDX analysis. As some elements, such as oxygen, are hard to be accurately detected and quantified via EDX an alternative method of characterization is applied. Thus, some of the porous surface material is carefully scrapped of the heat treated crystal (sample 4), ground into fine powder and x-ray powder diffraction is performed. The obtained diffraction pattern can be seen in Figure 5.8. Several sharp peaks are found, all of which match RuO_2 while no pure Ruthenium was detected. Ruthenium oxide is known to be a metallic transition-metal oxide [172].

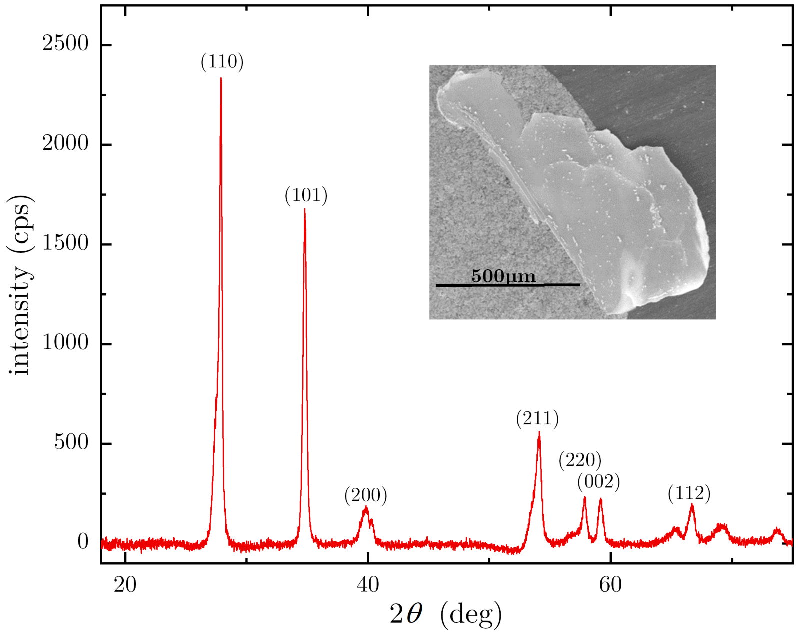

Figure 5.8: X-ray diffraction pattern of a flake removed from the surface of sample 4 after annealing. All peaks match those of RuO_2 with no indication of pure Ruthenium found.

5.3 Impact of thermal annealing

The following section will cover the impact of thermal annealing in argon or air respectively on the low-temperature heat capacity, magnetic susceptibility and electrical resistance.

Heat Capacity

Measurements of the heat capacity of the annealed samples in the temperature range of 0.35-20 K were performed using a Physical Properties Measurement System (PPMS) by Quantum Design. Measurements below 2 K were made possible by utilizing a He-3 option. For sample 1, heat treatments were performed with increasingly high maximum temperature, until a change in sample stoichiometry could be detected in EDX analysis which occurred at 400°C. As can be seen in Fig. 5.9, for sample 1 the heat treatment at 400°C leads to an increasing heat capacity towards low temperatures below 1.5 K. A second heat treatment at 450°C resulted in a further increase of the low temperature heat capacity. Furthermore, the magnitude of the peak at 7 K was found to decrease with increasing heat treatment temperature. Sample 2 shows a similar increase in the low temperature regime and a reduction in peak height. While the untreated samples show a T^3-behaviour down to lowest measured temperatures, the low temperature divergence shows a linear progression.

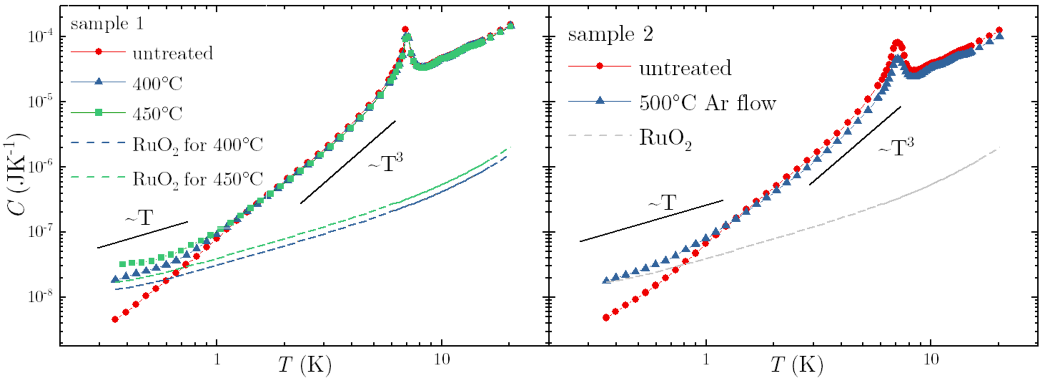

Figure 5.9: After heat treatments above 400°C the heat capacity of both sample 1 and 2 increases towards low temperatures for T<1.5 K. For sample 1, this effect is further enhanced by a second annealing at higher temperatures. The heat capacity of the RuO_2 fraction necessary to explain the deviation of the annealed samples is shown in dotted lines for all measurements [173].

Motivated by another paper [170] which reported degradation of $RuCl_3$ powder in air at temperatures as low as 150°C, another round of heat treatments were performed on a third sample, shown in Fig. 5.10, and this time heat capacity measurements were used instead of EDX as an indicator for changed behaviour. Here, a change in heat capacity can indeed already be found at 350°C, whereas heat treatment at 300°C does not appear to have any detectable impact on the heat capacity. While this is still significantly higher compared to the referenced paper [170], it should be noted that there are significant differences in both approaches. While our crystals are sealed under argon and thus have a very limited oxygen supply, the origin of which is not even clear yet, the powder was oxidized in air. Furthermore, the surface area directly exposed to the atmosphere is far higher for powder samples compared to a crystal. While small amounts of $RuCl_3$ might oxidise for the crystal at lower temperature, the overall fraction might just be too small for it to be detect by any of the available methods here.

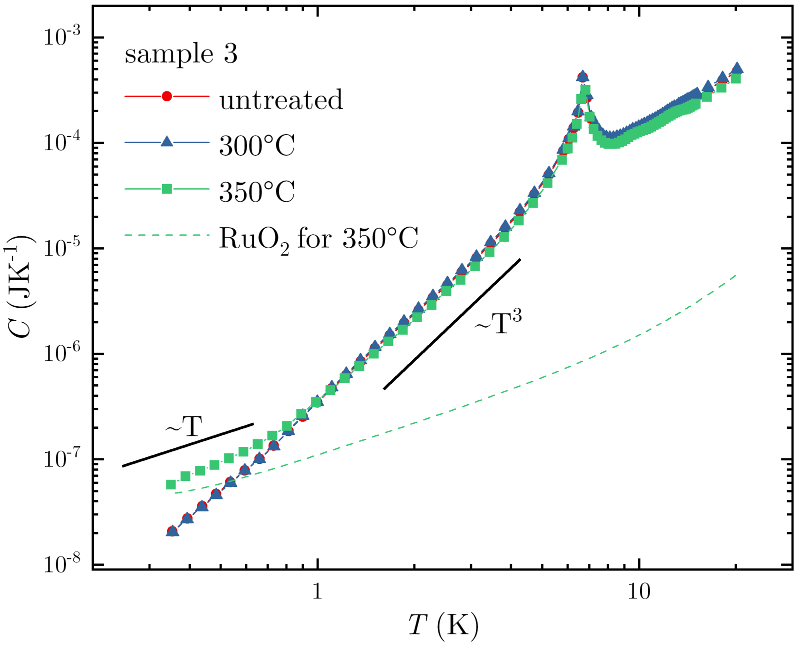

Figure 5.10: Heat capacity of another crystal (sample 3). While annealing at 300°C does not seem to have any visible effect, the low temperature heat capacity is increased after heat treatment at 350°C.

Looking at the heat capacity peak at T_N=7 K depicted in Fig. 5.11, a decrease in amplitude can be observed for the heat treated samples, while the peak position itself appears to be unchanged. Since the detected peak height depends on the exact temperatures at which data points were recorded, great care was taken to ensure that all plots were recorded with the same measurement sequence.

Before taking another look at the low temperature heat capacity of the annealed $RuCl_3$ crystals, the low temperature heat capacity of RuO_2 was measured using commercial powder (Sigma Aldrich, 99.9 % trace metals basis) which was pressed into a pellet. Comparison with previous measurements by other groups show that the heat capacity of RuO_2 in the investigated temperature range can be described very well by a $C = \alpha T^{-2} + \beta T^3 + \gamma T$ behaviour. The parameters obtained from this fit are $\alpha = 5.9 \cdot 10^{-5}$ JK/mol,

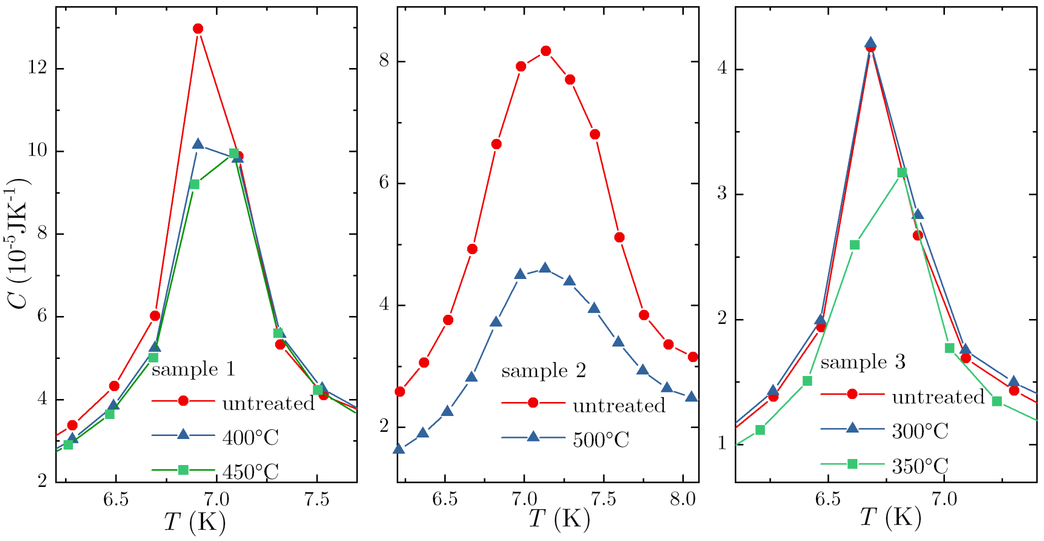

Figure 5.11: Temperature dependence of the heat capacity in the vicinity of the peak at $T_\mathrm{N} = 7\,\mathrm{K}$. The peak magnitude decreases with increasing heat treatment temperature.

$\beta = 2.25 \cdot 10^{-5}\,\mathrm{J/molK^4}$ and $\gamma = 5.77 \cdot 10^{-3}\,\mathrm{J/molK^2}$ which is similar to the values found in previous measurements done by Passenheim et al. [174] as can be seen in Fig. 5.12(a) where both our data as well as literature data are plotted.

Comparing the heat capacity of $\mathrm{RuO_2}$ and $\mathrm{RuCl_3}$ depicted in Fig. 5.12(b), one can see that the metallic contribution of the molar heat capacity of $\mathrm{RuO_2}$ surpasses that of $\mathrm{RuCl_3}$ for temperatures below 1.5 K which coincides with the temperature range where a deviation in the heat capacity of heat treated crystals can be observed.

Taking into consideration the data obtained for pure $\mathrm{RuO_2}$, an attempt was made to fit the heat capacity of samples 1, 2 and 3 with a combination of heat capacities of $\mathrm{RuCl_3}$ and $\mathrm{RuO_2}$ in units of J/K as shown in Fig. 5.13 with the following fit function

$$C/T = (m - m_{\mathrm{RuO_2}}) \cdot (\beta_{\mathrm{RuCl_3}} T^2) + m_{\mathrm{RuO_2}} \cdot C_{\mathrm{m,RuO_2}}/T \qquad (5.1)$$

Here, $C_{\mathrm{m,RuO_2}}$ is described by the fit done previously on the $\mathrm{RuO_2}$ pellet with the fit parameters now being $\alpha = 4.43 \cdot 10^{-7}\,\mathrm{JK/g}$, $\beta = 1.6 \cdot 10^{-7}\,\mathrm{J/gK^4}$ and $\gamma = 4.34 \cdot 10^{-5}\,\mathrm{J/gK}$. $\beta_{\mathrm{RuCl_3}}$ was set as a fit parameter for the untreated samples and then fixed for all later measurements. m is the sample mass determined by weighing the sample before or after heat treatment several times, then averaging the obtained values respectively. The mass of $\mathrm{RuCl_3}$ is expressed as the difference of sample mass and mass of $\mathrm{RuO_2}$ which leaves $m_{\mathrm{RuO_2}}$ as the only free fit parameter.

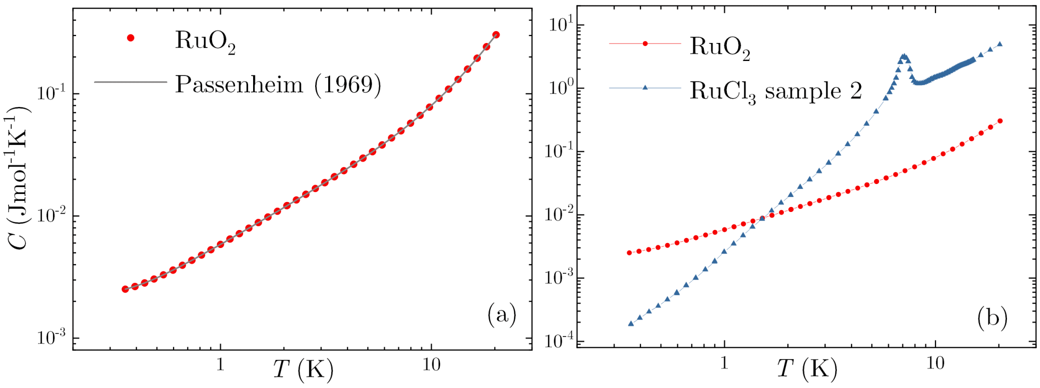

Figure 5.12: (a) Heat capacity of RuO_2 measured on a pellet in the temperature range of 0.35-20 K. The black line shows a fit $C = \alpha T^{-2} + \beta T^3 + \gamma T$. The parameters match those determined by Passenheim at al. (grey line) [174]. (b) Comparison of the heat capacity of RuO_2 and $RuCl_3$. For high temperatures the heat capacity of $RuCl_3$ surpasses that of RuO_2, whereas the RuO_2 heat capacity dominates for temperatures below 1.5 K.

For comparison, the mass fraction of RuO_2 in the heat treated samples was also determined in another way. Here we looked at the mass difference of the pristine and heat treated sample and calculated the mass of RuO_2 assuming that all mass loss can be attributed to the reaction $2RuCl_3 + 2O_2 \rightarrow 2RuO_2 + 3Cl_2$ resulting in the following formula:

$$m_{\mathrm{RuO_2,scale}} = \Delta m \left(1 - \frac{M_{\mathrm{mol,RuCl_3}}}{M_{\mathrm{mol,RuO_2}}}\right)^{-1} \tag{5.2}$$

A comparison of all obtained values can be found in Tab. 5.2. The masses obtained in both ways are very similar for all investigated samples with some samples consisting of as much as 18.6 mass% RuO_2.

	m_{sample} (mg)	$m_{\mathrm{RuO_2,balance}}$ (mg)	$m_{\mathrm{RuO_2,HC}}$ (mg)	$\frac{m_{\mathrm{RuO_2,HC}}}{m_{\mathrm{sample}}}$ (%)
sample 1	6.34(2)	-	0.06(1)	0.9(2)
400°C	5.96(3)	0.68(12)	0.61(2)	10.2(4)
450°C	5.84(4)	0.89(14)	0.93(4)	15.9(8)
sample 2	5.44(2)	-	0.09(2)	1.6(2)
500°C	4.58(3)	0.89(10)	0.85(3)	18.6(7)
sample 3	20.05(7)	-	0.41(9)	2.0(4)
350°C	18.89(5)	2.07(10)	2.62(7)	13.2(9)

Table 5.2: Masses of the pristine and heat treated samples 1-3 along with the RuO_2 masses and fractions calculated from the difference in sample masses determined by balance as well as obtained by fitting the heat capacity data.

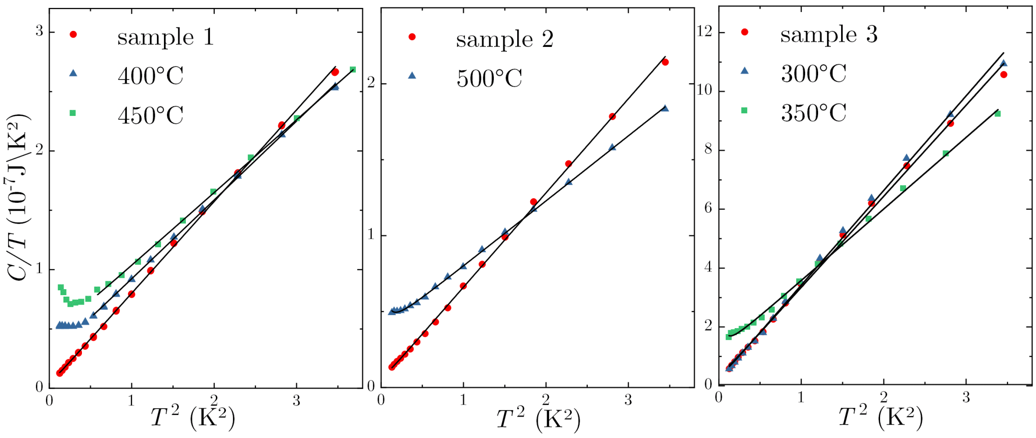

Figure 5.13: Heat capacity plotted as C/T vs. T^2 for samples 1 (left), 2 (middle) and 3 (right panel) before (red circles) and after (blue triangles, green squares) heat treatments. Fitting the data with $C/T = (m_{\mathrm{sample}} - m_{\mathrm{RuO_2}}) \cdot (\beta_{\mathrm{RuCl_3}} T^2) + m_{\mathrm{RuO_2}} \cdot C_{\mathrm{m,RuO_2}}/T$, indicated by the black lines, yields RuO_2 masses as listed in Tab. 5.2. $\beta_{\mathrm{RuCl_3}}$ was determined to be 1.29, 1.18 and 1.49$\cdot 10^{-5}$ J/gK^4 for sample 1, 2 and 3 respectively from the data of the untreated crystals. The heat capacity contribution of RuO_2 is described by $C_{\mathrm{m,RuO_2}} = M^{-1}_{\mathrm{RuO_2}}(\alpha T^{-2} + \beta T^3 + \gamma T)$ with $\alpha = 5.9 \cdot 10^{-5}$ JK/mol, $\beta = 2.25 \cdot 10^{-5}$ J/molK^4 and $\gamma = 5.77 \cdot 10^{-3}$ J/molK^2 [175].

Taking a closer look at the low temperature heat capacity over temperature C/T of the untreated samples, one can see that extrapolating the data towards absolute zero results in a finite non-zero heat capacity for all samples. Applying the previously described fit procedure to the pristine samples, a small fraction of RuO_2 can be found for all samples with values in the range of 1-2%.

To ensure that these are real values and cannot simply be attributed to the error of the measurement data or fit parameters, we once again look at the low temperature heat capacity of sample 1 as well as the corresponding addenda measurement which are depicted in Fig. 5.14. The first step for every heat capacity measurement was a separate investigation of the combined heat capacity of puck and grease. For this the exact amount of N grease later used for the sample measurement was placed on the HC platform and a measurement performed in the same way the sample measurement was done later. It should be noted that the addenda measurement also shows a non-zero Sommerfeld coefficient. This can however be explained by the contribution of metallic inclusions in the grease, heater, thermometer and platform. The sample was placed onto the grease using tweezers which were handled in such a way as to not touch the grease, thereby making sure that no material was removed from the sample holder. The following measurement yields a heat capacity containing a combination of those of the sample as well as puck and grease. Subtracting the addenda results in the part of the heat capacity stemming from the sample. Both sample and addenda heat capacity can be seen in Fig. 5.14(a). A fit routine as described in 3.7 combined with the quality of the raw data fit is used to determine the error bars for all measurements. Looking at the low temperature part of the heat capacity in Fig. 5.14(b), the dominant contribution to the addenda in this temperature region comes from the metal wires which are attached to the platform. The sample data was fitted using $C/T = (m - m_{\mathrm{RuO_2}}) \cdot (\beta_{\mathrm{RuCl_3}} T^2) + m_{\mathrm{RuO_2}} \cdot C_{\mathrm{m,RuO_2}}/T$ and the best fit is shown in black. A second fit assuming no $\mathrm{RuO_2}$ contribution and therefore a heat capacity meeting the origin, is shown in green. It can be seen clearly, that the green line does not meet the error margins of almost all data points. Fitting the data with a function through the origin thus is not possible and a $\mathrm{RuO_2}$ contribution is needed in order to best explain the heat capacity of untreated crystals at lowest temperatures.

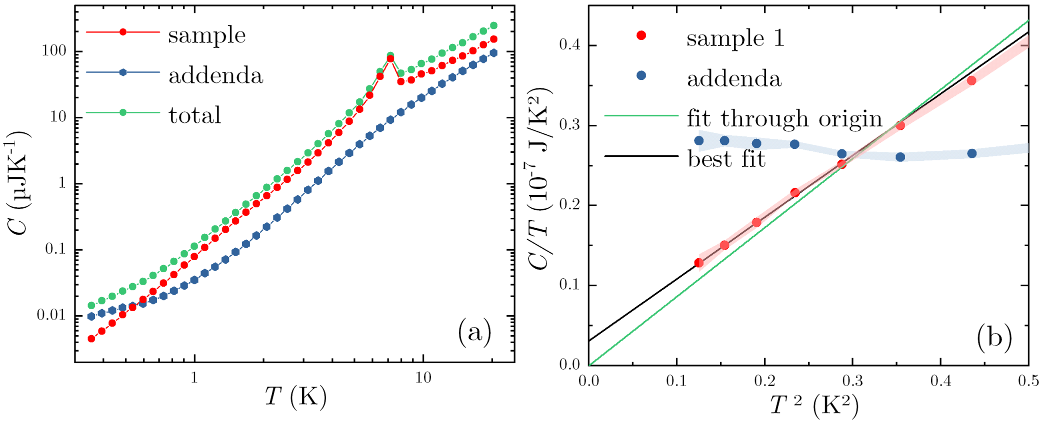

Figure 5.14: The sample heat capacity (shown here for sample 1) can be attained by subtracting the previously separately measured addenda from the total heat capacity both of which are shown in (a). (b) displays the low temperature heat capacity of sample 1 and the corresponding addenda. Here, the green line shows an attempt to fit the data points through the origin, while the black line shows the best fit.

Magnetic susceptibility

In order to investigate the influence of thermal annealing on the magnetic susceptibility, another crystal (sample 5) was heat treated at 500°C in Argon flow, analogous to sample 2. Measurements of the magnetic susceptibility in the *ab*-plane were performed before and after heat treatment. The susceptibility data depicted in Fig. 5.15 clearly shows a decrease in absolute values for the annealed sample. As a considerable part of the crystal is transformed into

RuO_2 during annealing, the mass must be adapted accordingly yielding the red plot. Now, the corrected plot shows nearly perfect overlap with the untreated sample. For further comparison, the RuO_2 contribution is plotted in yellow. As its absolute values lie several orders of magnitude below those of $RuCl_3$, no significant contribution to the annealed crystals magnetic susceptibility is made. As also observed for the heat capacity, a single transition at 7 K was found before and after heat treatment with no obvious signature at 14 K.

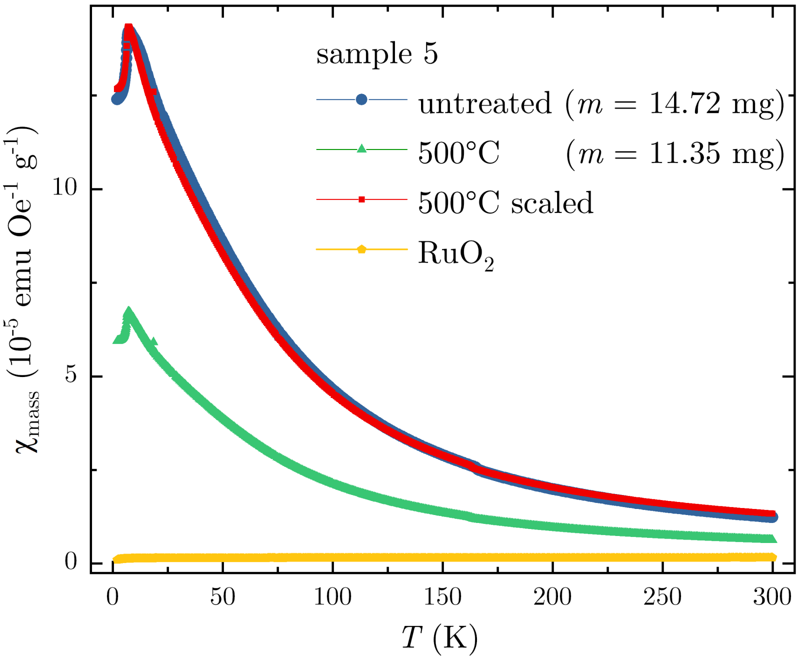

Figure 5.15: Temperature dependent magnetic susceptibility measured along the *ab*-plane with an applied magnetic field of 1 T. The blue line shows the data of the untreated sample, the green one that after heat treatment at 500°C. Scaling with the corrected mass of $RuCl_3$ yields the red plot, which shows good agreement with the untreated sample data. The susceptibility of RuO_2 is plotted in yellow for comparison, but does not significantly influence the heat treated sample since its absolute values are several orders of magnitude smaller than those of $RuCl_3$. The masses given in the legend are the total masses of the respective crystals.

Hirobe et al. [176] investigated the effect of curing α-$RuCl_3$ at 120°C in air for one hour on the thermal conductivity as well as magnetic susceptibility. For the thermal conductivity, they found no change, whereas the magnetic susceptibility increases for the heated samples which according to the authors is likely due to stacking faults which at first glance seems to contradict the data presented previously in this chapter. However, it should be noted, that the crystals investigated by Hirobe et al. all show a prominent feature at 14 K, whereas the samples investigated thus far in the frame of this thesis only show a single transition at 7 K. In order to compare with the published data, two more crystals were heated up to 120°C, this time under ambient conditions with increasing holding times and both magnetic susceptibility and heat capacity measurements performed.

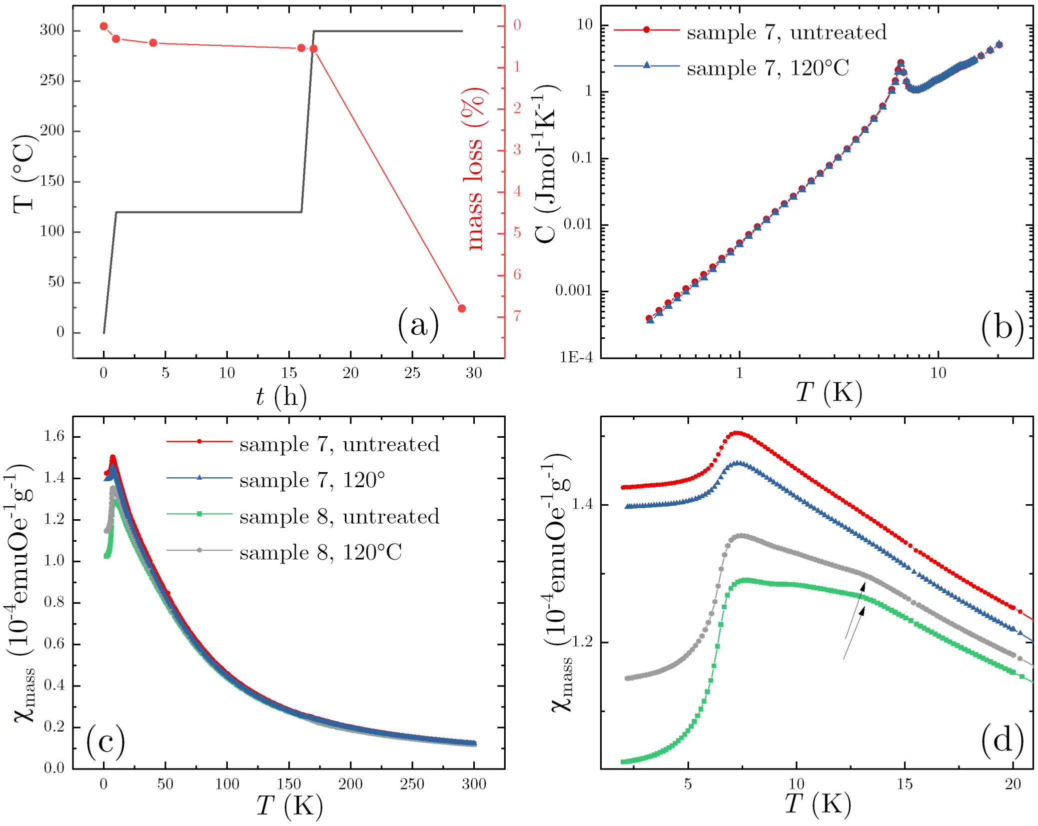

Figure 5.16: (a) Mass loss over time for heat treatments at 120, then 300°C. (b) Heat capacity before and after heat treatment at 120°C. (c) Magnetic susceptibility for heat treated samples 7 and 8. (d) Zoom-in on the low temperature magnetic susceptibility. While sample 7 shows a single feature at 7 K, for sample 8 a second feature at 14 K is present.

As depicted in Fig. 5.16(a), after heating the sample at 120°C for 1, 3 and 12 hours, a mass loss of less than 1% was detected. This is far less than that reported previously by Newkirk and McKee [170]. This study was performed using $RuCl_3$ powder, while this thesis deals with crystals, suggesting that crystals show a higher stability upon heating, likely due to the lower fraction of exposed surfaces, and either higher temperatures or even longer holding times are required to produce a more pronounced effect. Indeed, only after going to 300°C a substantial mass loss of about 7% was detected. No change in heat capacity for samples heat treated at 120°C could be observed (see Fig. 5.16(b)). The magnetic susceptibility before and after heat treatment is shown in Fig. 5.16(c) and (d). At first glance, some differences between both samples can be found: Firstly, the susceptibility of sample 7 is slightly higher than that of sample 8. Secondly, sample 8 shows a small, but visible additional feature at 14 K which is generally linked to the occurrence of stacking faults. For sample 7, a slight decrease of absolute values is found in good agreement with the detected mass loss. The magnetic susceptibility of sample 8, however, was found to slightly increase after heat treatment similar to the behaviour reported by Hirobe et al. Since the signature at 14 K is generally attributed to the presence of stacking faults, a likely explanation for the different behaviours of both samples can be given. While sample 7 shows a slight decrease in susceptibility after heat treatment due to the formation of a small RuO_2 fraction, the increase in susceptibility after heating for sample 8 can likely be explained by the presence of stacking faults in the crystal [176].

Electrical Transport

Another crystal (sample 6) was chosen in order to study the influence of thermal annealing on the in-plane electrical transport properties of α-$RuCl_3$. Measurements were performed using a PPMS by Quantum Design equipped with an ETO option. Contacts for a standard four-wire measurement were made using Pt wires and silver epoxy. The heat treatment was performed at 400°C in argon atmosphere in a closed silica ampoule. As the crystal surface of the annealed crystal shows increased porosity, extra care needs to be taken in order to ensure that the contacts are fixed to the sample while at the same time not removing any of the surface material.

While the resistivity of the untreated crystal is consistent with previous measurements by other groups clearly showing insulating behaviour [178–180], the resistivity of the annealed sample is decreased by several orders of magnitude. Both plots are shown in Fig. 5.17 along with the electrical resistivity of pure RuO_2 taken from literature [177]. Previous analysis showed that heat treatment at 400°C results in a RuO_2 fraction of about 10 mass%. While the influence of this RuO_2 fraction becomes apparent only at lowest temperatures in heat capacity, the electrical transport is clearly changed in the complete temperature range. Comparison with the resistivity of RuO_2 shows that the resistivity of the annealed sample is already closer to that of RuO_2 than to the pristine sample of $RuCl_3$.

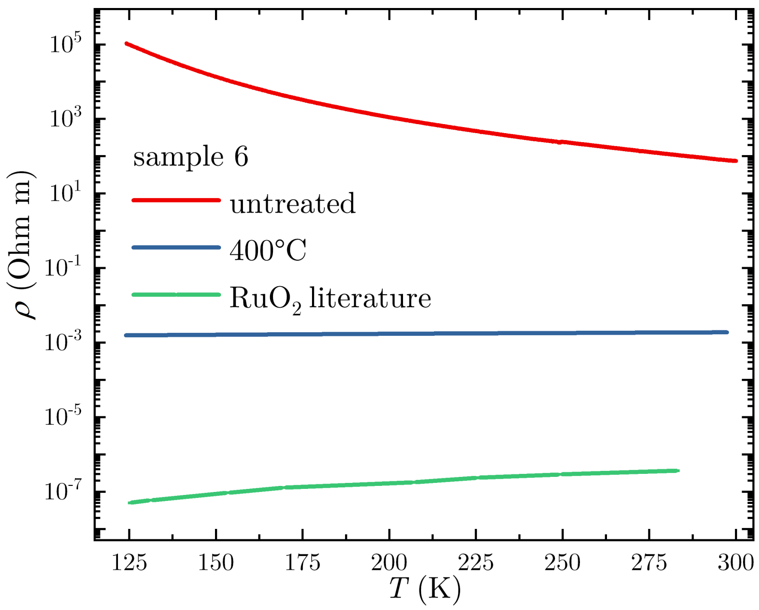

Figure 5.17: Electrical transport of another $RuCl_3$ crystal (sample 6) before (red) and after (blue) heat treatment at 400°C in the temperature range of 125-300 K [173]. For comparison, the resistivity of RuO_2 obtained from literature [177] is plotted in green.

5.4 Summary and Discussion

In summary, systematic heat treatments of high-quality single crystals of α-$RuCl_3$ were performed under closed Argon atmosphere, in Argon flow and in air. The maximum temperatures ranged from 120 to 500°C. A detailed listing of the samples along with the maximum temperatures during heat treatment and the executed measurements can be found in Tab. 5.3.

Low-temperature heat capacity measurements on crystals heat treated at $T \geq 350°C$ show increased values compared to the pristine crystals in the temperature range below 1.5 K. This effect becomes more pronounced with increasing maximum temperature during heat treatment.

On the surface of sample 1 clusters with highly increased ruthenium to chlorine ratio compared to the surrounding area were detected via combined SEM and EDX measurements, whereas sample 2 showed an overall increased Ru percentage (as high as 75 at%) on the surface after heat treatment at 500°C in argon flow. Performing the same heat treatment on another crystal (sample 4) revealed further insights on the penetration depth of the changed stoichiometry with the ruthenium percentage being elevated all the way into the crystal center, though the effect becomes less pronounced with increasing distance from the crystal surface.

Porous flakes with increased Ru content were removed from sample 4.

Powder XRD revealed them to consist of RuO_2 with no other side phases found.

A RuO_2 fraction is found in all heat treated samples offering a reasonable explanation for the increased heat capacity at low temperatures. The exact fraction of RuO_2 was determined via fitting the heat capacity data with a combination of heat capacities of $RuCl_3$ and RuO_2 with the mass of RuO_2 as the free parameter as well as calculated from mass loss determined by weighing the samples before and after heat treatments. Both values were in good agreement for all investigated samples with RuO_2 fractions being as high as 20% in the case of sample 2. Extending the fitting procedure to the heat capacity of untreated crystals indicates the presence of small RuO_2 contaminations of about 0.9-2% in all crystals.

	atmosphere	HC	EDX	$\chi(T)$	$\rho(T)$
sample 1	-	✓	✓	-	-
400°C	Ar, sealed	✓	✓	-	-
450°C	Ar, sealed	✓	✓	-	-
sample 2		✓	✓	-	-
500°C	Ar, flow	✓	✓	-	-
sample 3	-	✓	-	-	-
300°C	Ar, sealed	✓	-	-	-
350°C	Ar, sealed	✓	-	-	-
sample 4	-	-	-	-	-
500°C	Ar, flow	-	✓	-	-
sample 5		-	-	✓	-
500°C	Ar, flow	-	-	✓	-
sample 6	-	-	-	-	✓
400°C	Ar, sealed	-	-	-	✓
sample 7	-	✓	-	✓	-
120°C	air	✓	-	✓	-
sample 8	-	-	-	✓	-
120°C	air	✓	-	✓	-

Table 5.3: Overview of all samples along with the corresponding temperatures and atmospheric conditions for the heat treatments as well as performed measurements.

The magnetic susceptibility of sample 5 after heat treatment at 500°C in argon flow was found to be smaller than expected from prior measurements. Calculating the mass fraction of RuO_2 and adjusting the data accordingly lead to values in good agreement with those before heat treatment.

Furthermore, the resistivity of heat treated $RuCl_3$ was found to be several orders of magnitude smaller compared to the untreated crystals.

Heat treatments in air at 120°C did not lead to a detectable change in heat capacity and only small changes in the magnetic susceptibility. In the latter, the susceptibility was found to slightly decrease after heat treatment for a crystal with a single signature at 7 K, whereas a sample with an additional signature at 14 K, indicating the presence of stacking faults, showed a small increase in susceptibility.

Since it was not possible to perform measurements of the low-temperature thermal transport or thermal Hall effect on $RuCl_3$ in the frame of this thesis, no definite statement on the possible impact of small inclusions of metallic RuO_2 on such measurements can be made. Thus, further measurements by other groups would be necessary in order to give further insight into this question.

6 Microstructuring of β-Li_2IrO_3 for pump probe experiment

The Ir atoms in β-Li_2IrO_3 form a hyperhoneycomb lattice, making it another member of the class of Kitaev materials. Despite additional exchange interactions making it not a pure Kitaev system, bond-dependent anisotropic spin exchange occurs in this material [133, 181–184]. Below the transition temperature of $T_N = 37$-$38\,K$, an incommensurate magnetic order can be observed [182, 184]. This is a significantly higher temperature than observed for other Kitaev materials, making the ground state of β-Li_2IrO_3 comparably better accessible to time-resolved measurements. Measurements like ultrafast electron diffraction or dissipative pump-probe experiments could uncover more in depth information on the dynamics of the systems magnetic and structural ordering parameters, which in turn can be used to extract information on the strength of the correlated states bond-dependent interactions [185, 186].

However, in order to be able to conduct such measurements samples with a thickness of less than 1 µm are needed due to, for example, the limited penetration depth of the laser used for pump-probe experiments which limits the excitation volume of the sample. Ideally, thin films would be used in this case. However, for some samples it is not possible to grow high quality thin films. Another way to achieve thin samples would be exfoliation of single crystals. While this works especially well for 2D materials, achieving thin devices for 3D materials such as β-Li_2IrO_3 in this way is challenging. A third option would be the preparation of a thin lamella by FIB microstructuring. This was first attempted, but turned out to be difficult for β-Li_2IrO_3 as well. While the available crystals are rather small with diameters of rarely more than 200 µm, a surface of at least these dimensions is ideally necessary to achieve good quality measurements, meaning that the resulting FIB processed sample would essentially have to be a slice of the full crystal. After trying a few times, several problems were found to occur in all trials, such as uncovering cracks in the sample upon thinning or the sample breaking during transport to a substrate. Thus, another method had to be devised in order to achieve the desired result which will be described in this chapter along with some preliminary measurements performed on this sample as well as a bulk crystal for comparison.

6.1 Crystal Growth

Single crystals with a diameter of up to several 100 µm in the *ab*-plane can be grown via isothermal vapour transport of separated educts which was developed by F. Freund and A. Jesche and first published in [133]. Elemental iridium is placed on the bottom of a standard Al_2O_3 crucible upon which several rings with spikes are placed, followed by a spacer and an aperture with a 1 mm hole in the middle upon which elemental lithium is placed, as can be seen in Fig. 6.1. A lid is placed on top of the crucible, then the setup is placed inside a pre-heated muffle furnace, heated to 1050°C over the course of 5 h and held at this temperature for up to 2 weeks. Lithium and iridium react with air forming their respective oxides and transport due to the concentration gradient occurs resulting in crystal growth on the spikes. A more detailed description of the crystal growth process can be found in [133].

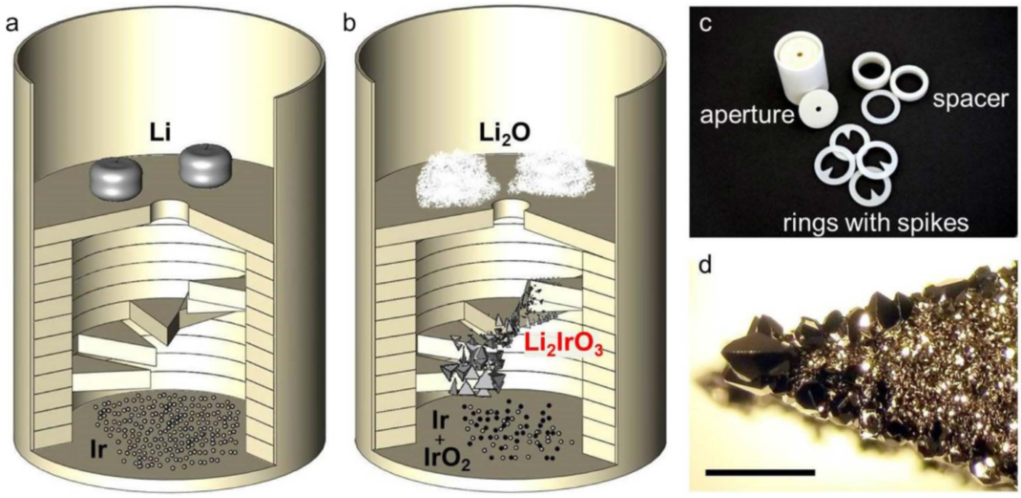

Figure 6.1: Crucible set-up for β-Li$_2$IrO$_3$ single crystal growth via vapour transport of separated educts. Copyright 2016, The Authors, published by Springer Nature. [133]

6.2 FIB thinning

A crystal was glued onto a STO substrate (10x5 mm diameter, thickness 0.5 mm) using two component epoxy with the crystals bottom surface perpendicular to *c* parallel to the substrate. Here, the sample was mounted at a distance of at least 1 mm to all substrate edges in order to meet alignment requirements for future measurements. The sample was then manually polished down as much as possible in order to save time and resources by limiting the amount of material that needed to be cut by FIB structuring. The sample was then mounted inside a combined FIB-SEM as shown in Fig. 6.2 with the crystal surface aligned parallel to the Ga^+ beam.

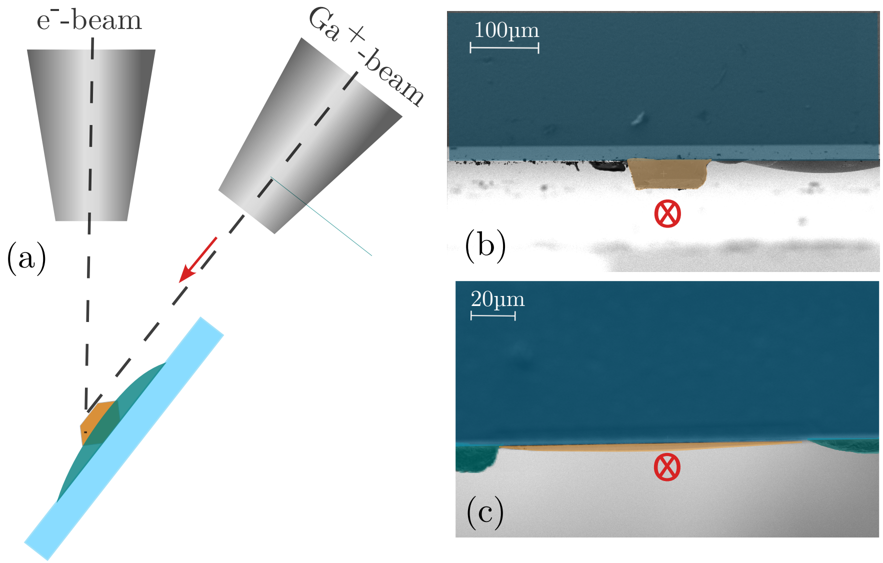

Figure 6.2: (a) FIB-SEM setup for thinning a crystal (orange) mounted on a sapphire substrate (light blue) with epoxy (teal) parallel to the surface. (b) SEM image perpendicular to the crystal surface before thinning. (c) SEM image perpendicular to the crystal surface after thinning. The red arrow in (a) and x in (b)-(c) indicate the direction of the Ga beam used for cutting.

Fig.6.2(b) and (c) show the sample before and after thinning using a voltage of 30 kV and starting with high probe currents up to 65 nA followed by progressively lower currents in order to avoid damage to the final sample. To compensate the reduced material removal for areas located further from the FIB column, the sample was tilted an additional 1-2° during cutting in order to achieve homogeneous thickness whenever necessary. In the last step, low energy milling was used in order to remove any embedded gallium ions, the absence of which was then confirmed by EDX. The resulting crystal thickness was determined to be about 1 µm.

The latter measurements were performed on the area marked in red in Fig.6.3(b) as well as a pristine crystal for comparison in order to check if any relevant sample damage occurred for the FIB sample.

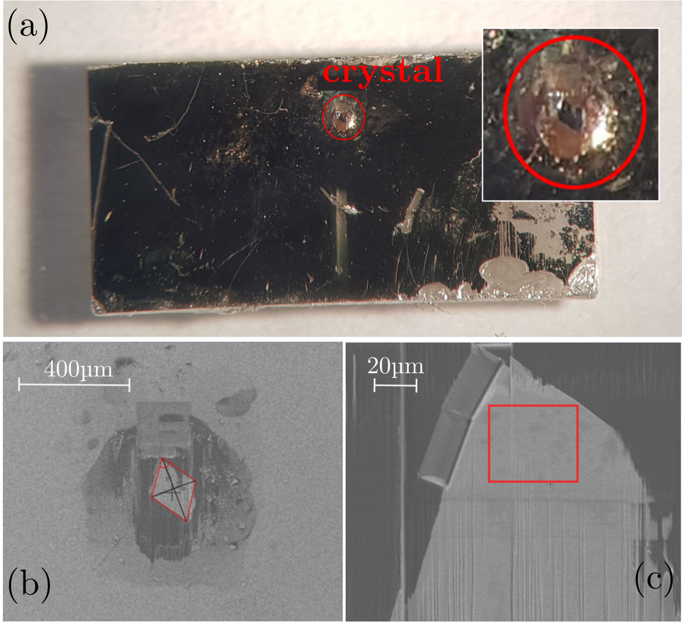

Figure 6.3: (a) Thinned crystal on gold covered sapphire substrate. (b) SEM image of the thinned sample. (c) The red square marks the area with thickness ~1 µm which will be used for measurements.

6.3 Properties of the thin lamella

In order to check whether the properties of the bulk crystal are preserved in the thinned sample, x-ray diffraction measurements were performed on both a bulk and a FIB sample. The measurements were performed by Dr. Nelson Hua (PSI Stuttgart) at the Materials Science Surface Diffraction (X04SA) beamline of the Swiss Light Source [187]. All data shown in this section as well as further information was published in [188].

The measurements were performed with an energy of 11.115 keV for the (004) and (135) lattice peaks at room temperature and 11.215 keV for measuring the incommensurate magnetic (-0.584,0,16) peak in the temperature range of 15-37.5 K.

The out of plane lattice structure as well as the lattice constant of the *c*-axis can be experimentally accessed by looking at the (004) peak shown in Fig. 6.4(a) and (b). Both bulk and FIB sample show lattice constants similar to those previously reported. While the bulk sample appears to consist of two main domains with a slight relative tilt, the FIB sample consists of several domains and shows a larger mosaic spread.

The in-plane lattice integrity probed by the (135) lattice peak shown in Fig.6.4(c)-(d) appears to be changed more by the FIB structuring than the out of plane lattice structure, represented by a comparatively larger correlation

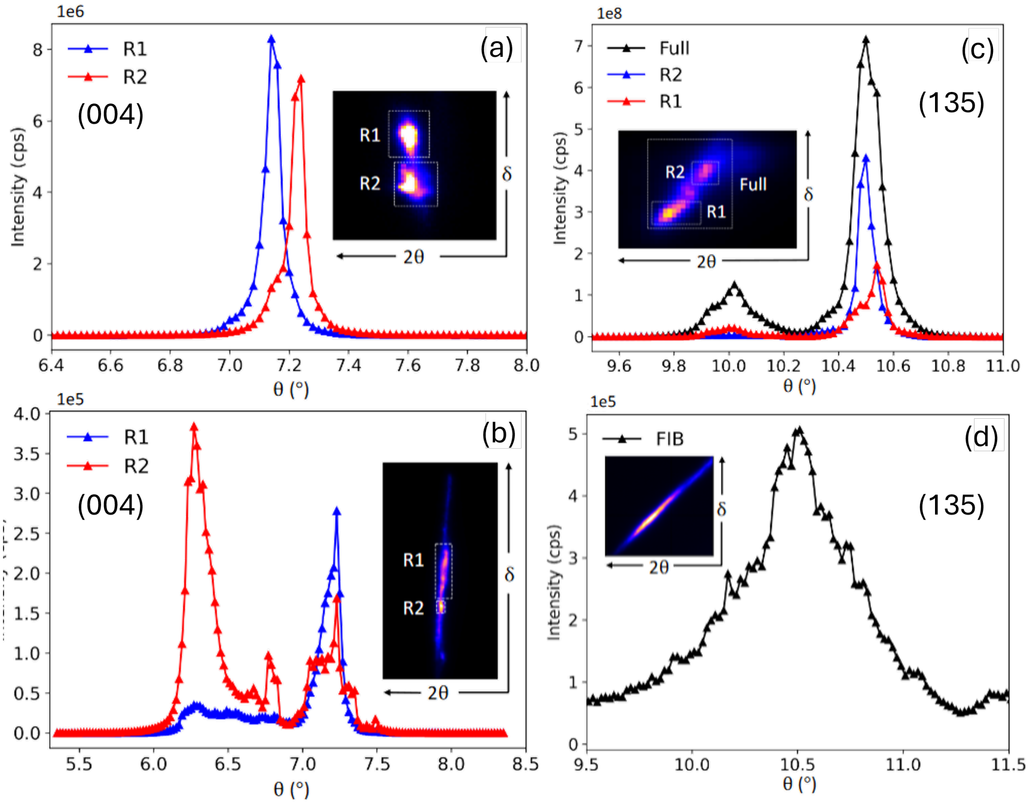

Figure 6.4: Rocking curve of the (004) peak for two domains R1 and R2 shown in the insets of the bulk (a) and FIB (b) sample. Both peaks appear at the same angle, however, the FIB sample shows multiple domains. Comparing the rocking curves of the (135) peak for the bulk (c) and FIB (d) sample, the latter shows a larger mosaic spread [188].

length determined from the full width half maximum of 0.068° and 0.600° for the bulk and FIB samples, respectively.

The magnetic structure can be probed via the the incommensurate resonant magnetic (-0.584,0,16) peak, shown in Fig. 6.5. Again, the FIB processing lead to a broadening of the peak compared to the bulk sample suggesting that the magnetic domain boundaries are determined by the lattice domains. Fig. 6.5 shows the peak completely disappearing for temperatures above $T = 37.5\,\mathrm{K}$ which is in good agreement with the reported transition temperature of 37 K [183, 184].

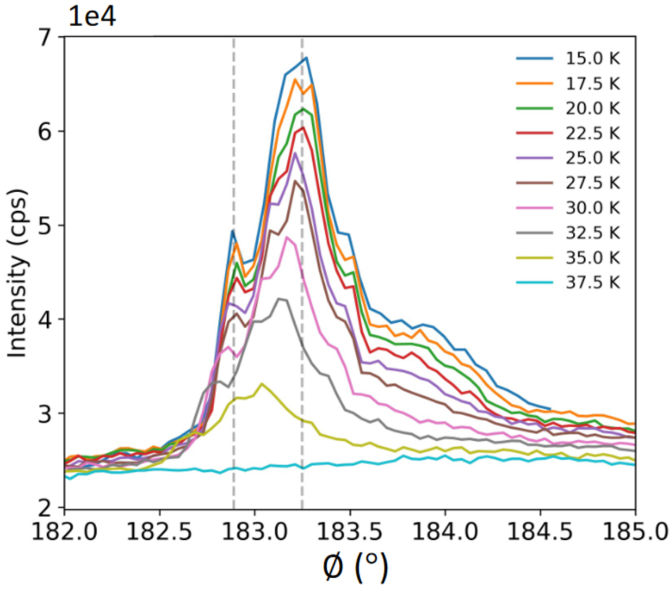

Figure 6.5: Full diffraction peak region in the temperature range of 15-37.5 K for the FIB sample. For temperatures above 37 K, the peak completely disappears [188].

6.4 Summary and Discussion

As would be expected for any technique requiring the use of high energy ions, FIB microstructuring can damage a materials surface in many different ways, for example by implanting foreign ions or creating dislocation defects beneath the surface by deposition of the beam energy into the sample [101]. While these effects can be avoided or repaired to a certain degree, it is necessary to check for each individual material whether the sample properties are influenced or changed by FIB microstructuring in a way relevant to the desired use or application. Reducing a β-Li$_2$IrO$_3$ single crystal down to a thickness of about 1 µm using FIB microstructuring resulted in a sample which, while showing a larger mosaicity and thus smaller domains, still retained the same properties as the bulk sample. X-ray diffraction measurements show that the magnetically ordered state and thus the electronic structure of the FIB processed β-Li$_2$IrO$_3$ single crystal is preserved. Furthermore, both bulk and FIB sample follow the same temperature dependence and the c lattice parameter remains mostly unchanged by FIB processing meaning that no significant strain due to dopants was introduced. Thus, it could be shown that further experiments, such as pump-probe x-ray diffraction or ultrafast electron diffraction measurements, can be executed in good conscience on a sample prepared in the described fashion.

7 The magnetic kagome metal CrRhAs

The kagome lattice, which is named after a pattern used in Japanese basketry, consists of regular hexagons surrounded by equilateral triangles which gives rise to strong geometrical frustration. If the magnetic ordering is antiferromagnetic, the kagome lattice can show exotic properties like classical or quantum spin liquids [7–9]. One example for such an antiferromagnetic kagome magnet is CrRhAs. In the past, studies of its magnetic and electronic properties have been conducted on polycrystalline samples [189–192]. A recent theoretical paper [193] brought this material back into the focus of research predicting the occurrence of exotic properties. Thus, this chapter deals with the growth of single crystalline CrRhAs samples of several millimetres length and a study of its magnetic, electrical and thermal properties.

Crystal Structure

The ternary arsenide CrRhAs is a member of the group of XYZ compounds with space group $P\overline{6}2m$ which crystallize in a hexagonal ZrNiAl crystal structure. The structure consists of two metal sublattices X and Y with Z atoms integrated in both in a 1:2 ratio. The structure shows a 6-fold rotoinversion symmetry which allows for the description of both metal layers as a twisted kagome lattice with Z atoms located in high symmetry positions inside the layers, which can be seen in Fig.7.1(a). The magnetic moment in this system is carried by the Cr atoms.

The two sublattices can be divided into one which is often magnetic, thus showing only small deviations from the ideal kagome lattice and one which is mostly non magnetic. The Coulomb interaction with the central ligands is minimized in the magnetic sublattice giving rise to magnetism and, if the interaction is of an antiferromagnetic nature, frustration. In the non magnetic sublattice, there are two ligand atoms per unit cell and the metals combine into trimers (Y_3Z_2 triangles) with covalent bonding resulting in no or only small magnetism. It was found that many XYZ compounds are magnetic, when the X atoms form the magnetic sublattice showing frustration as described within the ideal Kagome model. The exchange interactions J_1-J_4 between Cr atoms within the *ab*-plane are shown in Fig. 7.1(b).

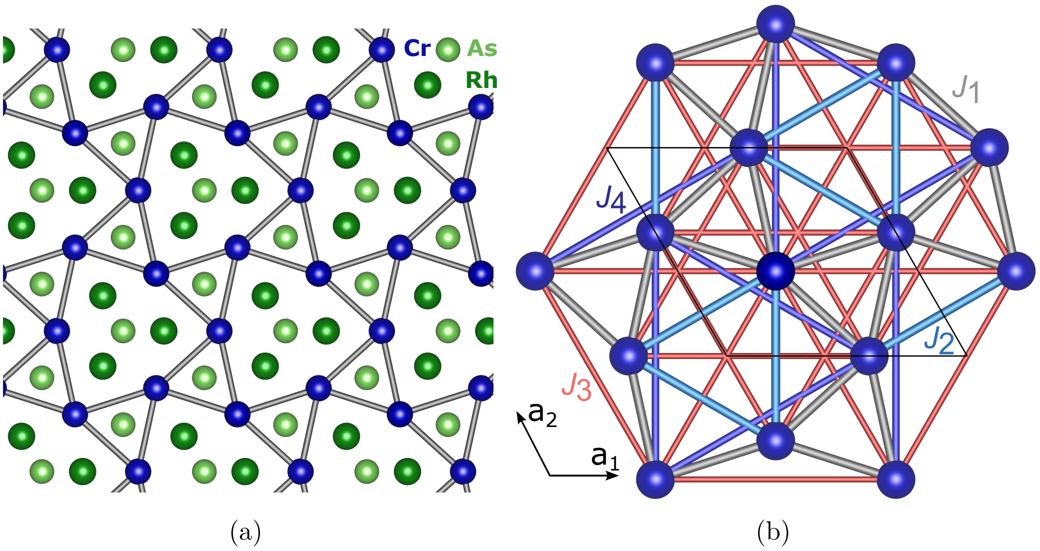

Figure 7.1: Crystal structure of CrRhAs. The twisted kagome structure formed by the Cr atoms (blue) is shown in (a) along with the atomic positions of Rh (dark green) and As (light green). (b) depicts the exchange interactions J_1-J$_4$ between Cr atoms within the *ab*-plane (adapted from [193]).

Theoretical Description and Predictions

This section is mostly based on a paper by Huang et al. [193].

Looking at the magnetic pattern of CrRhAs, the structure can be further divided into three symmetry equivalent Cr sublattices, which shall be referred to as Cr1, Cr2 and Cr3. In plane interaction between a Cr1 atom and its respective nearest neighbours up to fourth neighbours are depicted using different colours in Fig. 7.1. Each interaction can be described using a Heisenberg term $J_n \boldsymbol{s}_i \cdot \boldsymbol{s}_j$ with J_n describing the Heisenberg coupling between n-th nearest neighbours and $s_{i=1,2,3}$ the normalized spin operators.

The total energy of the magnetic pattern can then be described as

$$H = E_0 + H_{\text{Heisenberg}} + H_{\text{ring}} \tag{7.1}$$

with $H_{\text{Heisenberg}} = \sum_{i<j} J_{ij} \boldsymbol{s}_i \cdot \boldsymbol{s}_j$ and H_{ring} describing the ring exchange on a Cr triangle.

Modelling different spin spiral configurations in order to investigate the magnetic coupling of Cr atoms as well as performing noncollinear periodic calculations and fitting all obtained energy curves, Huang et al. find antiferromagnetic J_2 coupling to be the dominant exchange interaction being significantly larger (by a factor 10) than the ferromagnetic interaction J_1. J_3 and J_4 are both determined to be antiferromagnetic as well and of the same order as J_1. Thus, the dominant contribution for the Heisenberg Hamiltonian is antiferromagnetic. Despite the small interlayer distance, regarding its magnetism the material can be described almost two-dimensionally, since the interlayer exchange interactions are significantly smaller compared to those in plane. In the ground state, the J_2 bonds form isolated triangles with 120° order with either positive or negative vector chirality consisting of one of each Cr atom Cr1, Cr2 and Cr3. Huang at al. [193] thus come to the conclusion that CrRhAs shows a rather unusual Hamiltonian in several regards. On the one hand, the leading exchange interaction within the twisted kagome plane was found to be antiferromagnetic coupling. On the other hand, a ring exchange term needs to be added in order to obtain fits of ideal quality. This, combined with the ground state made up from isolated triangles, makes the twisted kagome material CrRhAs an interesting candidate for further experiments with the potential to show exotic phenomena such as a topological Hall effect.

7.1 Crystal Growth

Despite previous reports [189–192] covering both measurements of magnetization and electrical resistivity of polycrystalline samples of CrRhAs, CrNiAs and several more compounds of this family, to the best of our knowledge there was no report of successful growth of single crystalline CrRhAs prior to this work. All measurements reported so far were performed on polycrystalline CrRhAs which was grown by mixing stoichiometric amounts of the elements, grinding and heating several times before pressing them into a pellet.

Thus, a working method for achieving the growth of crystals of several millimetres size and sufficient weight for the desired measurements had to be found.

After trying several different fluxes, namely In, Ga, Pb and Zn, which all yielded several different crystals, however none of the desired compound, Bi was found to be well suited for this case. After varying the stoichiometry of the starting materials several times depending on the obtained crystals, the composition of which was determined via EDX, an ideal ratio of Cr:Rh:As:Bi of 1:2:1:15 was found. Needle-shaped crystals of several millimetres length with maximum thickness of about 200 µm were obtained in this way.

Due to the toxicity and possible reactivity with air, for each growth, the starting materials were placed in an Al_2O_3 Canfield crucible set [194], consisting of two crucibles and a stainer, inside a glovebox which was then sealed in a quartz ampoule under Argon atmosphere. The sealed ampoule was then placed in a Muffle furnace located in a closed fume hood, heated to 600°C and held at this temperature for 6 h to ensure that the arsenic is fully dissolved in the flux. Next, the temperature was increased for 3 h until the maximum temperature of 1100°C was reached and held for 2 h before slowly cooling down to about 650°C over the course of a week. The crystals were separated from the flux by centrifugation. Remaining flux fractions were removed by placing the crystals in HCl for two weeks. An opened crucible as well as extracted crystals are depicted in Fig. 7.2.

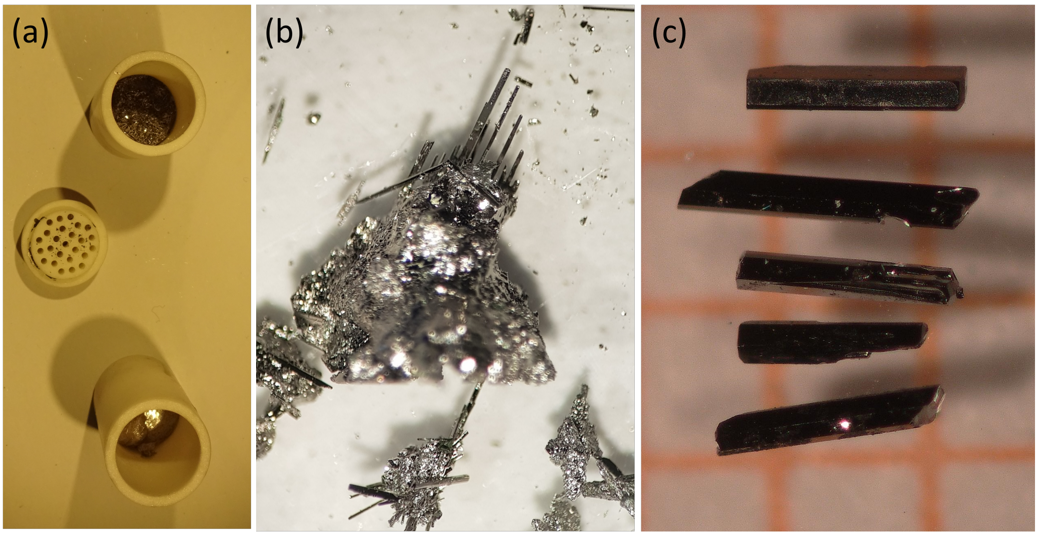

Figure 7.2: (a) Open Al_2O_3 crucible after centrifugation. The crystals are located in the upper part, while the flux has been moved through the strainer to the lower part. (b) Crystals stuck in flux after extraction from the crucible. (c) CrRhAs crystals separated from flux. Any remaining flux was removed by treating the crystals in HCl for two weeks.

Longer holding times or variations of the applied temperature profile did not result in larger or thicker crystals. Upon trying to further vary the stoichiometry, it was observed that crystals of CrRhAs appear to grow only within a rather narrow window of the stoichiometric ratio of 1:2:1 of the starting materials Cr:Rh:As.

7.2 Structural and Chemical Characterization

The structure and chemical composition of the obtained crystals was investigated using powder x-ray diffraction and energy dispersive x-ray spectroscopy (EDX).

X-ray Diffraction

Due to the limited sample size, several crystals were ground into a fine powder in order to perform x-ray diffraction measurements. The resulting diffractogram can be seen in Fig. 7.3(a) clearly identifying the material as the desired (111) compound. The remaining peaks can be assigned to bismuth. Since the XRD was performed on crystals as extracted from the crucible without placing them in HCl and thus some flux remaining on the crystals included in the measurement, a significant amount of bismuth was detected.

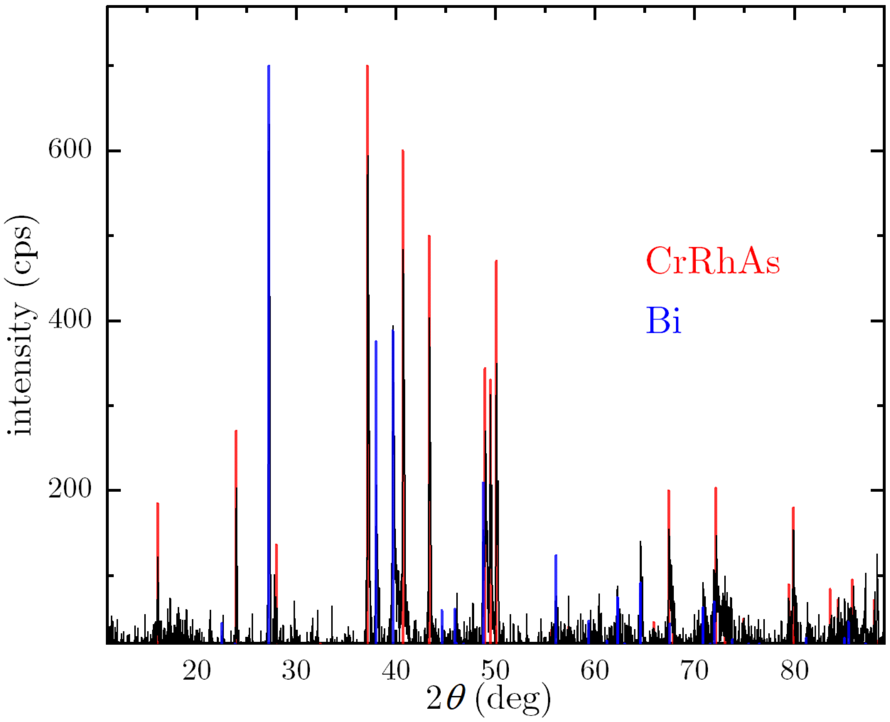

Figure 7.3: (a) Powder diffractogram of several ground CrRhAs single crystals. The remaining peaks are explained by some residue of Bi flux included in the powder, since the crystals were ground as extracted from the crucible.

EDX

Due to the limited amount of crystals and the need to grind crystals in order to obtain a good quality diffractogram via powder XRD, EDX was used as an alternative method to confirm the crystal stoichiometry.

Several needle shaped crystals were investigated making sure that future measurements were indeed performed on the right crystals. Once a working growth procedure was established, all needle shaped crystals were determined to be indeed the (111) compound. Other side phases, such a rhombus shaped RhAs and cubic Rh crystals, could not be eliminated from the resulting product due to the overlap of the respective temperatures needed for crystal growth. However, the different habits easily allow for the separation of the different compounds. EDX showed a close to perfect Cr:Rh:As ratio of 1:1:1 with a maximum deviation of 4 % which might be at least partially attributed

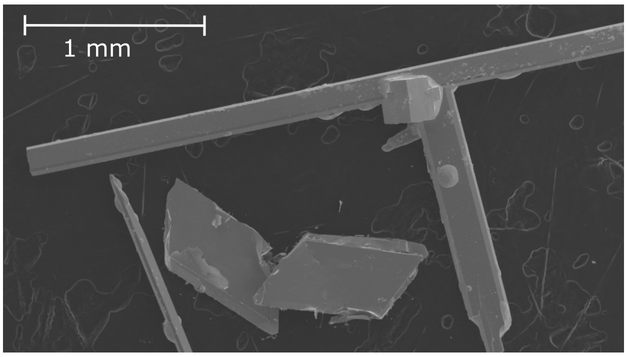

sample	Cr	Rh	As
# 1	0.99	0.97	1.04
# 2	1.00	0.96	1.04
# 3	0.94	0.98	1.08
# 4	0.98	1.00	1.02
# 5	0.99	0.97	1.04

Figure 7.4: (a) Crystals obtained during the previously described crystal growth. EDX was used to identify the needle shaped crystals as the desired CrRhAs. Rhombus shaped RhAs and cubic Rh crystals were found as side products. The bright spots are bismuth flux which was not fully removed during centrifugation. (b) Average composition of five different samples determined by EDX and normalized to add up to a value of 3.

to different error sources stemming from the measurement itself, such as deviations from a perfect parallel orientation of the crystal and the sample holder or some unevenness on the surface.

7.3 Physical Properties

Measurements of the heat capacity, field and temperature dependent magnetization and electrical transport were performed on several crystals including both bulk and FIB structured samples.

Heat Capacity

Due to the low mass of individual crystals of below 0.1 mg and the corresponding small signal, the heat capacity of CrRhAs was determined by measuring several crystals together.

As can be seen in Fig. 7.5, the heat capacity shows a single peak at $T_{\mathrm{N}} = 148\,\mathrm{K}$ which is lower than the value reported for polycrystalline samples of $T_{\mathrm{N}} = 165$ [189–191] or 172 K [192] determined from magnetic susceptibility. Plotting C/T vs T^2 as shown in the left bottom inset in Fig. 7.5 reveals a Sommerfeld coefficient of $\gamma = 30\,\mathrm{mJ/molK^2}$ which is a rather sizeable value for 3d systems and $\beta = 0.4\,\mathrm{mJ/molK^4}$ yielding a Debye temperature of $\theta_{\mathrm{D}} = 242\,\mathrm{K}$.

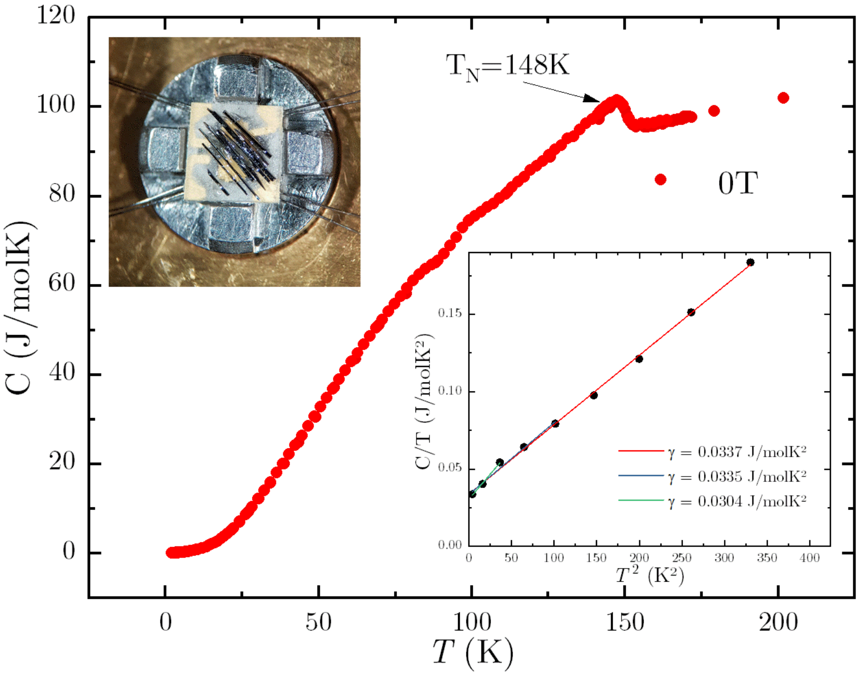

Figure 7.5: Temperature-dependent heat capacity of CrRhAs. The measurement was performed using several single crystals arranged as shown in the inset (top left) in order to achieve a sufficiently large signal. A peak at $T = 148\,\mathrm{K}$ is observed. Plotting C/T vs T^2 (bottom right inset) reveals a Sommerfeld coefficient of roughly 0.03 J/molK^2.

Field and Temperature dependent Magnetization

CrRhAs shows a linear field dependent magnetization for both measurements parallel and perpendicular to the c-axis with a slightly lower slope for the perpendicular measurement up to the maximum field of 8 T as depicted in Fig. 7.6(a). For polycrystalline samples, a linear field dependent magnetization was observed up to the maximum applied field of 15 T [191].

The magnetic susceptibility shows a clear peak at around 150 K for both measurements parallel and perpendicular c below which the susceptibility decreases towards lower temperatures until it increases again below 25 K. The Néel temperature is determined by looking at the maximum in $\mathrm{d}(\chi \cdot T)/\mathrm{d}T$ found at 148 K which is in good agreement with the signature observed in the heat capacity.

Plotting the inverse susceptibility shows a distinct non Curie-Weiss behaviour in the temperature region between 155-300 K with the slope decreasing with increasing temperature. Similar behaviour has been previously observed on powder samples for which different fitting procedures were utilized. The first reported data by Ohta et al. [189], shown in grey in Fig. 7.6(b), was analysed

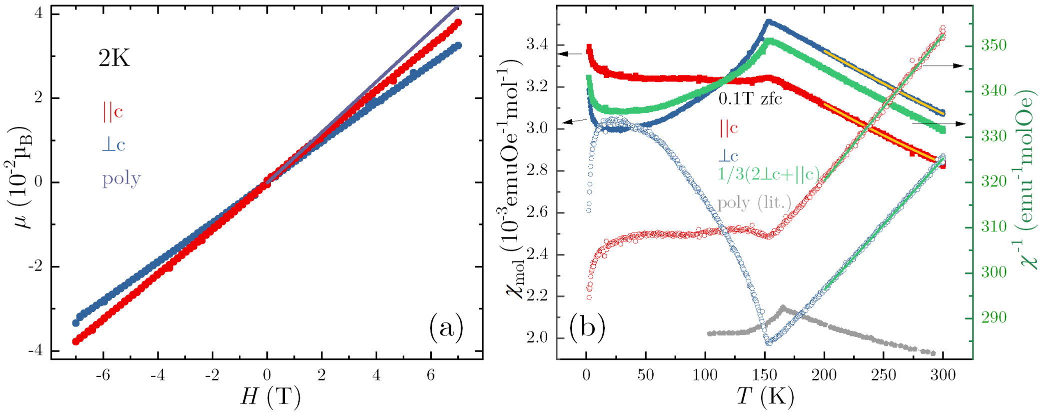

Figure 7.6: Field (a) and temperature dependent (b) magnetization of CrRhAs single crystals along and perpendicular to the *c* axis. $\mu(H)$ shows linear behaviour for fields up to at least 8 K, while $\chi(T)$ shows a $T_N = 148\,\mathrm{K}$ determined from the maximum in $\mathrm{d}(\chi \cdot T)/\mathrm{d}T$. $\chi^{-1}(T)$ shows a divergence from linear behaviour even above the transition temperature. The data for the polycrystalline sample from literature is shown in purple [191] and grey [189].

using a $\chi = C/(T-\theta)+\chi_0$ fit, while other publications used a $\chi = C'/(T-\theta')^{\gamma}$ approach [189, 190] which was shown to yield more accurate results if the fitting is done at temperatures close to T_C [195].

Kanamota et al. suggested that this deviation from linear behaviour might be attributed to spin fluctuation effects [190].

Fitting the single crystal data accordingly, the first approach yields an offset χ_0 in the order of $10^{-4}\,\mathrm{emuOe^{-1}mol^{-1}}$ which is an order of magnitude smaller than reported in literature. The Curie constant of both parallel and perpendicular susceptibility is close to 2 $\mathrm{emuKmol^{-1}}$ which is significantly larger than that reported in literature. The resulting effective moment $\mu_{\text{eff}} = 4\,\mu_B$, however, is similar to the theoretically predicted value of $\mu_{\text{eff}} = 3.87\,\mu_B$ [193]. The Curie Weiss temperature is found to be $T_{CW} = -596\,\mathrm{K}$ or $T_{CW} = -594\,\mathrm{K}$ for the parallel or perpendicular measurements respectively for a fit in the temperature range of 160-300 K. Once again, this is very close to the theoretically predicted value of $T_{CW} = -578\,\mathrm{K}$ assuming spin 3/2 and a quantum factor $S(S+1) = 5/3$ [193]. Fitting the data with an additional γ coefficient results in this variable being set close to one (0.94 and 0.95 for parallel and perpendicular respectively) and thus similar C' and T_{CW} as for the other fit. It should be mentioned, though, that in order to more accurately determine these values, measurements at higher temperatures would be preferable. This was attempted but resulted in unusable data due to unknown reasons.

Huang et al. suggested the definition of "instantaneous" Curie-Weiss parameters $C(T) = 1/(\mathrm{d}\chi^{-1}/\mathrm{d}T)$ and $\theta(T) = T - C(T)/\chi(T)$ [193]. Plotting the single crystal data in this fashion, $C(T)$ was found to increase for increasing temperatures, while $\theta(T)$ becomes more antiferromagnetic which is in good agreement with the behaviour predicted in [193].

Electrical Transport

Temperature dependent measurements of the longitudinal as well as the Hall resistivity were conducted on both manually contacted and FIB structured samples. Due to the needle shape of the obtained single crystals and an average thickness of no more than 100 µm, manual contacting for Hall measurements proved difficult and was only successful in one case. Thus, additional FIB microstructuring was once again employed in order to apply Hall contacts to the crystals. For this, the crystals were first polished on one side, glued onto a sapphire substrate and polished down even further in order to limit FIB cutting time. The sample was then covered with gold, before cutting a structure as shown in Fig. 7.7. The meandering structure used for all current and voltages contact is designed in such a way as to limits the stress and strain on the sample during cooling and warming during the measurement and thus serves as a prevention for contact breakage during measurements. In the last step, the gold coating was removed from the measurement bar using low kV FIB milling. EDX was used to check for any remaining contaminations.

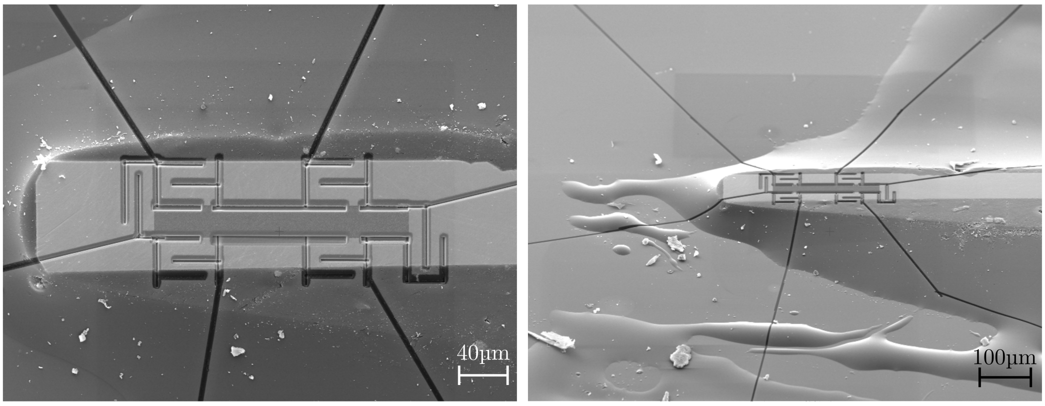

Figure 7.7: CrRhAs crystal contacted for longitudinal and Hall measurement by FIB microstructuring. The crystal was first polished, then glued onto a sapphire substrate, coated with gold and structured as described in 3.3.

Longitudinal Resistivity

Several needle shaped crystals were contacted for four wire measurements along the c axis.

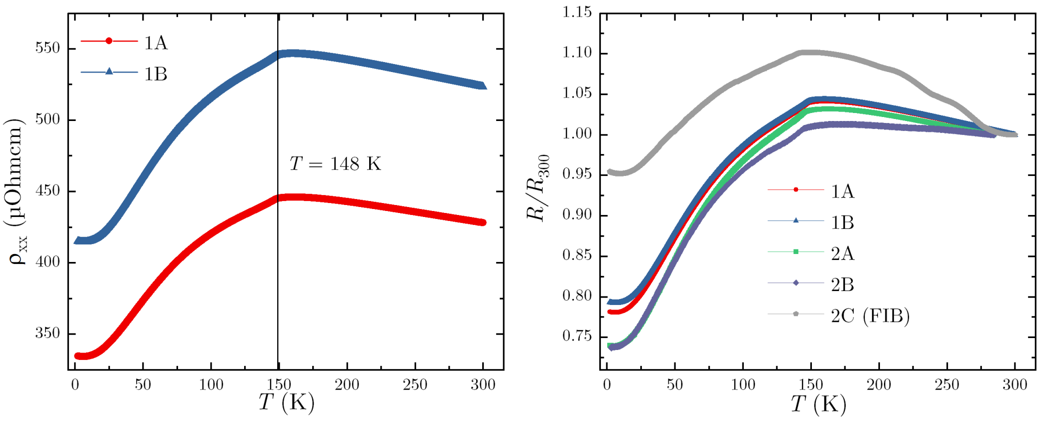

Figure 7.8: Temperature dependence of the longitudinal resistivity for several single crystals from different batches contacted for four wire measurements by manually attaching platinum wires or FIB structuring. For all samples, a Néel temperature of T_{N}=148 K was observed, below which the resistivity decreases towards low temperatures.

As can be seen in Fig. 7.8, the temperature dependent resistivity increases until the Néel temperature of $T_{\mathrm{N}} = 148\,\mathrm{K}$, below which it decreases until it approaches a constant residual resistivity at lowest measured temperatures. The FIB structured sample shows a somewhat higher R/R_{300} value which can probably be attributed to the use of FIB platinum for contacting, yet the overall behaviour is similar to the directly contacted samples. At low temperatures, the data can be best fit by a combination of residual resistivity, electron-electron and electron-phonon contributions written as $\rho = \rho_0 + aT^2 + bT^5$ with $\rho_0 = 3.3\text{-}4.1 \cdot 10^2\,\mu\Omega\mathrm{cm}$, $a = 1.4\text{-}2.0 \cdot 10^{-2}\,\mu\Omega\mathrm{cm}\ \mathrm{K}^{-2}$ and $b = 1.0\text{-}1.6 \cdot 10^{-7}\,\mu\Omega\mathrm{cmK}^{-5}$.

Magnetoresistance

Magnetoresistance was measured with the field applied perpendicular to the c-axis. At low temperatures, the magnetoresistance shows a positive cubic behaviour which is induced by Lorentz force [196], whereas at temperatures above the Néel temperature, the magnetoresistance first significantly decreases, before a sign reversal is observed for the data recorded at 200 K. This negative value in the paramagnetic regime could be explained by the suppression of spin fluctuations by the increase of the effective field due to the application of an external magnetic field and is also found in other antiferromagnetic metals [196, 197].

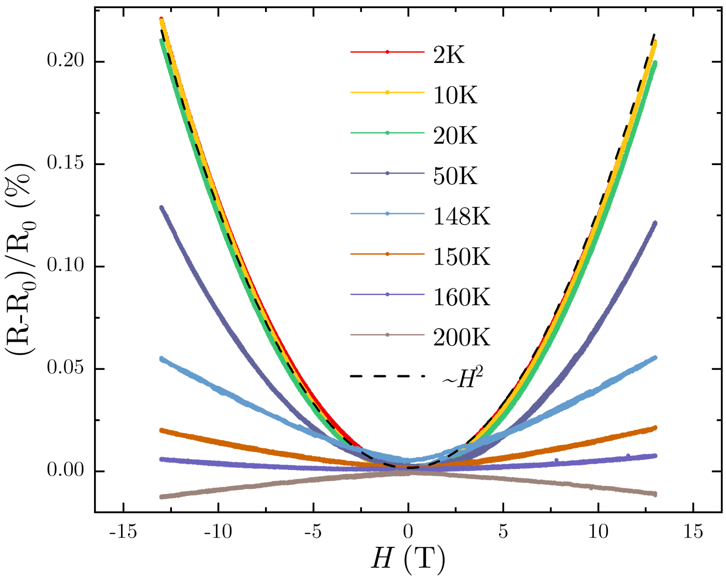

Figure 7.9: Magnetoresistance of a CrRhAs single crystal with the field applied perpendicular to the c-axis for temperatures in the range of 2-200 K. At low temperatures, a cubic behaviour can be observed.

Hall Measurements

While theory found an unusual magnetic Hamiltonian for CrRhAs and predicted the emergence of interesting phenomena such as anomalous Hall effect for this system, the measurements performed in this thesis with the current applied along the c axis and the magnetic field perpendicular to c revealed a purely linear Hall resistivity for both the directly contacted and the FIB structured samples.

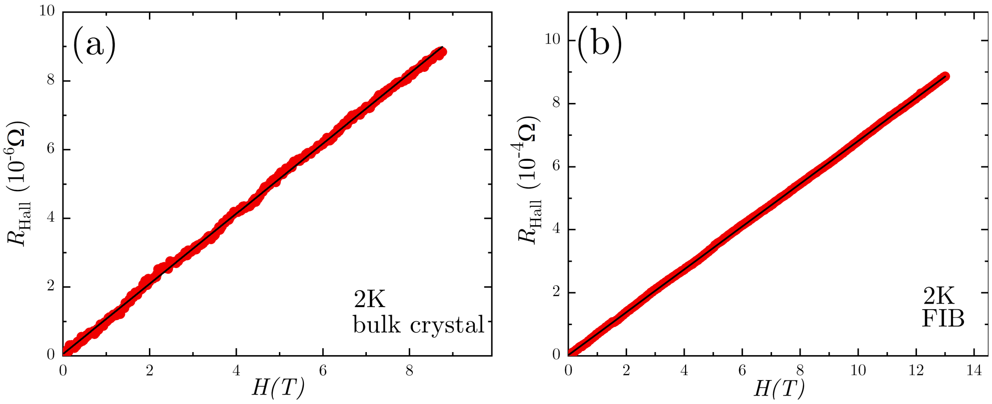

Figure 7.10: Hall resistance of a directly contacted crystal (a) and a FIB structured sample (b) showing linear behaviour with a charge carrier density of $\sim 10^{22}\,\mathrm{cm}^{-3}$.

The charge carrier density was determined to be about $n = 1 \cdot 10^{22}\,\mathrm{cm}^{-3}$ for the FIB structured and $n = 3 \cdot 10^{22}\,\mathrm{cm}^{-3}$ for the bulk sample.

7.4 Summary and Discussion

Here, for the first time successful growth of needle shaped single crystals of CrRhAs of up to several millimetres in length was achieved. For this the elements were weighed in a stoichiometric ratio of 1:2:1 along with 15 parts bismuth flux.

The Néel temperature determined from heat capacity, resistivity and magnetic susceptibility measurements conducted on single crystals in the temperature range of 2-300 K is shown to be T_N=148 K which is smaller than the values reported for polycrystals. The determined Curie-Weiss temperature of -(596-594) K and effective moment of 4 μ_B are in good agreement with the values suggested by theory.

However, despite the potential for exotic behaviour such as anomalous Hall effect due to the materials unusual magnetic Hamiltonian, all measurements performed on both bulk single crystals and FIB structured samples of CrRhAs hint at the system behaving like an ordinary metal.

Hall measurements revealed a completely linear Hall resistance, while longitudinal Hall resistance followed a H^2-behaviour at low temperatures with values decreasing towards higher temperatures. Thus, both Hall effect and low temperature magnetoresistance resemble that typically seen for metals, while $R(H)$ at higher temperatures is similar to what is seen in other antiferromagnets. Hall measurements on FIB structured samples within the kagome plane proved difficult with large noise and unexplained jumps in the temperature dependent resistivity and overall rather noisy Hall data. Therefore, it might be interesting to revisit this in the future and gain more insight into the materials in-plane electrical transport properties.

8 Impact of substitution on the ferromagnetic transition in CrNiAs

Unlike for systems with ideal kagome lattices, so far not many studies on materials with distorted kagome lattices have been conducted in regard to exotic physics, such as quantum bicriticality [198] or a spin ice state [199, 200]. Here, CrNiAs was chosen for several reasons. Similar to CrRhAs and the above mentioned systems YbAgGe and HoAgGe, CrNiAs crystallizes in a distorted kagome lattice of the ZrNiAl structure, but, contrary to the antiferromagnetic CrRhAs, for temperatures below T_C=170-190 K polycrystalline CrNiAs was reported to show ferromagnetic order [192, 201–203] breaking time reversal symmetry. No inversion center exists in the materials lattice structure. This combination of ferromagnetic ordering and lack of an inversion center was observed along with the existence of a ferromagnetic quantum critical point [204] in other materials such as $CeRh_6Ge_4$ which becomes a strange metal at the pressure induced QCP [205]. Thus, investigating CrNiAs could steer the search for ferromagnetic quantum phase transitions in a new direction.

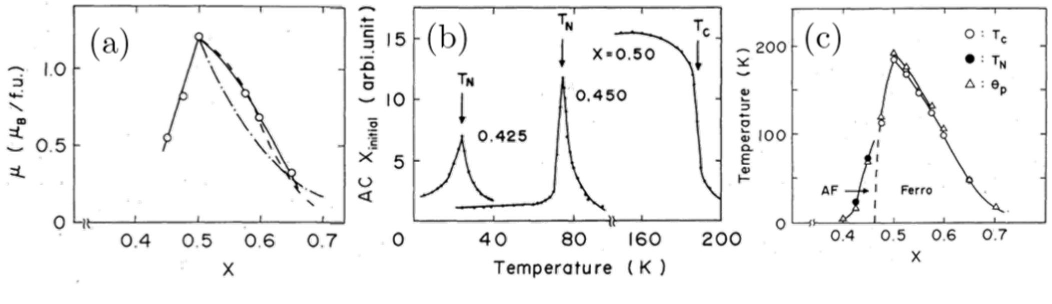

Figure 8.1: (a) Spontaneous magnetization for $(Cr_{1-x}Ni_x)_2As$ with x=0.425-0.6 at 4.2 K plotted as a function of the Ni concentration x. (b) AC susceptibility for different values of x. (c) Magnetic phase diagram showing the transition from ferromagnet to antiferromagnet at x=0.45. A maximum is reached at x=0.5 in both transition temperature and magnetic moment [201].

Unlike for CrRhAs, for which previous studies were limited to polycrystalline samples, single crystal growth was reported for $(Cr_{1-x}Ni_x)_2As$ with x=0.425-0.6 by Iwata et al. as early as 1980 [201]. In this report, the crystals were obtained by thermal annealing of the starting materials at 950°C, followed by grinding and a second thermal annealing at 1350°C. It should be mentioned though, that the reported x values are those of the nominal chemical composition of the starting materials. Iwata et al. reported a strong dependence of the spontaneous magnetic moment on the Cr:Ni ratio. $(\mathrm{Cr}_{1-x}\mathrm{Ni}_x)_2\mathrm{As}$ is shown to be an antiferromagnet in the range of $0.4<x\leq0.45$ and shows ferromagnetic behaviour for $0.45<x\leq0.7$. The magnetic transition temperature as well as the magnetic moment reach a maximum at x=0.5 with T_C=195 K and μ=1.19 μ_B, as can be seen in Fig. 8.1. This shows that the magnetism of the system is strongly influenced by the exact ratio of Cr:Ni in the system which needs to be taken into consideration when interpreting the data presented in this chapter.

In this thesis, a systematic study of the magnetic and electrical properties was conducted on single crystals grown by the flux method. Samples with Co or Cu substituted for Ni or P for As were investigated in regards to the effect of substitution on the materials physical properties with focus on the ferromagnetic transition. The results were compared with those obtained for samples to which hydrostatic pressure was applied by way of a pressure cell.

8.1 Crystal Growth

CrNiAs crystallizes in a ZrNiAl structure. The room temperature lattice parameters are a=6.113-6.117 Å and c=3.654-3.659 Å [192, 202, 203].

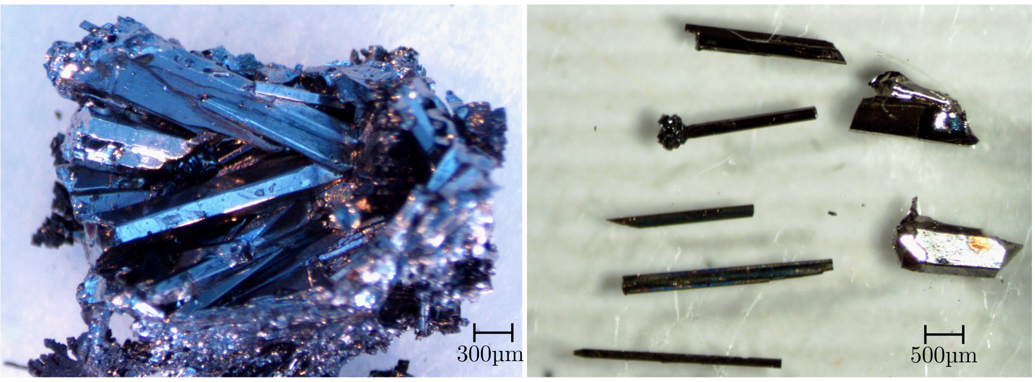

Figure 8.2: Single crystals as extracted from the crucible. Both needle shaped crystals and chunks can be found.

CrNiAs crystals are attempted to be grown using the same method as for CrRhAs discussed in the previous chapter. While CrRhAs was observed to grow exclusively in a needle shape, for this growth larger crystalline pieces can be found as well, allowing for measurements which can only be performed on samples of a certain size and thickness such as thermal expansion. Fig. 8.2

shows both types of crystals as extracted from the crucible after centrifugation. All remaining bismuth flux was removed using HCl.

Substitution was possible up to a certain degree by replacing some of the Ni with Cu or Co, or As with P. However, the doped crystals did not show the same stoichiometry as that used for the starting materials. The highest successful substitution percentages were 1% for Cu and 7% for Co and P. Even using a starting ratio as high as 1:1 for the substitution atom did not yield higher percentages in the resulting crystals.

8.2 Structural and Chemical Characterization

Despite the powder diffractogram shown in Fig 8.3 at first glance appearing to nicely match the literature data for the (111) phase, for almost all investigated crystals an excess of nickel was found in the EDX analysis, the absolute value of which depends on how the ratio is calculated, but was as high as 23 % which would translate into a stoichiometry of $(Cr_{0.4}Ni_{0.6})_2As$.

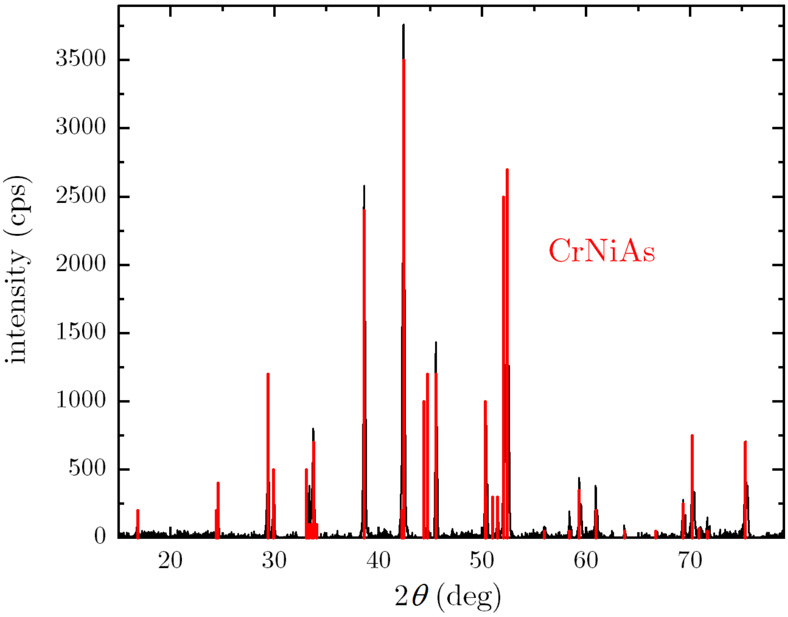

Figure 8.3: Powder diffractogram of several ground single crystals.

The data depicted in Tab. 8.1 was calculated by setting the sum of the elements as three, however, an excess of nickel was also found for calculation with either chromium or arsenic fixed as one atom per formula unit. Even though the detection of such a Ni excess might be due to some measurement errors, such a high deviation is rather unexpected, especially if compared to the measurements on CrRhAs performed under similar conditions. Thus, it appears possible that rather than growing CrNiAs, the obtained crystals are composed of $(Cr_{1-x}Ni_x)_2As$ with x >0.5 which could be confirmed in the following section by comparing the T_C values obtained for these crystals to those published in literature mentioned above. Further XRD measurements and structural refinement also indicated a stoichiometry of $(Cr_{0.46}Ni_{0.54})_2As$ [206] which would be consistent with the EDX as well as the measurements shown in the next section.

sample	Cr	Ni	As
# 1	0.82	1.19	0.99
# 2	1.02	1.15	0.83
# 3	0.94	1.20	0.86
# 4	0.83	1.23	0.94

Table 8.1: Stoichiometry of several crystals determined by EDX.

8.3 Physical Properties

Measurements of the field and temperature dependent magnetization as well as electrical transport were performed along different crystal axes for CrNiAs single crystals as well as Co, Cu or P substituted samples at ambient pressure as well as under hydrostatic pressure. The measurements at ambient pressure on pure samples as well as all measurements under hydrostatic pressure were performed and analysed by Dr. Bin Shen (University Augsburg) and are also published in [206, 207].

Field- and Temperature-dependent Magnetization

Field dependent magnetization was measured at 2 K, as shown in Fig. 8.4(a). Saturation is reached at around 0.1 T for the field applied parallel to the c axis and 0.8 T for the perpendicular case revealing c to be the easy axis and the system a rather soft magnet. The saturation magnetization is $\mu_{sat} = 0.9\,\mu_B$. Comparing this with the data published by Iwata et al. indicates a Ni concentration of $x \approx 0.55$.

The magnetic susceptibility was measured along and perpendicular to the c axis in field and zero field cool for a field of 0.1 T. At high temperatures, the susceptibility of both directions overlaps hinting at the magnetic exchange in the paramagnetic state being isotropic.

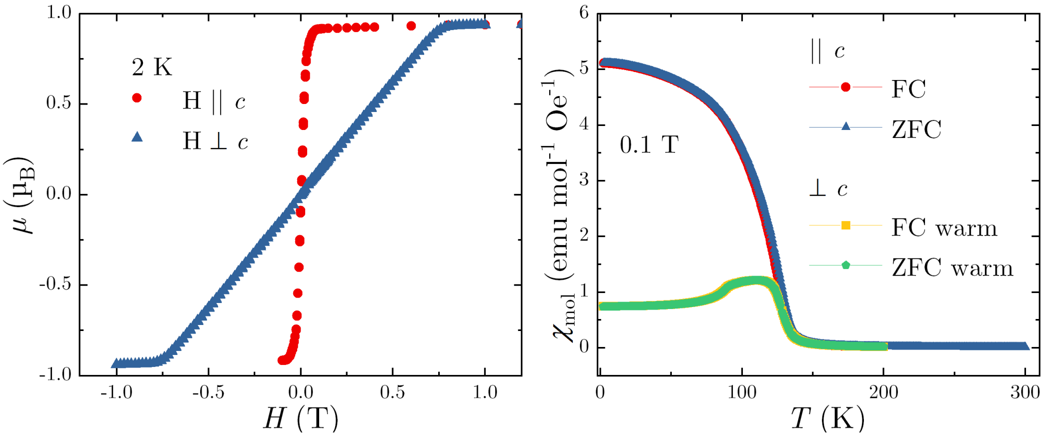

Figure 8.4: (a) Field dependent magnetization parallel and perpendicular to the c axis at 2K. (b) Field cooled (FC) and zero field cooled (ZFC) temperature dependent magnetization parallel and perpendicular to c at 0.1 T. [206]

A Curie Weiss fit for temperatures above 200 K yields an effective magnetic moment of $\mu_{\text{eff}} = 3.22\,\mu_{\text{B}}$ which is significantly larger than the saturation moment obtained from $\mu(H)$. The susceptibility increases rapidly, once a temperature below 135 K is reached which is in good agreement with the observed Curie Weiss temperature of $T_{\text{CW}} = 136\,\text{K}$. Comparing this once again with Iwata et al., this value is in good agreement with that reported for a Ni concentration of $x \approx 0.55$. For the parallel field, the susceptibility keeps increasing towards low temperatures before finally approaching saturation, whereas a maximum is reached at around 112 K for the perpendicular field. No difference can be seen between field cooled and zero field cooled measurements at the investigated fields, further confirming the system to behave like a soft magnet. At small fields, an additional kink at $T^* = 90\,\text{K}$ appears, the origin of which is still under investigation at the time of writing this thesis. Single crystals X-ray diffraction measurements performed below this temperature found neither additional reflections nor a significant peak splitting compared to higher temperatures. Thus, this transition cannot be explained by symmetry-breaking of the structural phase [206].

Electrical Transport

The electrical transport with the current applied parallel and perpendicular to the c axis for a single crystal is shown in Fig. 8.5(a). Compared to polycrystalline samples, the absolute values found here are an order of magnitude smaller which indicates higher sample quality.

A monotonic increase of the resistance towards low temperatures can be observed for the parallel case, while the perpendicular plot reaches a maximum at around 80 K before decreasing again towards low temperatures. Both

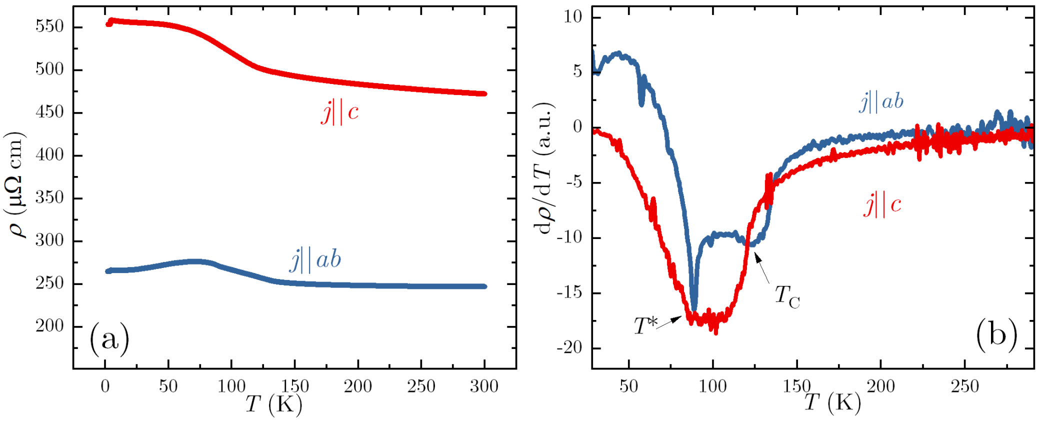

Figure 8.5: (a) Temperature dependent longitudinal electrical resistivity parallel and perpendicular to c. (b) Derivative of the resistivity showing the kinks at 135 and 90 K for the measurement perpendicular c [206].

directions show a kink at around 135 K and a second signature at 90 K which can be seen more clearly in the $\mathrm{d}\rho/\mathrm{d}T$ plot in Fig. 8.5(b). Data recorded during cooling perfectly overlaps with that taken during warm up. This absence of a hysteresis indicates that the two phase transition are second order. Furthermore, the resistivity is decreased in plane compared to the out of plane measurement.

Magnetoresistance and Anomalous Hall Effect

The magnetoresistance shown in Fig 8.6(a) shows positive values in the measured temperature range of 5-275 K. A kink at around 0.8 T can be clearly observed in the measurement at lowest temperature, but becomes increasingly less pronounced as the temperature approaches T_C. At higher fields, a quasi-linear behaviour can be observed at low temperatures, whereas above the ordering temperature, a parabolic field dependence is found. Looking at the Hall resistivity depicted in Fig. 8.6(b), below T_C anomalous Hall effect occurs. Fitting the high field data with $\rho_{xy} = \rho_{xy}^0 + \rho_{xy}^A = R_0 B + R_s \mu_0 M$ with R_0 and R_s the normal and anomalous Hall resistivity coefficients, as is customary for ferromagnets, the anomalous contribution ρ_{xy}^A can be extracted. Looking at the temperature dependence of the anomalous contribution depicted in Fig. 8.6(c), a strong increase for temperatures approaching T_C can be observed followed by saturation being reached at around 100 K which corresponds to the temperature at which the susceptibility also begins to saturate. Plotting ρ_{xy}^A over ρ_{xx} as shown in Fig. 8.6(d) can be used to identify the origin of ρ_{xy}^0. Here, a linear dependence is found which indicates skew scattering to be the main origin of the anomalous Hall effect in this system [208].

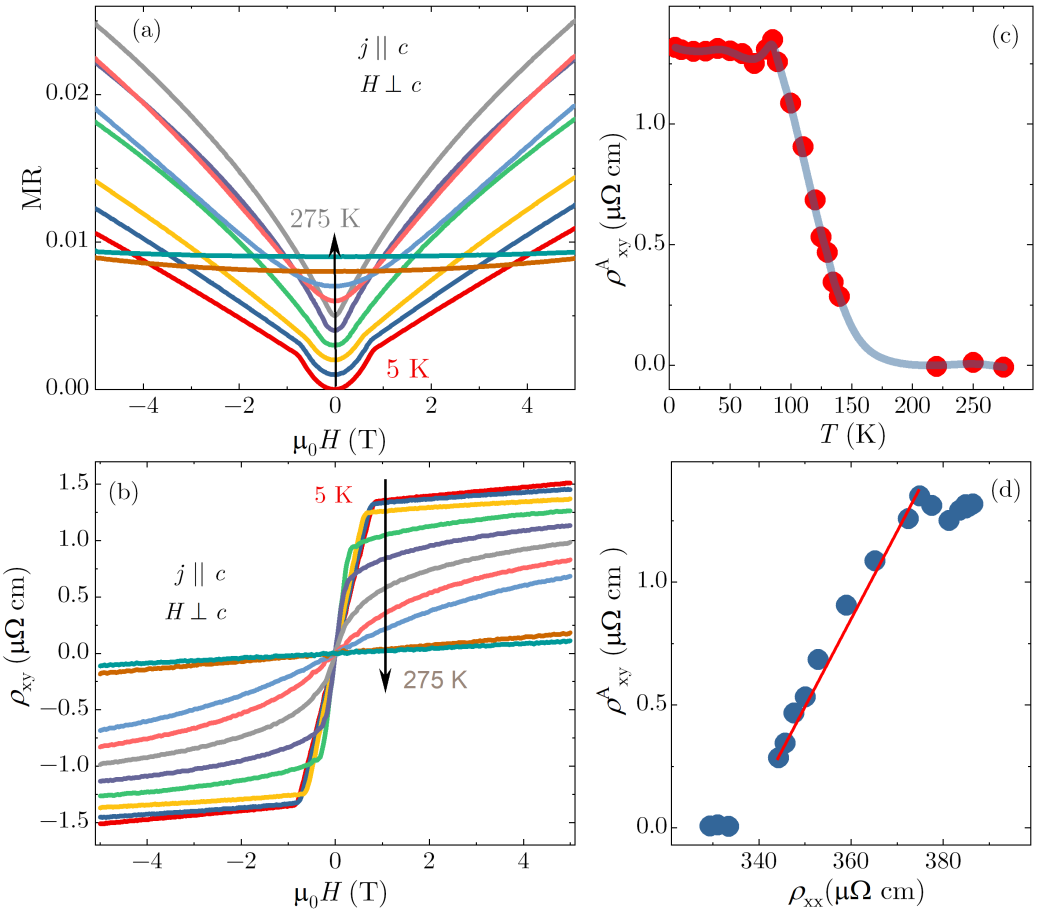

Figure 8.6: Magnetoresistance (a) and Hall resistivity (b) of CrNiAs in the temperature range of 5-275 K with the magnetic field applied perpendicular and the current applied parallel to c. From this the anomalous Hall resistivity ρ_{xy}^{A} vs T shown in (c) can be obtained. Plotting ρ_{xy}^{A} vs ρ_{xx} shown in (d) reveals a linear relation [206].

Impact of Substitution

For this section, the focus is put on the magnetic susceptibility and longitudinal electrical resistivity since both are quickly and easily accessible and the shift in transition temperature can be clearly observed. Three different substitutions were attempted here: $\mathrm{CrNi}_{1-x}\mathrm{Co}_x\mathrm{As}$, $\mathrm{CrNi}_{1-x}\mathrm{Cu}_x\mathrm{As}$ and $\mathrm{CrNiAs}_{1-x}\mathrm{P}_x$. While low Co concentrations did not yield any significant change in transition temperature, at higher concentrations another transition at lower temperatures was found, thus making Co substitution not a suitable candidate for suppressing the ordering. For Cu, it was not possible to substitute more than 1% of Ni despite weighing in as much as 50% in the starting materials. For this doped sample, no significant change in transition temperature was observed either.

Temperature dependent susceptibility measurements for both substitutions are shown in Fig. 8.7.

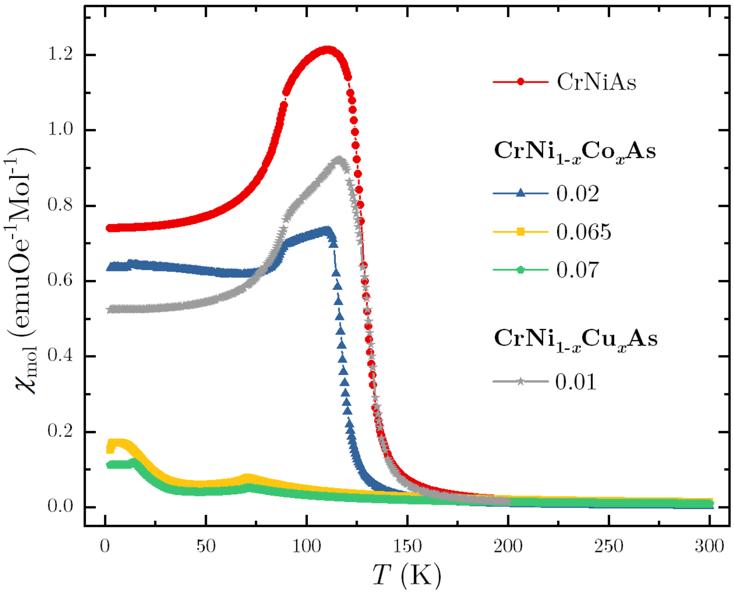

Figure 8.7: Temperature dependent susceptibility of copper or cobalt doped CrNiAs. For low Co or Cu substitution no significant change in T_{C} can be observed, while for the first another transition appears for higher substitution levels. A higher Cu substitution could not be achieved.

Thus, this section will focus on the substitution of arsenic with phosphorus. Several samples were prepared with nominal phosphorus contents in the range of x=0.005-0.6, however, no crystals with more than 7 % phosphorus substitution were found and the following measurements were limited to this substitution range.

Both magnetic susceptibility and electrical resistivity, depicted in Fig. 8.8, show an initial decrease of the ferromagnetic transition temperature with a minimum being reached at around $x = 0.033$. For higher phosphorus content, the transition temperature was shifted to higher values again, though still lower than that of the undoped compound. For the samples with more than 4 % substitution, the signature at T^* can no longer be clearly identified.

An overview over the change in transition temperatures T_C and T^* determined from $\mathrm{d}(\chi \cdot T)/\mathrm{d}T$ and $\mathrm{d}R/\mathrm{d}T$, and T_{CW} determined from fitting the high temperature magnetic susceptibility is shown in Fig. 8.9. T_{C} values extracted from susceptibility and resistivity are in good agreement and T_{CW} from fitting the high temperature susceptibility also yields similar values.

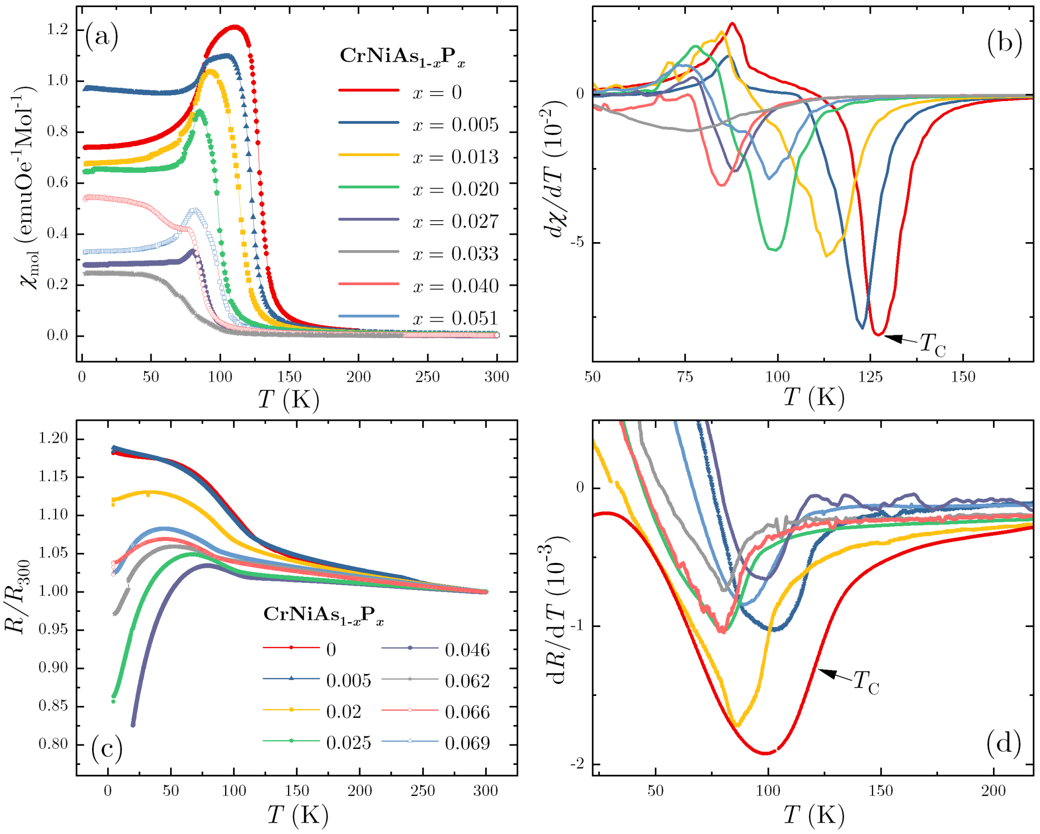

Figure 8.8: (a) Temperature dependent magnetic susceptibility and $d(\chi \cdot T)/dT$ (b) for several P-doped CrNiAs single crystals. As also observed in the electrical resistance, the transition temperature, marked by a minimum in $d(\chi \cdot T)/dT$, first shifts to lower temperatures with increasing phosphorus content, before increasing again for the phosphorus richest samples. (c) Temperature dependent longitudinal resistance plotted as R/R_{300} and its derivative (d) for several single crystals of CrNiAs with varying amounts of phosphorus substitution on the arsenic side. The transition, marked by a kink in $R(T)$, first shifts to lower temperatures with increasing phosphorus content, before increasing again for the phosphorus richest samples.

CrNiP was reported to be an itinerant ferromagnet with a Curie temperature of $T_C = 146\,\mathrm{K}$ [209, 210]. The reported effective moment is $\mu_{sat}=0.8\,\mu_B$ [211]. X-ray powder diffraction measurements of polycrystalline CrNiP revealed a Co_2P-type crystal structure with the space group Pnma with lattice parameters $a = 5.7965(1)\,\text{Å}$, $b = 3.5337(1)\,\text{Å}$ and $c = 6.8123\,\text{Å}$ [211]. However, a second phase in the amount of close to 10 wt% was detected and attributed to space group $P\overline{6}2m$ which is that reported for CrNiAs. A different paper also reported this space group with the lattice parameters given as $a = 5.84000\,\text{Å}$ and $c = 3.51400\,\text{Å}$ [212] which is roughly 5% smaller than those reported for

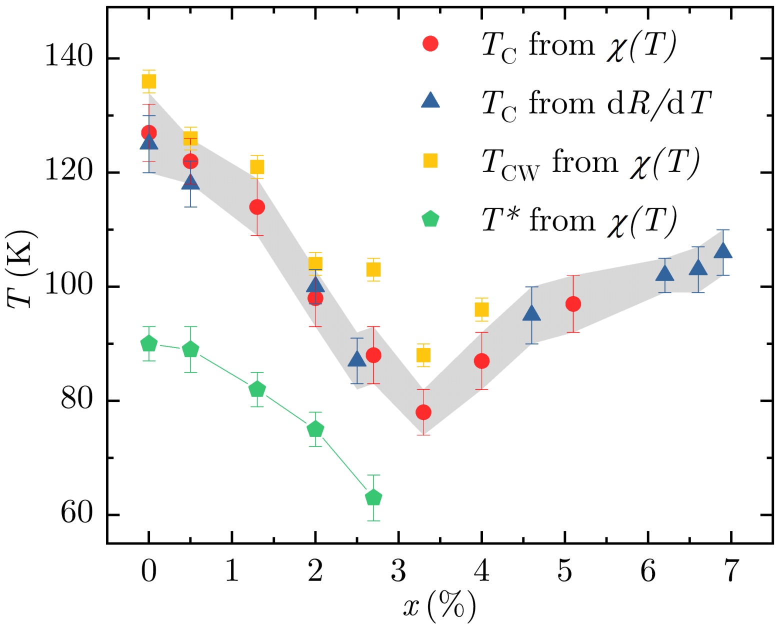

Figure 8.9: Transition temperatures determined from magnetic susceptibility and resistivity plotted against the samples phosphorus content. T_C reaches a minimum at 3.3 % P substitution.

CrNiAs.

For samples with different crystal structures, Vegard's law can not be employed to estimate the change in lattice parameters for the doped system. However, a powder diffractogram revealed similar peaks for the doped compared to the undoped sample. Furthermore, similar magnetic and electrical behaviour was observed for both. Thus, it is likely that the doped samples show the same crystal structure as reported for CrNiAs. Since the individual crystals are rather small, several crystals with slightly varying phosphorus content determined by EDX were ground into powder for an XRD measurement. Unfortunately, no powder measurements of the substituted samples of high enough quality to reliably determine the lattice parameters are available due to high noise, additional peaks due to flux inclusions or lack of material. It might be interesting to further investigate the change in lattice parameters by single crystal x-ray diffraction and make some efforts to investigate the crystal structure for different P concentrations in the future in order to gain insight into the initial decrease and following increase of T_C with increasing x.

As an alternative means to quantify the effect of the substitution, the change in transition temperature for the doped sample with the smallest T_C determined from $M(T)$ under hydrostatic pressure in Fig. 8.10(a) is compared to that achieved by the application of hydrostatic pressure on the pure compound [207]. Here, measurements under hydrostatic pressure up to 6.35 GPa were conducted on the $\mathrm{CrNiAs_{0.967}P_{0.033}}$ sample. Plotting the data in a p-T-diagram, as can be seen in Fig. 8.10(b), revealed a similar slope for both compounds with the data for the $\mathrm{CrNiAs_{0.967}P_{0.033}}$ sample shifted to lower temperatures compared to CrNiAs at equivalent pressures.

Comparing both datasets shows that a shift of Δp=4.5 GPa results in a good overlap of the data of both samples. This value should however not be considered as a direct conversion of the substitution into chemical pressure, since it was shown that other factors such as the Cr:Ni ratio strongly impact the ferromagnetic transition as well and it cannot be definitively stated that the observed effect is exclusively carried by the P substitution.

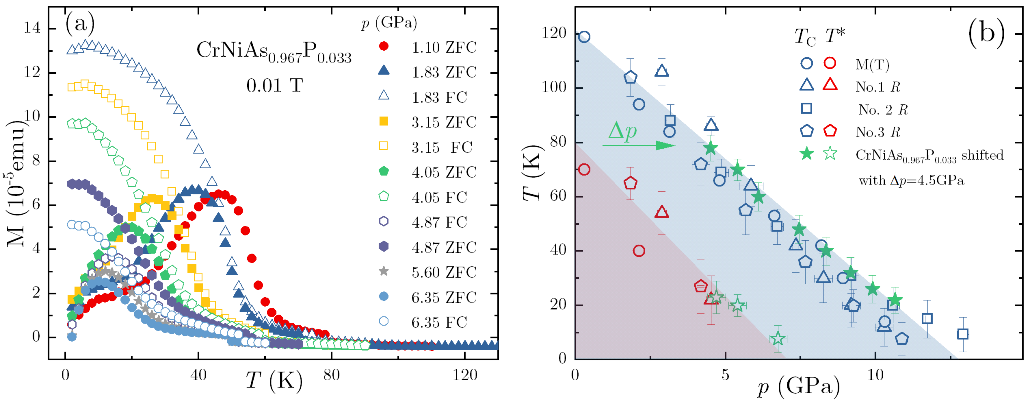

Figure 8.10: (a) Temperature dependent magnetization of a $\mathrm{CrNiAs_{0.967}P_{0.033}}$ single crystal for increasing hydrostatic pressure applied perpendicular to the c axis. The ferromagnetic transition at T_C continues to be shifted towards lower temperatures with increasing pressure. (b) p-T-phase diagram for CrNiAs [207] and $\mathrm{CrNiAs_{0.967}P_{0.033}}$. The data for the doped samples was shifted by Δp=4.5 GPa.

8.4 Summary and Discussion

Single crystals of CrNiAs, $\mathrm{CrNi_{1-x}Co_xAs}$, $\mathrm{CrNi_{1-x}Cu_xAs}$ and $\mathrm{CrNiAs_{1-x}P_x}$ were grown using the same flux growth method as described for CrRhAs. Both needle shaped crystals and larger crystals were obtained this way. Magnetization and electrical transport measurements showed a ferromagnetic transition temperature of T_C=135 K which is significantly lower than the value reported for polycrystalline samples. A second kink was observed at T^*=90 K the origin of which is still under investigation. Comparing both T_C and the obtained saturation magnetization of μ_sat=0.9 μ_B with those obtained for a series $\mathrm{(Cr_{1-x}Ni_x)_2As}$ with x=0.425-0.6 by Iwata et al. [201] indicates a Ni concentration of about x =0.55 for the crystals grown in this thesis which would also explain the enhanced Ni:Cr ratio detected by EDX.

Furthermore, CrNiAs shows a strong anomalous Hall effect below T_C the origin of which can likely be attributed to skew scattering.

Substitution of As with P leads to a reduction of T_C up to a P content of 3.3 % where a minimum value of 78 K was reached. For higher P percentages T_C was increased again. Comparison with measurements performed under hydrostatic pressure revealed that this minimum in T_C would correspond to a shift in pressure of Δp
$approx$4.5 GPa.

A possible explanation for this observed minimum would be an effect similar to that observed in the pyrochlore $(Eu_{1-x}Bi_x)_2Ir_2O_7$, where, despite the larger lattice parameters of $Bi_2Ir_2O_7$ compared to those of $Eu_2Ir_2O_7$, a minimum in the lattice parameters deviating from the expected Vegards law is detected at x=0.03 attributed to an anomalous lattice contraction [213] which would correspond to an increased chemical pressure. Similar behaviour is also observed in La-doped Sr_2IrO_4 [214], $Sr_3Ir_2O_7$ [215] or $SrTiO_3$ [216]. In these cases, the anomalous contraction is attributed to a change in carrier doping by replacing Sr^{3+} with La^{3+} which can, however, not be applied to $CrNiAs_{1-x}P_x$ or $(Eu_{1-x}Bi_x)_2Ir_2O_7$ since for both materials the substitution atoms are isovalent. For $(Eu_{1-x}Bi_x)_2Ir_2O_7$, the anomalous lattice contraction was thus suggested to arise from an enhanced hybridization of (Ir)5d-(Bi)6s/6p which results in th 6s/6p electrons of Bi contribution to the density of states at the Fermi level [217].

For CrNiAs, the ferromagnetic transition was shown to be fully suppressed only at a significantly higher hydrostatic pressure of ∼13 GPa. Full suppression of the ferromagnetic ordering by P substitution thus seems highly unlikely, especially considering that CrNiP itself shows a ferromagnetic transition at 146 K. Still, it might be interesting to look further into the origin of the substitution percentage dependence of the structural development of $CrNiAs_{1-x}P_x$ and the corresponding change in T_C.

However, since it has been shown that the transition temperature is strongly influenced by the exact ratio of Cr:Ni, one cannot say definitively if P substitution and hydrostatic pressure affect the ferromagnetic transition in the same way and this comparison should be considered with caution.

In the future, it might thus be interesting to further study the homogeneity region for different Ni concentrations and the dependence of the physical properties on the Ni:Cr ratio in $(Cr_{1-x}Ni_x)_2As$. While CrRhAs was shown to only grow within a rather narrow stoichiometry window using the flux growth method described in this chapter, no similar investigation was conducted for CrNiAs yet. Thus, it might be possible to influence the Cr:Ni ratio in the single crystals obtained by flux growth by changing the stoichiometry of the starting materials. However, this is beyond the scope of this work and shall be left to future research.

9 Summary and Outlook

In this thesis, a combined FIB-SEM set up was utilized in order to investigate several members of the honeycomb Kitaev magnets, including α-$RuCl_3$, Na_2IrO_3 and β-Li_2IrO_3 in chapter 4, 5 and 6, as well as the kagome magnetic metals CrRhAs and CrNiAs in chapter 7 and 8. Here, FIB microstructuring was used to access small structures on the micrometre scale or prepare micrometre thick devices with sufficiently larger surface area for XRD measurements as well as allow for the contacting of small samples in a Hall geometry.

This thesis began with an introduction into the theoretical background, including magnetism and electrical transport in chapter 2, followed by a description of the experimental methods in chapter 3 including x-ray diffraction, energy dispersive x-ray spectroscopy and Laue back scattering as well as FIB-SEM microstructuring and the basics of magnetization and electrical transport measurement.

In chapter 4, an in depth analysis of the structure and electrical transport behaviour of Na_2IrO_3 which grows as platelet shaped crystals of several tens of micrometers thickness, was discussed. Here, the existence of structural domains which are rotated around the c axis by $\pm 120°$ towards each other was uncovered. EDX analysis showed a varying degree of sodium deficiency in these structural domain walls with Na being reduced down to as little as $\sim 2/3$ of its original value in some samples. Direct contacting of such domain walls for longitudinal as well as Hall resistivity was possible utilizing FIB structuring along with the deposition of GIS platinum. A correspondence between Na deficiency and electrical transport behaviour was observed in so far as that the absolute resistivity values decrease with increasing Na deficiency. The two samples with lowest sodium content on the domain walls even showed metallic behaviour down to the lowest measured temperature of 2 K suggesting that a crossing of the metal-to-insulator transition has occurred in these samples. While the longitudinal magnetoresistance shows a steep increase at low fields indicating the occurrence of weak antilocalization, the Hall resistance of such a metallic structural domain wall shows purely linear behaviour and thus no indication of ferromagnetic ordering.

Chapter 5 discussed the thermal degradation of single crystalline α-$RuCl_3$ and its impact on the low temperature physical properties. Heat treatments at temperatures above 350°C in sealed ampoules or argon flow lead to the formation of RuO_2, not only on the surface but also a significant way towards the inside of the crystal. The formation of RuO_2 was confirmed by powder x-ray diffraction of porous flakes extracted from the annealed crystals surface and the stoichiometry of the annealed samples quantified by EDX analysis to be as high as 75 at% Ru and 25 at% Cl on the crystal surface compared to the expected ratio of 1:3 for pristine samples. The low temperature heat capacity of the annealed crystals showed an increase towards low temperatures which could be explained very well by combining the heat capacities of both $RuCl_3$ and RuO_2 using the mass of RuO_2 as a free fit parameter. RuO_2 mass fractions of as much as 20 % were found for the heat treated samples. Comparison with the RuO_2 fraction calculated from mass loss due to annealing determined by scale showed similar results. Analogously fitting the heat capacity of the pristine crystals indicated the presence of a small fraction of RuO_2 in the range of 0.9-2 % even before annealing. At first glance, the magnetic susceptibility of heat treated samples appeared to be significantly decreased compared to the pristine samples. However, correcting the mass by the RuO_2 fraction determined from the mass loss during annealing, and thus adjusting for the significantly smaller susceptibility of RuO_2, results in a close overlap of both plots. The electrical resistivity was observed to decrease by several orders of magnitude after heat treatment at 120°C in air. Thus, a significant influence of annealing leading to the formation of RuO_2 on the surface and inside of initially pristine single crystals of α-$RuCl_3$ on the low temperature heat capacity as well as magnetic susceptibility and electrical transport could be observed and reproduced for several samples. In the future, investigations into the influence of the inclusion of even a small RuO_2 fraction in pristine samples on other measurements such as low temperature thermal transport and Hall effect could give further insight into the physics behind this complex material.

FIB microsectioning was utilized for thinning a β-Li_2IrO_3 single crystal down to ~1 µm in chapter 6 by attaching it to an STO substrate, polishing and then cutting with the crystal surface aligned parallel to the FIB beam. Preliminary x-ray diffraction measurements comparing a bulk and a FIB structured crystal showed that both the electronic structure and the magnetic ordering remain intact for the FIB structured sample. In the future, further experiments looking into the dynamics of the systems magnetic and structural ordering parameters, such as dissipative pump-probe spectroscopy, will be conducted on a sample prepared in the described fashion.

Chapter 7 tells of the first successful growth of needle shaped CrRhAs single crystals of several millimetres length and a thickness of up to 200 µm by flux growth. Heat capacity, electrical transport and magnetic susceptibility were measured and revealed a Néel temperature of T_N=148 K which is somewhat smaller than the value reported previously for polycrystals. Both Curie temperature $T_\mathrm{C} = -595\,\mathrm{K}$ and effective moment μ_eff=4µ$_\mathrm{B}$ are in good agreement with the theoretical prediction. However, despite the report of an unusual magnetic Hamiltonian and a consequential theoretical prediction of exotic behaviour, a purely linear Hall resistance was found with no signs of an anomalous contribution. Along with the cubic magnetoresistance, the material thus appears to behave like a typical metal with similar magnetoresistance having been previously observed in other antiferromagnets. Since both resistivity and Hall measurements could only be successfully performed along the c axis, future measurements within the ab plane might provide additional information on this material.

Applying the same crystal growth method as for CrRhAs, the synthesis and characterization of CrNiAs as well as $\mathrm{CrNi}_{1-x}\mathrm{Co}_x\mathrm{As}$, $\mathrm{CrNi}_{1-x}\mathrm{Cu}_x\mathrm{As}$ and $\mathrm{CrNiAs}_{1-x}\mathrm{P}_x$ was attempted in chapter 8 revealing a T_C of 135 K for the pure compound which could be shifted to lower temperatures upon applying hydrostatic pressure and was completely suppressed at around 13 GPa. Comparison of T_C and saturation magnetization of the pure compound with a study done on $(\mathrm{Cr}_{1-x}\mathrm{Ni}_x)_2\mathrm{As}$ indicates a Ni excess of $x = 0.55$ which would also be in good agreement with the Cr:Ni ratio determined by EDX and XRD structure refinement. Thus, the obtained single crystals appear not to be the 1:1:1 phase, but rather $\mathrm{Cr}_{0.9}\mathrm{Ni}_{1.1}\mathrm{As}$. Furthermore, below T_C an anomalous Hall contribution originating from skew scattering could be detected. Looking at the influence of substitution on the materials properties, it could be shown that, while Cu or Co substitution did not yield the desired effect, for $\mathrm{CrNiAs}_{1-x}\mathrm{P}_x$ a minimum in T_C of 78 K is reached for a P content of 3.3% which would correspond to a $\Delta p \simeq 4.5$ GPa compared to pure CrNiAs under hydrostatic pressure. For higher substitution, the ferromagnetic transition shifts to higher temperatures again. Since the ferromagnetic transition has been shown to be strongly influenced by the Cr:Ni ratio in the single crystals as well, it cannot be definitively stated whether this reduction is purely attributed to the substituted phosphorus. It might thus be interesting to further investigate the origin of the minimum in T_C in the $\mathrm{CrNiAs}_{1-x}\mathrm{P}_x$ samples or try substitution with other elements in order to suppress the ferromagnetic transition as well as look further into the dependence of the physical properties on the Cr:Ni ratio. Furthermore, it might be interesting to further study the homogeneity region for different Ni concentrations and influence of the Ni:Cr ratio on the materials physical properties. CrRhAs was shown to only grow within a rather narrow stoichiometry window, but no similar investigation was conducted for $(\mathrm{Cr}_{1-x}\mathrm{Ni}_x)_2\mathrm{As}$ yet. It might thus be possible to influence the Cr:Ni ratio in the single crystals obtained by flux growth by changing the stoichiometry of the starting materials.

Overall, this thesis showed several possibilities for the application of FIB microstructuring from contacting for electrical transport measurements of micrometer structures to large scale thinning for measurements requiring thin samples of materials which cannot be grown as high quality thin films revealing new information on previously studied honeycomb Kitaev magnets and kagome magnetic metals. The techniques used here for honeycomb Kitaev magnets and kagome magnetic metals can potentially be - and already are - applied to many more systems for which only small samples are available or precise contacting of microstructures is desirable.

Bibliography

[1] A. Kitaev. Anyons in an exactly solved model and beyond. *Annals of Physics*, 321(1):2–111, 2006.

[2] Y. Kasahara, T. Ohnishi, Y. Mizukami, O. Tanaka, Sixiao Ma, K. Sugii, N. Kurita, H. Tanaka, J. Nasu, Y. Motome, T. Shibauchi, and Y. Matsuda. Majorana quantization and half-integer thermal quantum Hall effect in a Kitaev spin liquid. *Nature*, 559:227, 2018.

[3] A. Banerjee, P. Lampen-Kelley, J. Knolle, C. Balz, A.A. Aczel, B. Winn, Y. Liu, D. Pajerowski, J. Yan, C.A. Bridges, et al. Excitations in the field-induced quantum spin liquid state of α-RuCl$_3$. *npj Quantum Materials*, 3(1):1–7, 2018.

[4] M.L. Kiesel, C. Platt, and R. Thomale. Unconventional fermi surface instabilities in the kagome hubbard model. *Physical review letters*, 110(12):126405, 2013.

[5] S. Okamoto, N. Mohanta, E. Dagotto, and D.N. Sheng. Topological flat bands in a kagome lattice multiorbital system. *Communications Physics*, 5(1):198, 2022.

[6] M. Kang, L. Ye, S. Fang, J.-S. You, A. Levitan, M. Han, J.I. Facio, C. Jozwiak, A. Bostwick, E. Rotenberg, et al. Dirac fermions and flat bands in the ideal kagome metal fesn. *Nature materials*, 19(2):163–169, 2020.

[7] L. Balents. Spin liquids in frustrated magnets. *nature*, 464(7286):199–208, 2010.

[8] L. Savary and L. Balents. Quantum spin liquids: a review. *Reports on Progress in Physics*, 80(1):016502, 2016.

[9] Y. Zhou, K. Kanoda, and T.-K. Ng. Quantum spin liquid states. *Reviews of Modern Physics*, 89(2):025003, 2017.

[10] S. Manni, S. Choi, I.I. Mazin, R. Coldea, M. Altmeyer, H.O. Jeschke, R. Valenti, and P. Gegenwart. Effect of isoelectronic doping on the honeycomb-lattice iridate A$_2$IrO$_3$. *Physical Review B*, 89(24):245113, 2014.

[11] G.B. Halász, J.T. Chalker, and R. Moessner. Doping a topological quantum spin liquid: Slow holes in the Kitaev honeycomb model. *Physical Review B*, 90(3):035145, 2014.

[12] V. Hermann, J. Ebad-Allah, F. Freund, I.M. Pietsch, A. Jesche, A.A. Tsirlin, J. Deisenhofer, M. Hanfland, P. Gegenwart, and C.A. Kuntscher. High-pressure versus isoelectronic doping effect on the honeycomb iridate Na_2IrO_3. *Physical Review B*, 96(19):195137, 2017.

[13] Z.A. Kelly, M.J. Gallagher, and T.M. McQueen. Electron doping a kagome spin liquid. *Physical Review X*, 6(4):041007, 2016.

[14] J. Park, B. Cho, C.-Y. You, and K. Park. Magnetic anisotropy and magnetic phase diagram of a kagome antiferromagnet $Fe_{1-x}Co_xSn$. *Journal of Alloys and Compounds*, 976:173003, 2024.

[15] E. Ruska. The development of the electron microscope and of electron microscopy. *Reviews of modern physics*, 59(3):627, 1987.

[16] V.E. Krohn and G.R. Ringo. Ion source of high brightness using liquid metal. *Applied Physics Letters*, 27(9):479–481, 1975.

[17] R.L. Seliger. Submicron imaging of a liquid metal gallium source. *Ultramicroscopy*, 4(3):374, 1979.

[18] L.W. Swanson. Use of the liquid metal ion source for focused beam applications. *Applied surface science*, 76:80–88, 1994.

[19] L. Bischoff, P. Mazarov, L. Bruchhaus, and J. Gierak. Liquid metal alloy ion sources—an alternative for focussed ion beam technology. *Applied Physics Reviews*, 3(2), 2016.

[20] A.N. Zorzos and P.C. Lozano. The use of ionic liquid ion sources in focused ion beam applications. *Journal of Vacuum Science & Technology B: Microelectronics and Nanometer Structures Processing, Measurement, and Phenomena*, 26(6):2097–2102, 2008.

[21] T.P. Fedkiw and P.C. Lozano. Development and characterization of an iodine field emission ion source for focused ion beam applications. *Journal of Vacuum Science & Technology B: Microelectronics and Nanometer Structures Processing, Measurement, and Phenomena*, 27(6):2648–2653, 2009.

[22] N.S. Smith, W.P. Skoczylas, S.M. Kellogg, D.E. Kinion, P.P. Tesch, O. Sutherland, A. Aanesland, and R.W. Boswell. High brightness

inductively coupled plasma source for high current focused ion beam applications. *Journal of Vacuum Science & Technology B: Microelectronics and Nanometer Structures Processing, Measurement, and Phenomena*, 24(6):2902–2906, 2006.

[23] B. Van Leer and M. Dutka. Latest developments in multiple ion species plasma fib technology. *Microscopy and Microanalysis*, 25(S2):570–571, 2019.

[24] K. Höflich, G. Hobler, F.I. Allen, T. Wirtz, G. Rius, L. McElwee-White, A.V. Krasheninnikov, M. Schmidt, I. Utke, N. Klingner, et al. Roadmap for focused ion beam technologies. *Applied Physics Reviews*, 10(4), 2023.

[25] F.A. Stevie[1], L.A. Giannuzzi, and B.I. Prenitzer. The focused ion beam instrument. *Introduction to Focused Ion Beams: Instrumentation, Theory, Techniques and Practice*, page 1, 2004.

[26] D. Verkleij. The use of the focused ion beam in failure analysis. *Microelectronics reliability*, 38(6-8):869–876, 1998.

[27] A.A. Volinsky, L. Rice, W. Qin, and N.D. Theodore. FIB failure analysis of memory arrays. *Microelectronic Engineering*, 75(1):3–11, 2004.

[28] Y. Chen and X. Zhang. Focused ion beam technology and application in failure analysis. In *2010 11th International Conference on Electronic Packaging Technology & High Density Packaging*, pages 957–960. IEEE, 2010.

[29] T. Ishitani and T. Yaguchi. Cross-sectional sample preparation by focused ion beam: A review of ion-sample interaction. *Microscopy research and technique*, 35(4):320–333, 1996.

[30] J.Y. Liu, J. Yu, J.L. Ning, H.M. Yi, L. Miao, L.J. Min, Y.F. Zhao, W. Ning, K.A. Lopez, Y.L. Zhu, et al. Spin-valley locking and bulk quantum Hall effect in a noncentrosymmetric Dirac semimetal $BaMnSb_2$. *Nature communications*, 12(1):4062, 2021.

[31] M. Gabureac, L. Bernau, I. Utke, and G. Boero. Granular co–c nano-hall sensors by focused-beam-induced deposition. *Nanotechnology*, 21(11):115503, 2010.

[32] A. Sandhu, K. Kurosawa, M. Dede, and A. Oral. 50 nm hall sensors for room temperature scanning hall probe microscopy. *Japanese journal of applied physics*, 43(2R):777, 2004.

[33] P.J.W. Moll, B. Zeng, L. Balicas, S. Galeski, F.F. Balakirev, E.D. Bauer, and F. Ronning. Field-induced density wave in the heavy-fermion compound CeRhIn_5. *Nature Communications*, 6(1):6663, 2015.

[34] R.W. Simon, J.B. Bulman, J.F. Burch, S.B. Coons, K.P. Daly, W.D. Dozier, R. Hu, A.E. Lee, J.A. Luine, C.E. Platt, et al. Engineered hts microbridges. *IEEE transactions on magnetics*, 27(2):3209–3214, 1991.

[35] S.A. Cybart, E.Y. Cho, T.J. Wong, B.H. Wehlin, M.K. Ma, C. Huynh, and R.C. Dynes. Nano Josephson superconducting tunnel junctions in $\mathrm{YBa}_2\mathrm{Cu}_3\mathrm{O}_{7-\delta}$ directly patterned with a focused helium ion beam. *Nature nanotechnology*, 10(7):598–602, 2015.

[36] A.V. Krasheninnikov and K. Nordlund. Ion and electron irradiation-induced effects in nanostructured materials. *Journal of applied physics*, 107(7), 2010.

[37] D.S. Fox, Y. Zhou, P. Maguire, A. O'Neill, C. O'Coileain, R. Gatensby, A.M. Glushenkov, T. Tao, G.S. Duesberg, I.V. Shvets, et al. Nanopatterning and electrical tuning of MoS_2 layers with a subnanometer helium ion beam. *Nano letters*, 15(8):5307–5313, 2015.

[38] T. Oguchi, K. Terakura, and A.R. Williams. Band theory of the magnetic interaction in mno, mns, and nio. *Physical Review B*, 28(11):6443, 1983.

[39] A. Avella, F. Mancini, et al. *Strongly Correlated Systems*. Springer, 2012.

[40] D. Vollhardt. Elektronische Korrelationen und Magnetismus. 1996.

[41] R. Gross and A. Marx. *Festkörperphysik*. De Gruyter Oldenbourg, München, 2014.

[42] S. Blundell. *Magnetism in condensed matter*. OUP Oxford, 2001.

[43] S. Maekawa, T. Tohyama, S.E. Barnes, S. Ishihara, W. Koshibae, and G. Khaliullin. *Physics of transition metal oxides*, volume 144. Springer Science & Business Media, 2013.

[44] R.T. Scalettar. An introduction to the hubbard hamiltonian. *quantum materials: experiments and theory*, 6, 2016.

[45] M. Imada, A. Fujimori, and Y. Tokura. Metal-insulator transitions. *Reviews of modern physics*, 70(4):1039, 1998.

[46] S. Hunklinger. Festkörperphysik. In *Festkörperphysik*. De Gruyter Oldenbourg, 2017.

[47] L.H. Thomas. I. the kinematics of an electron with an axis. *The London, Edinburgh, and Dublin Philosophical Magazine and Journal of Science*, 3(13):1–22, 1927.

[48] A.V. Narlikar. *Superconductors.* Oxford University Press, 2014.

[49] G. Toulouse. The frustration model. In *Modern Trends in the Theory of Condensed Matter: Proceedings of the XVI Karpacz Winter School of Theoretical Physics, February 19–March 3, 1979 Karpacz, Poland*, pages 195–203. Springer, 2008.

[50] P. Schiffer. Magnetic frustration squeezed out. *Nature*, 420(6911):35–38, 2002.

[51] A.P. Ramirez. Strongly geometrically frustrated magnets. *Annual Review of Materials Science*, 24(1):453–480, 1994.

[52] K.H.J. Buschow. *Handbook of magnetic materials.* Elsevier, 2003.

[53] R. Moessner and A.P. Ramirez. Geometrical frustration. *Physics Today*, 59(2):24–29, 2006.

[54] K.P. Schmidt and S. Trebst. Topologische Spinflüssigkeiten. *Physik Journal*, 14(4), 2015.

[55] G. Mendonça, R. Lapa, J.R. De Sousa, M.A. Neto, K. Majumdar, and T. Datta. The ground state phase diagram of the quantum J_1-J_2 spin-1/2 Heisenberg antiferromagnet on an anisotropic square lattice. *Journal of Statistical Mechanics: Theory and Experiment*, 2010(06):P06022, 2010.

[56] W. Witczak-Krempa, G. Chen, and L. Kim, Y.B.and Balents. Correlated quantum phenomena in the strong spin-orbit regime. *Annu. Rev. Condens. Matter Phys.*, 5(1):57–82, 2014.

[57] S.M. Winter, A.A. Tsirlin, M. Daghofer, J. van den Brink, Y. Singh, P. Gegenwart, and R. Valentí. Models and materials for generalized Kitaev magnetism. *Journal of Physics: Condensed Matter*, 29(49):493002, 2017.

[58] A.Y. Kitaev. Fault-tolerant quantum computation by anyons. *Annals of Physics*, 303(1):2–30, 2003.

[59] G. Jackeli and G. Khaliullin. Mott insulators in the strong spin-orbit coupling limit: from heisenberg to a quantum compass and kitaev models. *Physical review letters*, 102(1):017205, 2009.

[60] J. Chaloupka, G. Jackeli, and G. Khaliullin. Kitaev-Heisenberg model on a honeycomb lattice: possible exotic phases in iridium oxides A_2IrO_3. *Physical review letters*, 105(2):027204, 2010.

[61] B. J. Kim, Hosub Jin, S. J. Moon, J.-Y. Kim, B.-G. Park, C. S. Leem, Jaejun Yu, T. W. Noh, C. Kim, S.-J. Oh, J.-H. Park, V. Durairaj, G. Cao, and E. Rotenberg. Novel $J_{\mathrm{eff}} = 1/2$ Mott State Induced by Relativistic Spin-Orbit Coupling in Sr_2IrO_4. *Phys. Rev. Lett.*, 101:076402, Aug 2008.

[62] T. Moriya. Anisotropic superexchange interaction and weak ferromagnetism. *Physical review*, 120(1):91, 1960.

[63] J. Chaloupka, G. Jackeli, and G. Khaliullin. Zigzag magnetic order in the iridium oxide Na_2IrO_3. *Physical review letters*, 110(9):097204, 2013.

[64] J.G. Rau and H.-Y. Kee. Trigonal distortion in the honeycomb iridates: Proximity of zigzag and spiral phases in Na_2IrO_3. *arXiv preprint arXiv:1408.4811*, 2014.

[65] J. Chaloupka and G. Khaliullin. Hidden symmetries of the extended Kitaev-Heisenberg model: Implications for the honeycomb-lattice iridates A_2IrO_3. *Physical Review B*, 92(2):024413, 2015.

[66] L. Janssen, E.C. Andrade, and M. Vojta. Magnetization processes of zigzag states on the honeycomb lattice: Identifying spin models for α-$RuCl_3$ and Na_2IrO_3. *Physical Review B*, 96(6):064430, 2017.

[67] I. Kimchi and Y.-Z. You. Kitaev-Heisenberg-J_2-J_3 model for the iridates A_2IrO3. *Physical Review B*, 84(18):180407, 2011.

[68] Y. Sizyuk, C. Price, P. Wölfle, and N.B. Perkins. Importance of anisotropic exchange interactions in honeycomb iridates: Minimal model for zigzag antiferromagnetic order in Na_2IrO_3. *Physical Review B*, 90(15):155126, 2014.

[69] I. Rousochatzakis, J. Reuther, R. Thomale, S. Rachel, and N.B. Perkins. Phase diagram and quantum order by disorder in the Kitaev K_1-K_2 honeycomb magnet. *Physical Review X*, 5(4):041035, 2015.

[70] E.C. Stoner. Collective electron ferromagnetism. *Proceedings of the Royal Society of London. Series A. Mathematical and Physical Sciences*, 165(922):372–414, 1938.

[71] E.C. Stoner. Collective electron ferromagnetism II. Energy and specific heat. *Proceedings of the Royal Society of London. Series A. Mathematical and Physical Sciences*, 169(938):339–371, 1939.

[72] J. Kübler. *Theory of itinerant electron magnetism*, volume 172. Oxford University Press, 2021.

[73] L. Néel. Theory of constant paramagnetism. application to manganese. *CR Acad. Sci. Paris*, 203:304–306, 1936.

[74] E. Fawcett. Spin-density-wave antiferromagnetism in chromium. *Reviews of Modern Physics*, 60(1):209, 1988.

[75] G. Czycholl and G. Czycholl. Elektronischer Transport in Festkörpern. *Theoretische Festkörperphysik Band 2: Anwendungen: Nichtgleichgewicht, Verhalten in äußeren Feldern, kollektive Phänomene*, pages 1–78, 2017.

[76] J. SPECOVIUS. Grundkurs leistungselektronik.

[77] J. Bellissard. Coherent and dissipative transport in aperiodic solids: An overview. *Dynamics of Dissipation*, pages 413–485, 2002.

[78] A. Miller and E. Abrahams. Impurity conduction at low concentrations. *Physical Review*, 120(3):745, 1960.

[79] J. Talamantes and J. Floratos. R-ε percolation in moderate-field hopping transport. *Philosophical Magazine B*, 65(4):627–630, 1992.

[80] M. Pollak and I. Riess. A percolation treatment of high-field hopping transport. *Journal of Physics C: Solid State Physics*, 9(12):2339, 1976.

[81] N. Apsley and H.-P. Hughes. Temperature-and field-dependence of hopping conduction in disordered systems. *Philosophical Magazine*, 30(5):963–972, 1974.

[82] N. Apsley and H.P. Hughes. Temperature-and field-dependence of hopping conduction in disordered systems, II. *Philosophical Magazine*, 31(6):1327–1339, 1975.

[83] N.F. Mott and E.A. Davis. *Electronic processes in non-crystalline materials*. Oxford university press, 2012.

[84] N.F. Mott. Conduction in glasses containing transition metal ions. *Journal of Non-Crystalline Solids*, 1(1):1–17, 1968.

[85] A.S. Skal, B.I. Shklovskii, and A.L. Efros. Activation Energy of Hopping Conduction. *Sov Phys Solid State*, 17(2):316–320, 1975.

[86] K.J. Hayden and P.N. Butcher. Analysis of hopping conduction in impurity bands in inversion layers. *Philosophical Magazine B*, 38(6):603–617, 1978.

[87] A.S. Skall and B.I. Shklovsky. Mott equation for low temperature edge conductivity. *Soviet Physics-Solid State*, 16(6):1190, 1974.

[88] C. Hurd. *The Hall effect in metals and alloys.* Springer Science & Business Media, 2012.

[89] J.M. Ziman. *Electrons and phonons: the theory of transport phenomena in solids.* Oxford university press, 2001.

[90] N. Nagaosa, J. Sinova, S. Onoda, A.H. MacDonald, and N.P. Ong. Anomalous hall effect. *Reviews of modern physics*, 82(2):1539–1592, 2010.

[91] J. Smit. The spontaneous hall effect in ferromagnetics i. *Physica*, 21(6-10):877–887, 1955.

[92] L. Berger. Side-jump mechanism for the hall effect of ferromagnets. *Physical Review B*, 2(11):4559, 1970.

[93] A. Tari. *The specific heat of matter at low temperatures.* World Scientific, 2003.

[94] Rigaku. MiniFlex600: Benchtop X-ray Diffractometer Instruction Manual. 2012.

[95] C. Janiak and E. Riedel. *Anorganische Chemie.* Walter De Gruyter, 2011.

[96] J.L. Amoros, M.J. Buerger, and M. C. de Amoros. The laue method academic press. *New York*, 1975.

[97] R. Diehl and N. Herres. X-ray fingerprinting routine for cut diamonds. *Gems & Gemology*, 40(1):40–57, 2004.

[98] N. Yao. *Focused ion beam systems: basics and applications.* Cambridge University Press, 2007.

[99] A. Weidner and H. Biermann. Moderne Methoden der Rasterelektronenmikroskopie. *Moderne Methoden der WerkstoffprüFung*, pages 217–254, 2014.

[100] K. Niederauer and W. Schäfer. Das Rasterelektronenmikroskop. *Physik in unserer Zeit*, 16(6):180–190, 1985.

[101] P.J.W. Moll. Focused ion beam microstructuring of quantum matter. *Annual Review of Condensed Matter Physics*, 9:147–162, 2018.

[102] J. Melngailis. Focused ion beam induced deposition: A review. *Electron-Beam, X-Ray, and Ion-Beam Submicrometer Lithographies for Manufacturing*, 1465:36–49, 1991.

[103] J. Puretz and L.W. Swanson. Focused ion beam deposition of Pt containing films. *Journal of Vacuum Science & Technology B: Microelectronics and Nanometer Structures Processing, Measurement, and Phenomena*, 10(6):2695–2698, 1992.

[104] C.-U. Ro, J. Osán, and R. Van Grieken. Determination of low-z elements in individual environmental particles using windowless epma. *Analytical Chemistry*, 71(8):1521–1528, 1999.

[105] R. Castaing. Electron probe microanalysis. In *Advances in electronics and electron physics*, volume 13, pages 317–386. Elsevier, 1960.

[106] Quantum Design. Magnetic property measurement system mpms 3 user's manual. *Quantum Design Inc*, 2016.

[107] A. Morello, W.G.J. Angenent, G. Frossati, and L.J. De Jongh. Automated and versatile SQUID magnetometer for the measurement of materials properties at millikelvin temperatures. *Review of scientific instruments*, 76(2):023902, 2005.

[108] Quantum Design. Electrical Transport Option (ETO) User's Manual (5th Edition). *Quantum Design Inc*, 2017.

[109] J. Weis. Quantum hall effect. In Tapash Chakraborty, editor, *Encyclopedia of Condensed Matter Physics (Second Edition)*, pages 553–566. Academic Press, Oxford, second edition edition, 2024.

[110] Quantum Design. Physical Property Measurement System - Heat Capacity Option User's Manual (27th Edition). *Quantum Design Inc*, 2017.

[111] Y. Singh and P. Gegenwart. Antiferromagnetic Mott insulating state in single crystals of the honeycomb lattice material Na_2IrO_3. *Physical Review B*, 82(6):064412, 2010.

[112] H. Watanabe, T. Shirakawa, and S. Yunoki. Microscopic study of a spin-orbit-induced mott insulator in ir oxides. *Physical review letters*, 105(21):216410, 2010.

[113] J.P. Clancy, N. Chen, C.Y. Kim, W.F. Chen, K.W. Plumb, B.C. Jeon, T.W. Noh, and Y.-J. Kim. Spin-orbit coupling in iridium-based 5d compounds probed by x-ray absorption spectroscopy. *Physical Review B*, 86(19):195131, 2012.

[114] S.K. Choi, R. Coldea, A.N. Kolmogorov, T. Lancaster, I.I. Mazin, S.J. Blundell, P.G. Radaelli, Y. Singh, P. Gegenwart, K.R. Choi, et al. Spin waves and revised crystal structure of honeycomb iridate Na_2IrO_3. *Physical review letters*, 108(12):127204, 2012.

[115] F. Ye, S. Chi, H. Cao, B.C. Chakoumakos, J.A. Fernandez-Baca, R. Custelcean, TF.. Qi, O.B. Korneta, and G. Cao. Direct evidence of a zigzag spin-chain structure in the honeycomb lattice: A neutron and x-ray diffraction investigation of single-crystal Na_2IrO_3. *Physical Review B*, 85(18):180403, 2012.

[116] Y. Singh, S. Manni, J. Reuther, T. Berlijn, R. Thomale, W. Ku, S. Trebst, and P. Gegenwart. Relevance of the Heisenberg-Kitaev model for the honeycomb lattice iridates A_2IrO_3. *Physical review letters*, 108(12):127203, 2012.

[117] S. Hwan Chun, J.-W. Kim, J. Kim, H. Zheng, C.C. Stoumpos, C.D. Malliakas, J.F. Mitchell, K. Mehlawat, Y. Singh, Y. Choi, et al. Direct evidence for dominant bond-directional interactions in a honeycomb lattice iridate Na_2IrO_3. *Nature Physics*, 11(6):462–466, 2015.

[118] A. Revelli, M.M. Sala, G. Monaco, C. Hickey, P. Becker, F. Freund, A. Jesche, P. Gegenwart, T. Eschmann, F.L. Buessen, et al. Fingerprints of kitaev physics in the magnetic excitations of honeycomb iridates. *Physical review research*, 2(4):043094, 2020.

[119] J.E. Moore. The birth of topological insulators. *Nature*, 464(7286):194–198, 2010.

[120] Y.K. Kim, N.H. Sung, J.D. Denlinger, and B.J. Kim. Observation of ad-wave gap in electron-doped Sr_2IrO_4. *Nature Physics*, 12(1):37–41, 2016.

[121] I. Battisti, K.M. Bastiaans, V. Fedoseev, A. De La Torre, N. Iliopoulos, A. Tamai, E.C. Hunter, R.S. Perry, J. Zaanen, F. Baumberger, et al. Universality of pseudogap and emergent order in lightly doped mott insulators. *Nature physics*, 13(1):21–25, 2017.

[122] M. Jenderka, J. Barzola-Quiquia, Z. Zhang, H. Frenzel, M. Grundmann, and M. Lorenz. Mott variable-range hopping and weak antilocalization effect in heteroepitaxial Na_2IrO_3 thin films. *Physical Review B*, 88(4):045111, 2013.

[123] J. Rodriguez, G. Lopez, F. Ramirez, N.P. Breznay, R. Kealhofer, V. Nagarajan, D. Latzke, S. Wilson, N. Marrufo, P. Santiago, et al. Competition between magnetic order and charge localization in Na_2IrO_3 thin crystal devices. *Physical Review B*, 101(23):235415, 2020.

[124] N. Alidoust, C. Liu, S.-Y. Xu, I. Belopolski, T. Qi, M. Zeng, D.-S. Sanchez, H. Zheng, G. Bian, and M. Neupane. Observation of metallic surface states in the strongly correlated Kitaev-Heisenberg candidate Na_2IrO_3. *Physical Review B*, 93(24):245132, 2016.

[125] L. Moreschini, I. Lo Vecchio, N.P. Breznay, S. Moser, S. Ulstrup, R. Koch, J. Wirjo, C. Jozwiak, K.S. Kim, E. Rotenberg, et al. Quasiparticles and charge transfer at the two surfaces of the honeycomb iridate Na_2IrO_3. *Physical Review B*, 96(16):161116, 2017.

[126] T. Dziuba. Combined Study of Local Spectroscopy and Macroscopic Electronic Transport of the Correlated Honeycomb Spin-Orbit Mott Insulator Na_2IrO_3. 2022.

[127] K. Mehlawat and Y. Singh. First-order density-wave-like transitions in surface-doped Na_2IrO_3. *Physical Review B*, 94(4):041109, 2016.

[128] I.-M. Pietsch. Magnetic anisotropy studies of kitaev model candidate materials. 2023.

[129] S. Manni. Synthesis and investigation of frustrated honeycomb lattice iridates and rhodates. 2014.

[130] J.W. Krizan, J.H. Roudebush, G.M. Fox, and R.J. Cava. The chemical instability of Na_2IrO_3 in air. *Materials Research Bulletin*, 52:162–166, 2014.

[131] J. Kaiser. Zur Güte von Einkristallen des Honigwabeniridats Na_2IrO_3. 2022.

[132] F.A. Breitner, J. Kaiser, A. Jesche, and P. Gegenwart. Metallic conductivity in Na-deficient structural domain walls in the spin-orbit Mott insulator Na_2IrO_3. *Physical Review B*, 108(23):235130, 2023.

[133] F. Freund, S.C. Williams, R.D. Johnson, R. Coldea, P. Gegenwart, and A. Jesche. Single crystal growth from separated educts and its application to lithium transition-metal oxides. *Scientific Reports*, 6(1):35362, 2016.

[134] F. Luepke, S. Manni, S.C. Erwin, I.I. Mazin, P. Gegenwart, and M. Wenderoth. Highly unconventional surface reconstruction of Na_2IrO_3 with persistent energy gap. *Physical Review B*, 91(4):041405, 2015.

[135] R. Comin, G. Levy, B. Ludbrook, Z.-H. Zhu, C.N. Veenstra, J.A. Rosen, Y. Singh, P. Gegenwart, D. Stricker, J.N. Hancock, et al. Na_2IrO_3 as a novel relativistic Mott insulator with a 340 meV gap. *Physical review letters*, 109(26):266406, 2012.

[136] B. I. Shklovskii and A.L. Efros. *Electronic properties of doped semiconductors*, volume 45. Springer Science & Business Media, 2013.

[137] M. Bremholm, S.E. Dutton, P.W. Stephens, and R.J. Cava. $NaIrO_3$—A pentavalent post-perovskite. *Journal of Solid State Chemistry*, 184(3):601–607, 2011.

[138] J. Zhao, L. Yang, Y. Yu, F. Li, R. Yu, and C. Jin. Structural and physical properties of the 6M $BaIrO_3$: a new metallic iridate synthesized under high pressure. *Inorganic chemistry*, 48(10):4290–4294, 2009.

[139] N.S. Kini, A.M. Strydom, H.S. Jeevan, C. Geibel, and S. Ramakrishnan. Transport and thermal properties of weakly ferromagnetic sr2iro4. *Journal of Physics: Condensed Matter*, 18(35):8205, 2006.

[140] N. Taira, M. Wakeshima, and Y. Hinatsu. Magnetic properties of iridium pyrochlores $R_2Ir_2O_7$ (R= Y, Sm, Eu and Lu). *Journal of Physics: Condensed Matter*, 13(23):5527, 2001.

[141] S.A. Carter, B. Batlogg, R.J. Cava, J.J. Krajewski, W.F. Peck Jr, and L.W. Rupp Jr. Mechanism for the metal-insulator transition in $Sr_2Ir_{1-x}Ru_xO_4$. *Physical Review B*, 51(23):17184, 1995.

[142] N. W. Ashcroft and N.D. Mermin. Solid state physics. *Physics (New York: Holt, Rinehart and Winston) Appendix C*, 1976.

[143] Y. Maeno, K. Yoshida, H. Hashimoto, S. Nishizaki, S.-I. Ikeda, M. Nohara, To. Fujita, A.P. Mackenzie, N.E. Hussey, J.G. Bednorz, et al. Two-dimensional Fermi liquid behavior of the superconductor Sr_2RuO_4. *Journal of the Physical Society of Japan*, 66(5):1405–1408, 1997.

[144] D.K. Roy and M. Kabir. Robust magnetism and phase transitions in ultrathin Na_2IrO_3 flakes. *Physical Review B*, 110(2):L020403, 2024.

[145] N.W. Ashcroft, N.D. Mermin, and S. Rodriguez. Solid state physics. *American Journal of Physics*, 46(1):116–117, 1978.

[146] H.-K. Jin, W. Kadow, M. Knap, and J. Knolle. Kinetic ferromagnetism and topological magnons of the hole-doped kitaev spin liquid. *arXiv preprint arXiv:2309.15153*, 2023.

[147] W. Kadow, H.-K. Jin, J. Knolle, and journal=npj Quantum Materials volume=9 number=1 pages=32 year=2024 publisher=Nature Publishing Group UK London Knap, M.l. Single-hole spectra of kitaev spin liquids: from dynamical nagaoka ferromagnetism to spin-hole fractionalization.

[148] J. Seidel, L.W. Martin, Q. He, Q. Zhan, Y.-H. Chu, A. Rother, M.E. Hawkridge, P. Maksymovych, P. Yu, M. Gajek, et al. Conduction at domain walls in oxide multiferroics. *Nature materials*, 8(3):229–234, 2009.

[149] P. Maksymovych, J. Seidel, Y.H. Chu, P. Wu, A.P. Baddorf, L.-Q. Chen, S.V. Kalinin, and R. Ramesh. Dynamic conductivity of ferroelectric domain walls in $BiFeO_3$. *Nano letters*, 11(5):1906–1912, 2011.

[150] S. Ghara, K. Geirhos, L. Kuerten, P. Lunkenheimer, V. Tsurkan, M. Fiebig, and I. Kézsmárki. Giant conductivity of mobile non-oxide domain walls. *Nature Communications*, 12(1):3975, 2021.

[151] K.W. Plumb, J.P. Clancy, L.J. Sandilands, V. V. Shankar, Y.F. Hu, K.S. Burch, H.-Y. Kee, and Y.-J. Kim. α- $RuCl_3$: A spin-orbit assisted Mott insulator on a honeycomb lattice. *Physical Review B*, 90(4):041112, 2014.

[152] L.J. Sandilands, Y. Tian, K.W. Plumb, Y.-J. Kim, and K.S. Burch. Scattering continuum and possible fractionalized excitations in α- $RuCl_3$. *Physical review letters*, 114(14):147201, 2015.

[153] A. Banerjee, C.A. Bridges, J.-Q. Yan, A.A. Aczel, L. Li, M.B. Stone, G.E. Granroth, M.D. Lumsden, Y. Yiu, J. Knolle, et al. Proximate Kitaev quantum spin liquid behaviour in a honeycomb magnet. *Nature materials*, 15(7):733–740, 2016.

[154] S. Agrestini, C.-Y. Kuo, K.-T. Ko, Z. Hu, D. Kasinathan, H. B. Vasili, J. Herrero-Martin, SM Valvidares, E. Pellegrin, and L.-Y. Jang. Electronically highly cubic conditions for Ru in α- $RuCl_3$. *Physical Review B*, 96(16):161107, 2017.

[155] L.J. Sandilands, Y. Tian, A.A. Reijnders, H.-S. Kim, K.W. Plumb, Y.-J. Kim, H.-Y. Kee, and K.S. Burch. Spin-orbit excitations and electronic structure of the putative Kitaev magnet α- $RuCl_3$. *Physical Review B*, 93(7):075144, 2016.

[156] J.A. Sears, M. Songvilay, K.W. Plumb, J.P. Clancy, Y. Qiu, Y. Zhao, D. Parshall, and Y.-J. Kim. Magnetic order in α-$RuCl_3$: A honeycomb-lattice quantum magnet with strong spin-orbit coupling. *Physical Review B*, 91(14):144420, 2015.

[157] J.A. Sears, Y. Zhao, Z. Xu, J.W. Lynn, and Y.-J. Kim. Phase diagram of α-$RuCl_3$ in an in-plane magnetic field. *Physical Review B*, 95(18):180411, 2017.

[158] H. B. Cao, A. Banerjee, J.-Q. Yan, C. A. Bridges, M. D. Lumsden, D. G. Mandrus, D. A. Tennant, B. C. Chakoumakos, and S. E. Nagler. Low-temperature crystal and magnetic structure of α-RuCl$_3$. *Phys. Rev. B*, 93:134423, Apr 2016.

[159] R.D. Johnson, S.C. Williams, A.A. Haghighirad, J. Singleton, V. Zapf, P. Manuel, I.I. Mazin, Y. Li, H.O. Jeschke, R. Valentí, et al. Monoclinic crystal structure of α- RuCl$_3$ and the zigzag antiferromagnetic ground state. *Physical Review B*, 92(23):235119, 2015.

[160] S. Gass, P. M. Consoli, V Kocsis, L. T. Corredor, P. Lampen-Kelley, D. G. Mandrus, S. E. Nagler, L. Janssen, M. Vojta, B. Buchner, and A. U. B. Wolter. Field-induced transitions in the Kitaev material α-RuCl$_3$ probed by thermal expansion and magnetostriction. *Phys. Rev. B*, 101:245158, 2020.

[161] Y. Kubota, H. Tanaka, T. Ono, Y. Narumi, and K. Kindo. Successive magnetic phase transitions in α-RuCl$_3$: xy-like frustrated magnet on the honeycomb lattice. *Physical Review B*, 91(9):094422, 2015.

[162] O. Tanaka, Y. Mizukami, R. Harasawa, K. Hashimoto, K. Hwang, N. Kurita, H. Tanaka, S. Fujimoto, Y. Matsuda, E.-G. Moon, et al. Thermodynamic evidence for a field-angle-dependent majorana gap in a kitaev spin liquid. *Nature Physics*, 18(4):429–435, 2022.

[163] M. Yamashita, J. Gouchi, Y. Uwatoko, N. Kurita, and H. Tanaka. Sample dependence of half-integer quantized thermal Hall effect in the Kitaev spin-liquid candidate α-RuCl$_3$. *Phys. Rev. B*, 102:220404(R), 2020.

[164] P. Czajka, T. Gao, M. Hirschberger, P. Lampen-Kelley, A. Banerjee, J. Yan, D.G. Mandrus, S.E. Nagler, and N.P. Ong. Oscillations of the thermal conductivity in the spin-liquid state of α-RuCl$_3$. *Nature Physics*, 17(8):915–919, 2021.

[165] T. Yokoi, S. Ma, Y. Kasahara, S. Kasahara, T. Shibauchi, N. Kurita, H. Tanaka, J. Nasu, Y. Motome, C. Hickey, S. Trebst, and Y. Matsuda. Half-integer quantized anomalous thermal Hall effect in the Kitaev material candidate α-RuCl$_3$. *Science*, 373:568, 2021.

[166] J. Bruin, R.R. Claus, Y. Matsumoto, N. Kurita, H. Tanaka, and H. Takagi. Robustness of the thermal Hall effect close to half-quantization in $\alpha-$RuCl$_3$. *Nat. Phys.*, 18:401, 2022.

[167] E. Lefrançois, G. Grissonnanche, J. Baglo, P. Lampen-Kelley, J.-Q. Yan, C. Balz, D. Mandrus, S.E. Nagler, S. Kim, Young-June Kim, N. Doiron-Leyraud, and Louis Taillefer. Evidence of a Phonon Hall Effect in the Kitaev Spin Liquid Candidate α-RuCl$_3$. *Phys. Rev. X*, 12:021025, 2022.

[168] J. Bruin, R.R. Claus, Y. Matsumoto, J. Nuss, S. Laha, B.V. Lotsch, N. Kurita, H. Tanaka, and H. Takagi. Origin of oscillatory structures in the magnetothermal conductivity of the putative Kitaev magnet $\alpha-$RuCl$_3$. *arXiv preprint arXiv:2205.15839*, 2022.

[169] H. Zhang, A.F. May, H. Miao, B.C. Sales, D.G. Mandrus, S.E. Nagler, M.A. McGuire, and J. Yan. Sample-dependent and sample-independent thermal transport properties of α- RuCl$_3$. *Physical Review Materials*, 7(11):114403, 2023.

[170] A.E. Newkirk and D.W. McKee. Thermal decomposition of rhodium, iridium and ruthenium clorides. *Journal of Catalysis*, 11:370, 1968.

[171] S. Reschke, F. Mayr, S. Widmann, H.-A. Krug Von Nidda, V. Tsurkan, M.V. Eremin, S.-H. Do, K.-Y. Choi, Z. Wang, and A. Loidl. Sub-gap optical response in the Kitaev spin-liquid candidate α-RuCl$_3$. *Journal of Physics: Condensed Matter*, 30(47):475604, 2018.

[172] M. Khachane, P. Nowakowski, S. Villain, J.R. Gavarri, I. Muller, C.and Luk'Yanchuk, M. Elaatmani, A. Outzourhit, and A. Zegzouti. Catalytic Studies of RuO$_2$ Films Deposited on Ferroelectrics Films by Spin Coating Process. *Ferroelectrics*, 371(1):34–42, 2008.

[173] F.A. Breitner, A. Jesche, V. Tsurkan, and P. Gegenwart. Thermal decomposition of the Kitaev material α- RuCl$_3$ and its influence on low-temperature behavior. *Physical Review B*, 108(4):045103, 2023.

[174] B.C. Passenheim and D.C. McCollum. Heat capacity of RuO$_2$ and IrO$_2$ between 0.54 and 10 K. *The Journal of Chemical Physics*, 51(1):320–321, 1969.

[175] F.A. Breitner, A. Jesche, V. Tsurkan, and P. Gegenwart. Supplement: Thermal decomposition of the Kitaev material α- RuCl$_3$ and its influence on low-temperature behavior. *Physical Review B*, 108(4):045103, 2023.

[176] D. Hirobe, M. Sato, Y. Shiomi, H. Tanaka, and E. Saitoh. Magnetic thermal conductivity far above the Néel temperature in the Kitaev-magnet candidate α- RuCl$_3$. *Physical Review B*, 95(24):241112, 2017.

[177] S.R. Butler and J.L. Gillson. Crystal growth, electrical resistivity and lattice parameters of RuO$_2$ and IrO$_2$. *Materials Research Bulletin*, 6(2):81–89, 1971.

[178] D.A.S. Kaib, K. Riedl, A. Razpopov, Y. Li, S. Backes, I.I. Mazin, and R. Valentí. Electronic and magnetic properties of the RuX_3 (X= Cl, Br, I) family: two siblings—and a cousin? *npj Quantum Materials*, 7(1):75, 2022.

[179] S. Mashhadi, D. Weber, L.M. Schoop, A. Schulz, B.V. Lotsch, M. Burghard, and K. Kern. Electrical transport signature of the magnetic fluctuation-structure relation in α-RuCl3 nanoflakes. *Nano letters*, 18(5):3203–3208, 2018.

[180] P. Barfield, V. Tran, V. Nagarajan, M. Martinez, A. Diego, D. Bergner, A. Lanzara, J.G. Analytis, and C. Ojeda-Aristizabal. Electronic transport mechanisms in a thin crystal of the Kitaev candidate α-RuCl_3 probed through guarded high impedance measurements. *Applied Physics Letters*, 122(24), 2023.

[181] A. Biffin, RD.. Johnson, S. Choi, F. Freund, S. Manni, A. Bombardi, P. Manuel, P. Gegenwart, and R. Coldea. Unconventional magnetic order on the hyperhoneycomb Kitaev lattice in β-$\mathrm{Li}_2\mathrm{IrO}_3$: full solution via magnetic resonant x-ray diffraction. *Physical Review B*, 90(20):205116, 2014.

[182] T. Takayama, A. Kato, R. Dinnebier, J. Nuss, H. Kono, L.S.I. Veiga, G. Fabbris, D. Haskel, and H. Takagi. Hyperhoneycomb iridate β-$\mathrm{Li}_2\mathrm{IrO}_3$ as a platform for Kitaev magnetism. *Physical review letters*, 114(7):077202, 2015.

[183] A. Ruiz, A. Frano, N.P. Breznay, I. Kimchi, T. Helm, I. Oswald, J.Y. Chan, R.J. Birgeneau, Z. Islam, and J.G. Analytis. Correlated states in β-$\mathrm{Li}_2\mathrm{IrO}_3$ driven by applied magnetic fields. *Nature Communications*, 8(1):961, 2017.

[184] A.A. Tsirlin and P. Gegenwart. Kitaev magnetism through the prism of lithium iridate. *physica status solidi (b)*, 259(5):2100146, 2022.

[185] L. Rademaker. Quenching the kitaev honeycomb model. *SciPost Physics*, 7(5):071, 2019.

[186] H. Bragança, M.F. Cavalcante, R.G. Pereira, and M.C.O. Aguiar. Quench dynamics and relaxation of a spin coupled to interacting leads. *Physical Review B*, 103(12):125152, 2021.

[187] P.R. Willmott, D. Meister, S.J. Leake, M. Lange, A. Bergamaschi, M. Böge, M. Calvi, C. Cancellieri, N. Casati, A. Cervellino, et al. The materials science beamline upgrade at the swiss light source. *Journal of synchrotron radiation*, 20(5):667–682, 2013.

[188] N. Hua, A. Breitner, F.A.and Jesche, S.-W. Huang, C. Rüegg, and P. Gegenwart. Structural and magnetic properties of β-Li_2IrO_3 after grazing-angle focused ion beam thinning. *arXiv preprint arXiv:2310.18644*, 2023.

[189] S. Ohta, T. Kanomata, and T. Kaneko. Magnetic properties of CrRhAs and CrRuAs. *Journal of magnetism and magnetic materials*, 90:171–172, 1990.

[190] T. Kanomata, T. Kawashima, H. Utsugi, T. Goto, H. Hasegawa, and T. Kaneko. Magnetic properties of the intermetallic compounds MM'X (M= Cr, Mn, M'= Ru, Rh, Pd, and X= P, As). *Journal of applied physics*, 69(8):4639–4641, 1991.

[191] T. Kaneko, T. Kanomata, T. Kawashima, S. Mori, S. Miura, and Y. Nakagawa. High-field magnetization in intermetallic compounds MM'X (M= Mn, Cr; M'= Ru, Rh, Pd; X= As, P). *Physica B: Condensed Matter*, 177(1-4):123–126, 1992.

[192] S. Ohta, T. Kaneko, H. Yoshida, T. Kanomata, and H. Yamauchi. Pressure effect on the magnetic transition temperatures and thermal expansion in chromium ternary pnictides CrMAs (M= Ni, Rh). *Journal of magnetism and magnetic materials*, 150(2):157–164, 1995.

[193] Y.N. Huang, H.O. Jeschke, and I.I. Mazin. CrRhAs: a member of a large family of metallic kagome antiferromagnets. *npj Quantum Materials*, 8(1):32, 2023.

[194] P.C. Canfield, T. Kong, U.S. Kaluarachchi, and N.H. Jo. Use of frit-disc crucibles for routine and exploratory solution growth of single crystalline samples. *Philosophical magazine*, 96(1):84–92, 2016.

[195] R.V. Chamberlin. Mean-field cluster model for the critical behaviour of ferromagnets. *Nature*, 408(6810):337–339, 2000.

[196] K. Usami. Magnetoresistance in antiferromagnetic metals. *Journal of the Physical Society of Japan*, 45(2):466–475, 1978.

[197] H. Yamada and S. Takada. Magnetoresistance of antiferromagnetic metals due to s-d interaction. *Journal of the Physical Society of Japan*, 34(1):51–57, 1973.

[198] Y. Tokiwa, M. Garst, P. Gegenwart, S.L. Bud'ko, and P.C. Canfield. Quantum bicriticality in the heavy-fermion metamagnet ybagge. *Physical review letters*, 111(11):116401, 2013.

[199] K. Zhao, H. Deng, H. Chen, K.A. Ross, V. Petříček, G. Günther, M. Russina, V. Hutanu, and P. Gegenwart. Realization of the kagome spin ice state in a frustrated intermetallic compound. *Science*, 367(6483):1218–1223, 2020.

[200] K. Zhao, Y. Tokiwa, H. Chen, and P. Gegenwart. Discrete degeneracies distinguished by the anomalous hall effect in a metallic kagome ice compound. *Nature Physics*, 20(3):442–449, 2024.

[201] N. Iwata, T. Matsushima, H. Fujii, and T. Okamoto. Magnetic properties of (cr1- xnix) 2as single crystal compounds. *Journal of the Physical Society of Japan*, 49(4):1318–1322, 1980.

[202] M. Bacmann, D. Fruchart, A. Koumina, and P. Wolfers. Low temperature magnetic structure of crnias. In *Materials Science Forum*, volume 443, pages 379–382. Trans Tech Publ, 2004.

[203] Z.M. Stadnik, P. Wang, N. Jansen, D. Walcher, P. Gütlich, and T. Kanomata. Magnetization and ^{61}Ni Mössbauer effect study of the ternary arsenide CrNiAs. *Journal of Physics: Condensed Matter*, 20(32):325230, 2008.

[204] T.R. Kirkpatrick and D. Belitz. Ferromagnetic quantum critical point in noncentrosymmetric systems. *Physical Review Letters*, 124(14):147201, 2020.

[205] B. Shen, Y. Zhang, Y. Komijani, M. Nicklas, R. Borth, A. Wang, Y. Chen, Z. Nie, R. Li, X. Lu, et al. Strange-metal behaviour in a pure ferromagnetic kondo lattice. *Nature*, 579(7797):51–55, 2020.

[206] B. Shen, F. Breitner, J. Ebad-Allah, J. Langmann, C.A. Kuntscher, P. Gegenwart, and A.A. Tsirlin. Magnetoelastic coupling in a distorted Kagome ferromagnet CrNiAs. *unpublished*, 2025.

[207] B. Shen, F. Du, F. Breitner, A.A. Tsirlin, and P. Gegenwart. Pressure-induced strange metal phase in a metallic kagome ferromagnet. *unpublished*, 2025.

[208] J. Smit. The spontaneous hall effect in ferromagnetics ii. *Physica*, 24(1-5):39–51, 1958.

[209] N. Iwata, T. Matsushima, H. Fujii, and T. Okamoto. Magnetic properties of $(\mathrm{Cr}_{1-x}\mathrm{Ni}_x)_2\mathrm{P}$ compounds. *Journal of the Physical Society of Japan*, 50(3):729–730, 1981.

[210] T. Kanomata, H. Endo, H. Yamauchi, Y. Yamaguchi, H. Yoshida, T. Kaneko, H.A. Katori, and T. Goto. Magnetovolume effect of CrNiP. *Physica B: Condensed Matter*, 237:517–519, 1997.

[211] Z.M. Stadnik, P. Wang, N. Jansen, D. Walcher, P. Gütlich, and T. Kanomata. Magnetic properties and ^{61}Ni Mössbauer spectroscopy of the ternary phosphide CrNiP. *Journal of Physics: Condensed Matter*, 20(28):285227, 2008.

[212] S.V. Orishchin and Y.B. Kuz'ma. Cr(W)-Ni-P ternary systems. *Izv. Akad. Nauk SSSR, Neorg. Mater*, 20(3):425–430, 1984.

[213] P. Telang, K. Mishra, G. Prando, A.K. Sood, and S. Singh. Anomalous lattice contraction and emergent electronic phases in Bi-doped $Eu_2Ir_2O_7$. *Physical Review B*, 99(20):201112, 2019.

[214] X. Chen, T. Hogan, D. Walkup, W. Zhou, M. Pokharel, W. Yao, M.and Tian, T. Z. Ward, Y. Zhao, D. Parshall, et al. Influence of electron doping on the ground state of $(Sr_{1-x}La_x)_2IrO_4$. *Physical Review B*, 92(7):075125, 2015.

[215] T. Hogan, X. Wang, H. Chu, D. Hsieh, and S.D. Wilson. Doping-driven structural distortion in the bilayer iridate $(Sr_{1-x}La_x)_3Ir_2O_7$. *Physical Review B*, 95(17):174109, 2017.

[216] A. Janotti, B. Jalan, S. Stemmer, and C.G. Van de Walle. Effects of doping on the lattice parameter of $SrTiO_3$. *Applied Physics Letters*, 100(26), 2012.

[217] T.F. Qi, O.B. Korneta, X. Wan, L.E. DeLong, P. Schlottmann, and G. Cao. Strong magnetic instability in correlated metallic $Bi_2Ir_2O_7$. *Journal of Physics: Condensed Matter*, 24(34):345601, 2012.

Acknowledgements

I would like to thank the following people who contributed to the successful completion of this thesis:

- Prof. Dr. Philipp Gegenwart for giving me the opportunity to write this thesis at his chair as well as agreeing to be my supervisor, answering questions and providing input as well as being first referee.

- Prof. Dr. Manfred Albrecht for agreeing to be the second referee of this thesis.

- Dr. Anton Jesche for offering advice with crystal growth, measurements and always taking the time to answer my questions and explain things more than once if necessary as well as for agreeing to proofread my thesis.

- Dr. Bin Shen for performing some of the measurements shown in my thesis.

- Klaus Wiedenmann for general support with measurement devices and lab equipment as well as introducing me to the FIB and often providing help with fatal error messages and other FIB problems which often magically disappeared upon me trying to demonstrate them to him.

- Alexander Herrenberger for support with all kinds of technical things and measurement set-ups.

- Dr. Sebastian Bachus for providing help with using the He3-option.

- Christine Schäfer for providing help with all things concerning administrative matters.

- The many different people whom I shared an office with over the course of my (many) years at the chair and all other members of EP6 for taking part in providing a pleasant work atmosphere, especially those involved in regular coffee breaks and games of Hanabi which everyone really enjoyed without ever complaining about anything. I really enjoyed being a part of this group for the last few years.

- My parents and grandparents for all the love and support I have received during the many years of my studies.
- Special thanks to Tessi and Alex for proofreading my thesis and always listening to me complaining about the latest problems during my PhD (or at least trying her best to keep listening, once I start talking about physics).